Asymmetric/Anisotropic Structure of Active Mo and Pt Sites on Metal-Oxide Single Crystal Surfaces by Means of Polarization-Dependent Total-Reflection Fluorescence X-ray EXAFS

偏光全反射蛍光XAFS法による酸化物単結晶表面上のMo及びPt触媒活性点の非対称・異方性構造解析

Wang-Jae Chun

田　　旺帝

Asymmetric/Anisotropic Structure of Active Mo and Pt Sites on Metal-Oxide Single Crystal Surfaces by Means of Polarization-Dependent Total-Reflection Fluorescence XAFS

A Thesis
Submitted to
The University of Tokyo
in Fulfillment of the Requirements
for the Degree
of
Doctor of Science

By Wang-Jae Chun

Jun, 1997

" In oneself lies the whole world, and if you know how to look and learn, then the door is there and the key is in your hand. Nobody on earth can give you either that key or the door to open, except yourself"

J. KrishnaMurti - from You are the World.

Acknowledgment

All the studies in my doctor thesis have been carried out under Prof. Y. Iwasawa's supervision. He taught me a lot of fundamental and technical knowledges as well as suggested a way of a researcher. I also appreciate Assistant Prof. K. Asakura for his continuing guidance and encouragement for my work. For the long machine time and hard measurement in KEK-PF, he never stopped to encourage me. I could not have been done my work without him.

I had a valuable and helpful advice from Dr. T. Aruga, Dr. H. Onishi, Dr. T. Sasaki and Dr. K. Fukui. I would like to express gratitude to them. I would like to thank Dr. T. Inoue, Dr. K. Okumura and Dr. T. Sueyoshi. I have been enjoyed in discussing and spending in laboratory especially with Dr. Inoue. I also thank all other members of Iwasawa Lab. including alumni, Dr. M. Shirai, Dr. N. Ichikuni and Dr. K. Tomishige, and visiting scientists during my doctoral course. I am especially grateful to Dr. Shirai and Dr. Tomishige for their kind encouragement and advice on my works. I also thank Dr. T. Yokoyama for valuable discussions.

Also I would like to appreciate the staffs of the Photon Factory, Prof. M. Nomura, Dr. S. Kishimoto and Dr. N. Usami for arranging beam time and technical advice.

To Prof. U. Lee, my mentor, I would like to express my deepest gratitude to him for his guidance and encouragement. Finally, I would like to give my deepest love to my family.

CONTENTS

Chapter 1

Introduction

1.1 General Remarks

Catalytic science has a long history originating from Humphry Davy(1778 ~ 1829)'s electrolysis experiments with Pt and is still an attractive field because of fundamental and technological points of view. Since the days, there are two primary questions about catalysts. "What is the structure of catalyst?" and "What influences does the catalytic structure have on the reactivity?" Nowdays catalytic reaction mainly occurs at a special site called as " active site" which is composed of ensemble of atoms. Thus in order to answer these questions, one has to reveal the structure of active sites.

With recent progress in characterization techniques, we have been able to clarify the physical and chemical properties of materials in atomic or molecular levels based on the structural information such as atomic position, thermal vibration, bond length, bond angle, electronic state and so on. In catalysis field such information must be necessary for understanding catalysis in an atomic scale. Because of inhomogeneity in the surface structure and lack of the surface sensitive techniques, it was difficult to carry out the characterization of active sites in an atomic level. In 1970s a great development in ultra high vacuum technique shed light on surface science. One can prepare a clean and well-defined single crystal surface in an ultrahigh vacuum chamber, which offers reproducibility of the experimental results. Electron spectroscopy such as XPS and Auger as well as electron diffraction technique provide the information on surface electronic state and long-range order structure. Many researchers have investigated the catalyses of such well-defined single crystal surfaces and found basic ideas for activity of kinks and steps[1], surface induced reconstruction [2] and reaction, coadsorption[3] and so on. However, practical catalysts are often used in the form of supported metal catalysts using powder oxides as supports, which makes it acutely difficult to apply these surface science techniques. Thus the science about real catalyst seems to be still in the "Dark Ages" and someone gives up the understanding of catalysis on the atomic level. However, the steady efforts in this field have established structural analysis tools suitable

for the charcterization of powder samples. TEM(Transmission Electron Microscopy) and EXAFS(Extended X-ray Absorption Fine Structure) are powerful techniques for powder samples. EXAFS is referred to a fine structure appearing over the energy range 30 –1000 eV above the edge and can provide interatomic distances and coordination numbers for bondings. Although many attempts to prepare homogeneous and well-defined active sites have been done for powder catalysts, yet such preparation techniques have some limitations in full characterization of active sites in an atomic level. One requires a new model system for dispersed systems as well as development of analysis techniques suitable for the model supported system. One candidate a single crystal with metal clusters dispersed on it. Up to now, there are a number of analytical methods for dispersed model systems such as RAIRS, AFM, XPS, ARXPS and so on. Although EXAFS can be one of the most powerful techniques to analyze model systems, conventional EXAFS can not be applied to them as discussed later, and PTRF-EXAFS(Polarization-dependent Total Reflection Fluorescence EXAFS) has been developed to characterize model dispersed systems. I have further improved the PTRF-EXAFS method which is described in this thesis. In this chapter I will describe active site structures in conventional catalysts, characterization techniques for conventional catalysts, especially EXAFS, the feature of model dispersed catalysts, and advantages of PTRF-EXAFS and its limitation in application. In the last part of this chapter I will give the aim and the outline of this thesis.

1.2 Active Sites- Asymmetric/ Anisotropic Structure Influencing Catalytic Reactions

Supported metal catalysts have been used in commercially important applications such as hydrogenation, isomerization, reforming, hydrocracking, and oxidation process. They are formed as highly dispersed metal particles on inorganic metal oxides with high surface areas since obtaining smaller metal particles which present higher activities and implying economical reasons[4-6]. Reactions often take place at active sites at surface of

the noble metal particles, where adsorbed gas molecules react with the surface metal atoms to be converted to desired products. Therefore, they differ to bulk structures since the active site structure presents unsaturated bonding features having no bonding atoms in an external direction from the surface while bulk ones bonding with neighboring atoms in all directions. As a result, it has been considered that the bonding feature of active sites may generate asymmetric structure at the surface, at least between the surface normal and the plane direction. It is also predicted that surface structure dynamically changes and asymmetric structure is induced by the atmosphere under reaction conditions.

Moreover, there is another feature of the structure of active sites on supports. Anisotropy is induced by the interaction between active sites and metal oxide supports. The supports, generally inorganic metal oxides with high surface areas, have been considered to be inert for catalytic reactions. However, it has now become clear that most of supported catalysts produce completely different catalytic reaction properties compared to those of the unsupported ones. Furthermore, activity and selectivity depend on not only the amount of active sites but also the kind of supports. Inorganic metal oxide supports play a role not only to disperse the metal particles but also change their morphologies, orientations, structures, and electrical states by the interaction between metal particles and supports. The orientation of active metal structures at the surface, which is a key issue of solid a catalysis, is therefore directly related to the structure of support surfaces[7, 8]. If oxide support surface is anisotropic, it should be expected that active sites on the support form a particular oriented structure, that is, anisotropic active sites. Thus, it is indispensable to determine asymmetric / anisotropic surface active structures in order to elucidate the mechanism of heterogeneous catalysis.

1.3 Application of EXAFS to Catalyst Characterization

Extended X-ray absorption fine structure(EXAFS) spectroscopy is a technique to provide information about the local structure around an atom, i. e., the number and kind of neighbor atoms and interatomic distances[9-11]. The EXAFS technique is especially useful for the structural study of catalysts because catalytically active materials on oxide are present as tiny crystallites or particles, for whose characterization other techniques like x-ray diffraction or electron diffraction, cannot be used. When the dispersion of active materials is high and the size of the crystallites is below ca. 3 nm, the X-ray diffraction lines become too broad and weak to be observable. Moreover, the EXAFS technique gives also structural information nondestructively and is independent of the kinds of sample and the atmosphere of measurements. Therefore, the EXAFS technique is extremely useful in studying the structure of highly dispersed heterogeneous catalysts, under in-situ conditions[12-17]. Since the EXAFS oscillations are averaged over every direction if powder catalysts are employed as samples, and thus angle-dependent properties of EXAFS become nominal one, however, it is not straightforward to obtain a precise structural information from a conventional EXAFS. Therefore, it is not possible to achieve asymmetric or anisotropic structural analysis.

1.4 Application of Polarization-dependent Total-Reflection Fluorescence EXAFS (PTRF-EXAFS) to Characterization of Catalysts with Asymmetric or Anisotropic Structures

In recent years, catalytic chemistry on well-defined surfaces of metal or metal oxide is attracting attention[1, 18, 19]. Work within several research groups has integrated the surface science techniques into fundamental catalytic research. This method relies to a large degree on carrying out catalytic reactions on metal single crystal surfaces at realistic conditions approaching to those typically found in technical

applications. The kinetics and surface chemistry of several catalytic reactions have demonstrated the relevance of single-crystal studies for modeling the behavior of high surface area supported catalysts[18-26].

The EXAFS amplitude depends on the angle between the electric field vector(E) of the incident x-rays and the bond vector(r) of absorbing atom and scattering atoms as shown in Fig.1. Bond distances and coordination numbers around x-ray absorbing atoms can be expressed by $\chi(kj)$(EXAFS oscillation) of eq. (1)[11, 27],

$$\chi(k_j) = \sum_j \frac{N_j^* F_j(k_j)}{k r_j^2} \exp(-2\sigma_j^2 k_j^2) \exp(-2r_j/\lambda_j) \sin(2k_j r_j + \phi_j(k_j)) \qquad (1),$$

where kj, r_j, σ_j, λ_j, $F_j(k)$ and $\phi_j(k)$ are wave-number of photoelectron, interatomic distance, Debye-Waller factor, mean free path of photoelectron, backscattering amplitude function and phase shift function for j-th shell, respectively. For oriented samples, effective coordination number from EXAFS spectra is expressed by eq. (2) and eq. (3),

$$N^* = 3\sum_j \cos^2\theta_j \quad \text{(for K and } L_1\text{-edges)} \qquad (2),$$

$$N^* = (0.5+c)N + (1.5-3c)\sum_j \cos^2\theta_j \quad \text{(for } L_2 \text{ and } L_3\text{-edges)} \qquad (3),$$

where θ_j is the angle between the electric field vector(E) of the incident x-rays and the bond vector(r). The term c in eq. (3) has been calculated for various elements and was found c.a. 0.2 for Z ≥20 and relatively independent of k[28, 29]. Since the angular symmetry is weaken for L_2 and L_3-edges by the isotropic term 0.5 N in eq. (3), the characterization of a geometry from L_2 and L_3-edge EXAFS is complicated but is still possible to acheive it[30-32].

When a metal oxide single crystal is used as a support and well-polarized and highly brilliant x-ray of synchrotron radiation is used as x-ray source, it is possible to characterize the asymmetric structure of active sites separately in two different directions parallel and perpendicular to the surface(Fig. 1(b), (c)). However, there are several problems in detecting EXAFS signals from this kind of system. Since concentrations of monolayer metal on a flat surface are in the range 10^{14}-10^{15} atoms cm^{-2}, which is 4-5 orders of magnitude lower than those of metals for conventional catalysts in a powder

form, it is not available to detect EXAFS signal in a transmission mode[33]. It is apparent that probability emitting electrons from a level, that is, the absorption coefficient, is equal to the probability of creating a core hole. Any process which is proportional to the absorption coefficient can be used to obtain EXAFS spectra. The core hole in shell A can be annihilated by a radiated transition(fluorescence X-ray emission) or a non radiated electron transition(auger electron) from a lower binding energy level B as shown in Fig.2. Instead of measurement in a transmission mode, surface EXAFS spectra can be obtained by detecting Auger electrons or fluorescence X-rays. The electron yield EXAFS is surface sensitive since the escape depth is less than 1 nm to several nm[34-36]. However, the technique has also some disadvantages. One is a low ratio of the electron signal to background. The other one is that it is impossible to measure EXAFS signal under gas atmosphere since the electron yield technique needs UHV conditions.

On the other hand, the fluorescent x-ray detection technique can be used over whole energy range and often produces a higher sensitivity by two or more orders of magnitude than transmittance EXAFS[37-39]. Thus, it is possible to submonolayer metal species on surfaces. Usually it is more preferable for dilute samples than monitoring direct absorption. In a soft X-ray region, the fluorescence-detection mode successfully gives the EXAFS signals with high quality, and the polarization-dependent EXAFS studies determine the adsorption sites of light elements such as C, O, S, Cl, and P with various substrates[40, 41]. Moreover, the most outstanding advantage of the fluorescence detection technique is that it can get EXAFS signals under various reaction conditions in the presence of ambient gas. The technique is also suitable for higher-Z elements since fluorescence yield for higher-Z atoms is large compared to lower-Z elements(ε=0.3 for Z=26(Fe); ε=0.75 for Z=42(Mo))[38]. The problem in measuring the fluorescence from sample surfaces at the high energy region is attributed to a high background. When high energy X-ray radiation hits the surface, not only fluorescence X-ray radiation but also scattering X-ray are produced. The fluorescence X-rays are drowned in the scattering X-rays. To reduce the noise from scattering X-ray radiation, a

total-reflection method is advantageous. When the incidence angle of the X-rays is below the critical angle, total reflection occurs. The critical angle is given by eq. (4),

$$\theta_c = \sqrt{N(Z/A)\rho e^2 \lambda^2 / \pi m_e c_0^2} \qquad (4),$$

where N is Avogadro`s number, Z is the atomic number of the x-ray absorbing atoms, A is the atomic mass of the X-ray absorbed atoms, ρ is the density of the substrate, e is the elementary charge, λ is the wave length of the incident x-ray, m is the electron rest mass and c_0^2 is the speed of light in vacuum. The critical angle is evaluated to be as small as about several mrad, because the refractive index of X-rays is below unity. In other words, the penetration depth of incident X-rays becomes below several nm, the scattering X-ray radiation(which causes the high background) becomes low under total-reflection conditions and surface sensitive fluorescence XAFS signals are obtained[42]. Thus it is possible to get surface sensitive EXAFS spectra by the total-reflection fluorescence technique. The first measurement of submonolayer species at the high energy region by a total-reflection fluorescence yield technique was done by Heald et al.[38]. They reported the EXAFS signals of Au layers on a glass and Ag substrate with the incident X-ray parallel to the substrate[38]. The technique has been applied to semiconducting materials, electrodes and adsorbates surfaces. Shirai et al. developed the polarization-dependent total-reflection fluorescence XAFS(PTRF-XAFS) chamber and then applied the technique to catalytically interesting systems[43-52].

1.5. Purpose in This Thesis

In this thesis, I challenged to probe active site structures and to obtain relationship with the catalytic properties. The goal of this work is a better understanding of active sites in the field of microscopic structure by characterization of metal or metal oxide species on a single crystal metal oxide surface by means of Polarization-dependent Total-Reflection Fluorescence X-ray Absorption Fine Structure(PTRF-XAFS) spectroscopy.

1.5.1 Mo oxides on TiO_2(110)

Most catalytically interesting elements such as Mo, Ru, Rh, etc. have higher Z-numbers in a periodic table. Although those elements show high catalytic performances, PTRF-XAFS measurements have not been applied to those systems. In this work, I challenged to perform high K-edge PTRF-XAFS measurements for those higher Z-elements and tried to investigate their surface structure.

I adopted Mo as a target element since it is a principal component in industrial catalysts for the selective oxidation and ammoxidation of propene as well as many other catalysts of industrial importance[53-55]. Especially, TiO_2-supported molybdenum oxides works as good catalysts for the selective oxidation of hydrocarbons[56] and for the oxidative dehydrogenation of alcohols[57], as well as for the selective catalytic reduction of NOx by ammonia[58, 59]. Moreover, they are also active for alkene metathesis[60] and for hydrodesulfurization catalysts[61, 62]. Although there are many controversies in structural results, the importance of molybdenum oxide catalysts in catalytic applications has promoted a large number of studies concerning the surface structures and the effect of the oxide support on the surface properties using various spectroscopic techniques such as ultraviolet-visible spectroscopy(UV-VIS)[63], infrared spectroscopy(IR)[64-66], electron spin resonance spectroscopy(ESR)[67], ion scattering spectroscopy(ISS) [68], X-ray photoelectron spectroscopy(XPS)[67, 69, 70], and laser Raman spectroscopy[66, 69, 71-73]. Delmon. et al. have suggested that molybdena-titania interaction leads to an epitaxial growth of MoO_3 on the TiO_2[68]. Volta et. al reported the anisotropic crystal growth of MoO_3 [74]. Also, the coordination symmetry around Mo atoms is influenced by the support, and a recent X-ray absorption fine structure(XAFS) study[75] concludes that while the predominant structure of molybdates on Al_2O_3 changes from tetrahedral to octahedral with increasing Mo loading, MoO_3-like structure is formed on SiO_2 support, and dispersed Mo atoms in octahedral coordination are favored over TiO_2. A high dispersion of octahedral polymolybdates over TiO_2

surface was reported by Ng and Gulari[71], who used laser Raman and IR spectroscopies for characterization, and it was also suggested by ESR and XPS[67].

I used a rutile-type $TiO_2(110)$ single crystal as a support and attempted to measure PTRF-XAFS for investigating the structure of Mo oxides on $TiO_2(110)$ single crystal as a model catalyst. Titanium dioxide is a known photoelectrode. A large crystal is available only for rutile at present though titanium oxide has two other crystal structures, anatase and brooklite, both of which are slightly distorted form the rutile structure. Rutile titanium dioxide surfaces have for some years been used as a typical metal oxide for exploring surface oxide physics and chemistry. Several pioneering works revealed the structure and electron state of a rutile $TiO_2(110)$ surface by various characterization techniques. (1x1) or (2x1) LEED patterns for $TiO_2(110)$ have been reported by many groups[21, 76]. Preliminary medium-energy electron diffraction(MEED) measurements have been performed on polished and annealed $TiO_2(110)$ surfaces[77]. Scanning tunneling microscopy(STM) has also been reported on $TiO_2(110)$ surfaces[78-80]. Surface x-ray diffraction(SXRD) has proved the surface structure of $TiO_2(110)$ combining with LEED[81]. Ab-initio calculations of the energy minimized structure also suggested the (110) surface structure of TiO_2[82, 83]. Rutile $TiO_2(110)$ surfaces alternatively aligned of the protruding oxygen ridge along [001] axis and the groove which is the rows of five -fold coordinated Ti^{4+} cations between the protruding oxygen ridges, which has a characteristic anisotropy. $TiO_2(110)$ plane is a most stable surface since the largest stability results from the large coordination on the (110) surface. Half of Ti cations have six-fold coordination while the others are five-fold coordinated. Na and Ni were adsorbed on the exposed Ti-rows of the substrate[84, 85]. Onishi et al. also reported the structure sensitive reaction of CO_2 with $TiO_2(110)$ surfaces modified with Na adatoms by scanning tunneling microscopy[86]. At low coverages (0.4 atom/nm^2 or less) Na adatoms are ionized and adsorbed on the exposed Ti rows of the substrate. CO_2 adsorption on the protruding oxygen was assisted by Na coadsorption. Schierbaum et. al studied the interaction of Pt with $TiO_2(110)$ surface by

means of XPS, UPS, ISS, AES, and ESD, and found that Pt atoms adsorb preferentially on top of five fold coordinated Ti atoms which act as nucleation sites for the subsequent three dimensional growth of Pt clusters [87] Considering those chemical, physical and anisotropic properties, it could be expected that the characteristic Mo oxide structure will be formed on TiO_2(110).

In Chapter 3, I tried to improve the PTRF-XAFS measurements for higher Z-elements ($Z \geq 42$) and also evaluated the efficiency of a CdTe solid state detector for fluorescence detection. The heavy metal elements have K-edge x-ray absorption energies higher than over 20 keV. The high-energy K-edge EXAFS measurement in a total reflection condition has been believed to be quite difficult since their extremely small critical angle required for the total-reflection. In order to solve this problem, I used a high-precision 4-axis goniometer stage which makes adjustment at a minimum step of 0.17 mrad possible. On the other hand, another problem in a fluorescent x-rays detection is attributed to Bragg diffraction stemmning from TiO_2(110) substrate ,which disturbs to conduct the PTRF-XAFS measurements. A small CdTe solid-state detector can be efficiently adjusted to a position where there is no Bragg diffraction. With those improvements, I firstly succeeded in measuring Mo K-edge PTRF-XAFS of molybdenum oxides on TiO_2(110) as described in Chapters 3 and 4. In Chapter 3, a CdTe solid state detector was applied to the measurements of polarization-dependent total-reflection fluorescence XAFS spectra. The data reveal that the detector with a compact size has a good sensitivity and is appropriate for in-situ measurements and removal of X-ray Bragg diffraction. The detector efficiently recorded the high-energy K-edge XAFS spectra for molybdenum oxides supported on TiO_2(110).

In Chapter 4, I report the first Mo K-edge Fluorescence EXAFS under a total reflection ocondition by means of the PTRF-EXAFS technique. Although there are some works for P, S, and Cl on Ni(7 9 11) considering a polarization-dependency for each axis along the surface[88-90], there is no report for the higher-Z elements($Z \geq 42$) on metal oxide single crystals. This work is the first report of the successful application

of PTRF-EXAFS to the element with high K-edge energy(over 20 keV). PTRF-XAFS spectra where the electric-field vectors of the incident x-rays are parallel to [1 $\bar{1}$ 0], [001] and [110] directions of TiO_2(110) revealed different oscillations from each other, and indicated the formation of an anisotropic surface structure. Comparing the observed data to the calculated data in the three directions, we concluded that Mo dimer species were formed, with Mo-Mo bond parallel to the [1 $\bar{1}$ 0] direction of TiO_2 (110) surface. In follwing Chapter 5, the PTRF-EXAFS is applied to investigate the surface structure of Mo oxide species on TiO_2(110) induced by alkali metals. It is revealed that the Mo oxides species on TiO_2(110) has symmetric tetrahedral Mo oxide structure with Mo-O 0.176 nm. It is supposed that the symmetric structure is formed by an interaction between molybdenum and alkali metals..

1.5.2 Supported Pt cluster catalysts

Knowledge of the structure and chemical state of active sites at catalyst surface is indispensable to elucidate catalytic reaction mechanisms and to develope new-catalytic materials. I found that the catalysts prepared by supporting [$Pt_4(\mu$-$CH_3COO)_8$] on SiO_2 and α-Al_2O_3 showed remarkably high activities for formic acid decomposition compared with traditional Pt particle catalysts. Decomposition of formic acid on metal and oxide surfaces has served as a convenient test reaction for fundamental research on catalysis; e.g. to determine the factors which can affect the catalytic properties of metals and metal oxides[91-94]. [$Pt_4(\mu$-$CH_3COO)_8$] (octakis(μ-acetato-O,O') tetraplatinum(II)) which was employed as a precursor in this study has a square framework composed of four Pt atoms with strong metal-metal bonds and coordinated by eight bridging acetate groups. Yamaguchi et.al. reported facile regioselective ligand substitution for the in-plane bridging acetate in the Pt cluster[95, 96]. From those properties, it was expected that the catalysts would exhibit unique catalytic properties.

In Chapter 6, Pt_4-cluster/SiO_2 catalyst, prepared from the [$Pt_4(\mu\text{-}CH_3COO)_8$] cluster, has shown remarkably high activity with 100% selectivity to CO_2 and H_2 for formic acid decomposition as compared with a conventional Pt particle/SiO_2 catalysts. In order to elucidate the genesis and mechanism for the catalysis of Pt_4-cluster/SiO_2, the samples were characterized by kinetics, Pt L_3-edge EXAFS, and FT-IR. EXAFS and IR data revealed that the surface structure of the catalyst changed from tetramer to dimer during an induction period, then to monomer which was active for the catalysis. Eventually Pt particles were formed and the catalyst was deactivated. The structural transformations of the Pt_4-cluster/SiO_2 catalyst are discussed in relation to the catalytic reaction profiles.

$Pt_4(\mu\text{-}CH_3COO)_8$ dispersed on $\alpha\text{-}Al_2O_3$ also showed a high catalytic activity for HCOOH decomposition reaction with selectively to CO_2 and H_2. The initial rate for the formation of CO_2 per Pt_4 (turnover frequency) on $Pt_4(\mu\text{-}CH_3COO)_8/\alpha\text{-}Al_2O_3$ is twice larger than the maximum reaction rate on the $Pt_4(\mu\text{-}CH_3COO)_8$ /SiO_2.

In Chapter 7, in order to obtain more precise structural information, therefore, I investigated the active sites structure of $Pt_4(\mu\text{-}CH_3COO)_8$ dispersed on $\alpha\text{-}Al_2O_3$ by in-situ polarization-dependent total reflection fluorescence XAFS(EXAFS and XANES) techniques. To examine the active site, I choose an $\alpha\text{-}Al_2O_3$ (0001) single crystal surface as support and then deposited $Pt_4(\mu\text{-}CH_3COO)_8$ on it. The measurements were carried out by using the in-situ PTRF-XAFS chamber[49].

Alumina, Al_2O_3, is an extremely important ingredient in ceramics, catalysts, integrated circuit manufacture, etc. There are several polymorphs of Al_2O_3, and the most stable one is corundum, $\alpha\text{-}Al_2O_3$. XPS and UPS measurements presented the valance-band electronic structure of single-crystal $\alpha\text{-}Al_2O_3$ (0001)[97-99]. Several qualitative LEED[100-102] studies and ab-initio calculations [103, 104]on $\alpha\text{-}Al_2O_3$ (0001) surface were performed. $\alpha\text{-}Al_2O_3$ (0001) surface has often been chosen for studies of metal-oxide interactions as follows. A particle-size effect for Pt and Rh on the substrate was investigated by Altman[105]. Cordatos et. al. reported that the effect of

particle size on the desorption properties of Pd/α-Al_2O_3 (0001) for NO, CO and H_2 is be related to the morphology of Pd sites[106]. Growth of copper on α-Al_2O_3 (0001) was rmonitored by means of surface sensitive X ray absorption spectroscopy (SEXAFS) at Cu K-edge [107]. It was suggested that there coexisted copper dimers and very small copper nanoclusters weakly bonded to the surface Al atoms. On the other hand, Shirai et al. measured PTRF-EXAFS spectra for Co oxides on α-Al_2O_3 (0001)[47]. It was reported that Co atoms occupied the threefold hollow sites of α-Al_2O_3 (0001) as monomers, which were aggregated to form small spinel-like particles by oxidation at 873 K.

In Chapter 7, it was found that the Pt_4 cluster framework was destroyed upon deposition of $Pt_4(\mu\text{-}CH_3COO)_8$ on α-Al_2O_3 at room temperature. The isolated Pt species were converted to one-atomic layer Pt rafts with the Pt-Pt distance of 0.273 nm when the Pt species were treated with H_2 at 373 K. It was suggested that raft-like Pt clusters were stabilized by the formation of direct Pt-O-Al bonding with the α-Al_2O_3 surface. The raft-like Pt clusters were redispersed to isolated oxidized Pt species by reaction with NO. They were also transformed to 3-dimensional Pt particles by reduction with H_2 at 773 K.

References

[1] G. A. Somorjai, *Chemistry in Two Dimensions: Surfaces* (Cornell University Press, Ithka, 1981).

[2] G. Ertl, *J.Mol.Catal.* **74**, 1 (1992).

[3] Y. Iwasawa, *Catalysis Today* **18**, 21 (1993).

[4] M. Akimoto and E. Echigoya, *J. Catal.* **29**, 191 (1973).

[5] D. Vanhove and M. Blanchard, *J. Catal.* **37**, 6 (1976).

[6] K. Hauffe, H. Raveling, and B. Bunsenges, *Phys. Chem.* **84**, 912 (1980).

[7] G. C. Bond and K. Bruckman, *Faraday Disc. Chem. Soc.* **72**, 235 (1981).

[8] F. Roozeboom, D. D. Cordingley, and P. J. Gellings, *J. Catal.* **68**, 464 (1981).

[9] B. K. Teo, *EXAFS Spectroscopy: Basic Principles and Data Analysis* (Springer-Verlag, Berlin, 1986).

[10] Y. Iwasawa, in *World Scientific Series on Synchrotron Radiation Techniques and Applications*, edited by D. H. Bilderback, K. O. Hodgeson, M. P. Kiskinova and R. Rosei (World Scientific, Singapore, 1996), Vol. 2, p. 410.

[11] D. C. Koningsberger and R. Prins, *X-ray absorption, Principles, applications, techniques of EXAFS, SEXAFS, and XANES* (John Wiley & Sons, New York, 1988).

[12] B. C. Gates, L. Guczi, and H. Knozinger, in *studies in surface science and catalysis* (Elsevier, Amsterdom, 1986).

[13] S. Kawai, O. Alexeev, M. Shelef, and B. C. Gates, *J. Phys. Chem.* **99**, 6926 (1995).

[14] K. Asakura, K.-K. Bando, and Y. Iwasawa, *J. Chem. Soc. Faraday Trans.* **86**, 2645 (1990).

[15] D. C. Koningsberger, J. B. A. D. van Zon, H. F. J. van't Blik, G. J. Visser, R. Prins, A. M. Mansour, D. E. Sayers, *et al.*, *J.Phys.Chem.* **89**, 4075 (1985).

[16] Y. Iwasawa, K. Asakura, H. Ishii, and H. Kuroda, *Z.Phys.Chemie Neue Folge* **144**, 105 (1985).

[17] K. Tomishige, K. Asakura, and Y. Iwasawa, *Chem.Lett.* 235 (1994).

[18] D. W. Goodman, *Acc.Chem.Res.* **17**, 194 (1984).

[19] D. W. Goodman, *J. Phys. Chem.* **100**, 13090 (1996).

[20] E. I. Altman and R. J. Gorte, *Surf..Sci.* **195**, 392 (1988).

[21] L. Atanasoska, R. T. Atanasoski, F. H. Pollak, and W. E. Ogrady, *Surf..Sci.* **230**, 95 (1990).

[22] P. J. Berlowitz, C. H. F. Peden, and D. W. Goodman, *J.Phys.Chem.* **92**, 5213 (1988).

[23] C. T. Campbell and A. Ludviksson, *J.Vac.Sci.Technol* **12**, 1825 (1994).

[24] H. Onishi and Y. Iwasawa, *Phys.Rev.Lett.* **76**, 791 (1996).

[25] R. C. Yates, J. E. Turner, A. J. Gellman, and G. A. Somorjai, *Surf.Sci.* **149**, 175 (1985).

[26] H. Onishi, T. Aruga, and Y. Iwasawa, *J. Am. Chem. Soc.* **115**, 10460 (1993).

[27] Y. Iwasawa, in *World Scientific Series on Synchrotron Radiation Techniques and Applications*, edited by D. H. Bilderback, K. O. Hodgeson, M. P. Kiskinova and R. Rosei (World Scientific, Singapore, 1996), Vol. 2, p. 410.

[28] S. M. Heald and E. A. Stern, *Phys. Rev. B* **17**, 4132 (1978).

[29] B. K. Teo and P. A. Lee, *J..Am. Chem.Soc* **101**, 2815 (1979).

[30] P. H. Citrin, *Phys.Rev.B* **31**, 700 (1985).

[31] R. Barchewiz, M. Cremonese-Visicato, and G. Onori, *J.Phys.Chem.* **11**, 4439 (1978).

[32] P. H. Citrin, *Surf.Sci.* **184**, 109 (1987).

[33] H. Oyanagi, R. Shioda, Y. Kuwahra, and K. Haga, *J. Synchrotorn Rad.* **2**, 99 (1995).

[34] J. Stohr, R. Jaeger, J. Feldhaus, S. Brennan, D. Norman, and G. Apai, *Appl. Optics* **19**, 3911 (1980).

[35] J. Stohr and R. Jaeger, *J.Vac.Sci.Technol.* **21**, 619 (1982).

[36] J. Stohr, C. Noguera, and T. Kendelewicz, *Phys.Rev.B* **30**, 5571 (1984).

[37] J. Jaklevic, J. A. Kirby, M. P. Klein, A. S. Robertson, G. S. Brown, and P. Eisenberger, *Solid State Communications* **23**, 679 (1977).

[38] S. M. Heald, E. Keller, and E. A. Stern, *Phys. Lett.* **A 103**, 155 (1984).

[39] S. M. Heald and E. A. Stern, *Phys. Rev.B* **16**, 5549 (1977).

[40] J. Stohr, in *X-ray absorption Principles, Applications, Techniques of EXAFS, SEXAFS, and XANES.*, edited by R. P. D.C.Koningsberger (A John Wiley & SONS, New York, 1988), Vol. 92, p. 443.

[41] T. Ohta, K. Asakura, and T. Yokoyama, *Application to Surface Structure Analyses* (Elsevier, Amsterdam, 1996).

[42] L. G. Parratt, *Phys.Rev.* **95**, 359 (1954).

[43] M. Shirai, K. Asakura, and Y. Iwasawa, *Chem. Lett.* 1037 (1992).

[44] M. Shirai, K. Asakura, and Y. Iwasawa, *Chem. Lett.* **15**, 247 (1992).

[45] K. Asakura, M. Shirai, and Y. Iwasawa, *Catal. Lett.* **20**, 117 (1993).

[46] M. Shirai, K. Asakura, and Y. Iwasawa, *Jpn. J. Appl. Phys* **32**, 413 (1993).

[47] M. Shirai, T. Inoue, H. Onishi, K. Asakura, and Y. Iwasawa, *J. Catal.* **145**, 159 (1994).

[48] M. Shirai, K. Asakura, and Y. Iwasawa, *Catal. Lett.* **26**, 229 (1994).

[49] M. Shirai, M. Nomura, K. Asakura, and Y. Iwasawa, *Rev. Sci. Instruments* **66**, 5493 (1995).

[50] M. Shirai, W.-J. Chun, K. Tomishige, K. Asakura, and Y. Iwasawa, *Catalytic Science and Technology,* (Kodansha.,1995), Vol. 1, 263.

[51] K. Asakura, K. Tomishige, M. Shirai, W.-J. Chun, T. Yokoyama, and Y. Iwasawa, *Physica B* **208&209**, 637 (1995).

[52] W.-J. Chun, M. Shirai, K. Tomishige, K. Asakura, and Y. Iwasawa, *Journal of Molecular Catalysis A: Chemical* **107**, 55 (1996).

[53] C. R. Adams and T. S. Jennings, *J. Catal.* **2**, 63 (1963).

[54] J. D. Krenze and G. W. Keulks, *J. Catal.* **61**, 316 (1980).

[55] J. D. Burrington, C. T. Kartisch, and R. K. Graseli, *J. Catal.* **81**, 489 (1983).

[56] D. Vanhove, Op, S. R., and Fernandez, A., Blanchard, M., *J. Catal.* **57**, 253 (1979).

[57] T. Ono, Y. Kubogawa, H. Miyata, and Y. Nakagawa, *Bull. Chem. Soc. Jpn* **57**, 1205 (1984).

[58] S. Okazaki, M. Kunasaka, M. Yoshida, J. Kosaka, and K. Tanabe, *I&EC Prod. Res. Dev.* **20**, 301 (1981).

[59] S. Matsuda and A. Kato, *Appl. Catal.* **8**, 149 (1983).

[60] K. Tanaka and K. I. Tnaka, *Chem. Soc., Chem. Commun.* **748**, (1984).

[61] K. Y. S. Ng and E. J. Gulari, *J. Catal.* **95**, 33 (1985).

[62] H. Shimada, T. Sato, Y. Yoshimura, J. Hiraishi, and A. Nishijima, *J. Catal.* **110**, 275 (1988).

[63] Y. C. Liu, G. L. Griffin, S. S. Chan, and I. E. Wachs, *J. Catal.* **94**, 108 (1985).

[64] G. C. Bond, S. Flamerz, and R. Shukri, *Faraday discuss.Chem. Soc.* **87**, 65 (1989).

[65] C. Martin, I. Martin, and V. Rives, *J. Chem. Soc. Faraday Tran.* **89**, 4131 (1993).

[66] I. E. Wachs, *Catalysis Today* **27**, 437 (1996).

[67] C. V. Ca'ceres, J. L. G. Fierro, J. La'zaro, A. L. Agudo, and J. Soria, *J. Catal.* **122**, 113 (1990).

[68] T. Machej, B. Doumain, B. Yasse, and B. Delmon, *J. Chem. Soc. Faraday Trans. 1* **84**, 3905 (1988).

[69] D. S. Kim, Y. Kurusu, I. E. Wachs, F. D. Hardcatle, and K. Segawa, *J. Catal.* **120**, 325 (1989).

[70] R. B. Quincy, M. Houalla, A. Proctor, and D. M. Hercules, *J. Phys. Chem.* **94**, 1520 (1990).

[71] K. Y. S. Ng and E. Gulari, *J. Catal.* **92**, 340 (1985).

[72] R. B. Quincy, M. Houalla, and D. M. Hercules, *J. Catal.* **106**, 85 (1987).

[73] D. S. Kim, I. E. Wachs, and K. Segawa, *J. Catal.* **146**, 268 (1994).

[74] J. C. Volta and J. L. Portefaix, *Appl. Catal.* **18**, 32 (1985).

[75] H. Shimada, N. Matsubayashi, T. Sato, T. Yoshimura, and A. Nishijima, *J. Catal.* **138**, 746 (1992).

[76] J. Evans, B. E. Hayden, and G. Lu, *Surf. Sci.* **360**, 61 (1996).

[77] B. L. Machoff, J. Pan, and T. E. Madey, *Surf. Sci.* **259**, 190 (1991).

[78] H. Onishi, Y. Yamaguchi, K. Fukui, and Y. Iwasawa, *J. Phys.Chem.* **100**, 9582 (1996).

[79] H. Onishi, K. Fukui, and Y. Iwasawa, *Colloids And Surfaces A Physicochemical And Engineering Aspects. Apr* **109**, 335 (1996).

[80] H. Onishi and Y. Iwasawa, *Surf. Sci.* **358**, 773 (1996).

[81] G. Charlton, P. B. Hows, C. L. Nicklin, P. Steadman, J. S. G. Tayor, C. A. Muryn, S. P. Harte, *et al.*, *Phys. Rev. Lett.* **78**, 495 (1997).

[82] G. Pacchioni, A. M. Ferrari, and P. S. Bagus, *Surf. Sci.* **350**, 159 (1996).

[83] K. D. Schierbaum and W. X. Xu, *International Journal Of Quantum Chemistry* **57**, 1121 (1996).

[84] H. Onishi, T. Aruga, C. Egawa, and Y. Iwasawa, *Surf.Sci.* **199**, 54 (1988).

[85] H. Onishi, T. Aruga, C. Egawa, and Y. IWasawa, *Surf.Sci.* **233**, 261 (1990).

[86] H. Onishi and Y. Iwasawa, *Catal. Lett.* **38**, 89 (1996).

[87] K. D. Schierbaum, S. Fischer, M. C. Torquemada, J. L. Desegovia, E. Roman, and J. A. Martingago, *Surf. Sci.* **345**, 261 (1996).

[88] H. Ishii, K. Asakura, Y. Kitajima, M. Funabashi, H. Namba, N. Kosugi, T. Ohta, and H. Kuroda, in *X-ray absorption fine structure*, edited by S. Hasnain (Ellis-Horwood, 1991), p. 257.

[89] H. Namba, Y. Okawa, and H. Kuroda, *Surf.Sci.* **242**, 32 (1991).

[90] K. Asakura, H. Ishii, S. Konishi, Y. Kitajima, T. Ohta, and H. Kuroda, *Physica B* **208 & 209**, 465 (1995).

[91] P. Maes, J. J. F. Scholten, and P. Zwietering, *Adv. Catal.* **14**, 35 (1963).

[92] J. M. Trillo, G. Munuera, and J. N. Craido, *Catal. Rev.* **7**, 51 (1972).

[93] R. J. Madix, *Surf. Sci.* **89**, 540 (1979).

[94] F. Solymosi, J. Kiss, and I. Kova'cs, *J. Phys. Chem.* **92**, 796 (1988).

[95] T. Yamaguchi, Y. Sasaki, A. Nagasawa, T. Ito, N. Koga, and K. Morokuma, *Inorg. Chem.* **28**, 4311 (1989).

[96] T. Yamaguchi, Y. Sasaki, and T. Ito, *J. Am. Chem. Soc.* **112**, 4038 (1990).

[97] W. J. Gignac, R. S. Williams, and S. P. Kowalczyk, *Phys. Rev. B* **32**, 1237 (1985).

[98] F. S. Ohuchi and M. Kohyama, *J. Amer. Ceram. Soc.* **74**, 1163 (1991).

[99] E. I. Altman and R. J. Gorte, *Surf.Sci.* **216**, 386 (1989).

[100] M. Gautier, J. P. Duraud, L. Pham Van, and M. J. Guittet, *Surf. Sci.* **250**, 71 (1991).

[101] M. Vermeersch, R. Sporken, P. Lambin, and M. J. Guittet, *Surf. Sci* **235**, 5 (1990).

[102] M. Gautier, J. P. Duraud, and L. Pham Van, *Surf. Sci.* **250**, 71 (1991).

[103] C. Pisani, M. Causa', R. Dovesi, and C. Roetti, *Prog. Surf. Sci.* **25**, 119 (1987).

[104] M. Causa', R. Dovesi, C. Pisani, and C. Roetti, *Surf. Sci.* **215**, 259 (1989).

[105] E. I. Altman and R. J. Gorte, *Surf.Sci.* **216**, 386 (1989).

[106] H. Cordatos, T. Bunluesin, and R. J. Gorte, *Surf. Sci.* **323**, 219 (1995).

[107] S. Gota, M. Gautier, L. Douillard, N. Thromat, J. P. Duraud, and P. Fevre, *Surf.Sci.* **323**, 163 (1995).

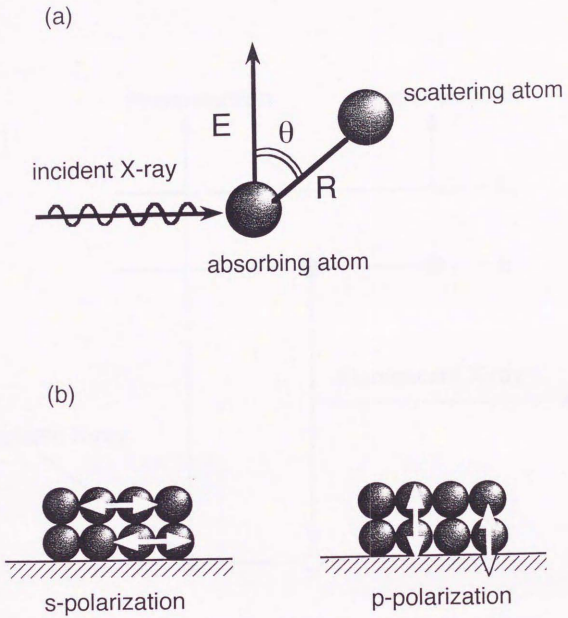

Figure 1. Scheme of Polarization-dependent X-ray absorption:
(a) A photon absorption; (b) s-polarization; (c) p-polarization.

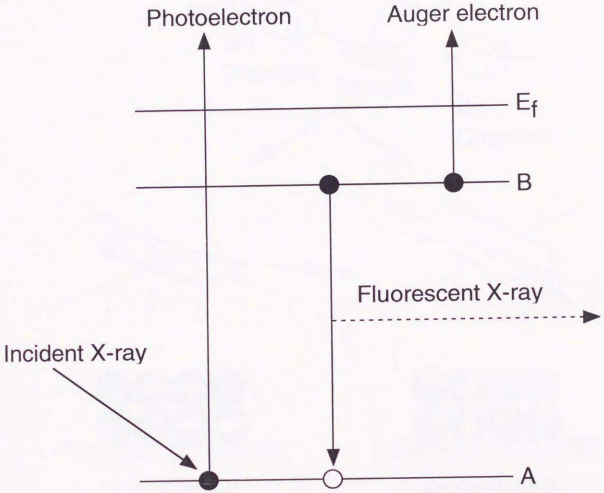

Fig.2 Scheme of X-ray absorption precess by a core electron and annihilation precoess of the created core hole.

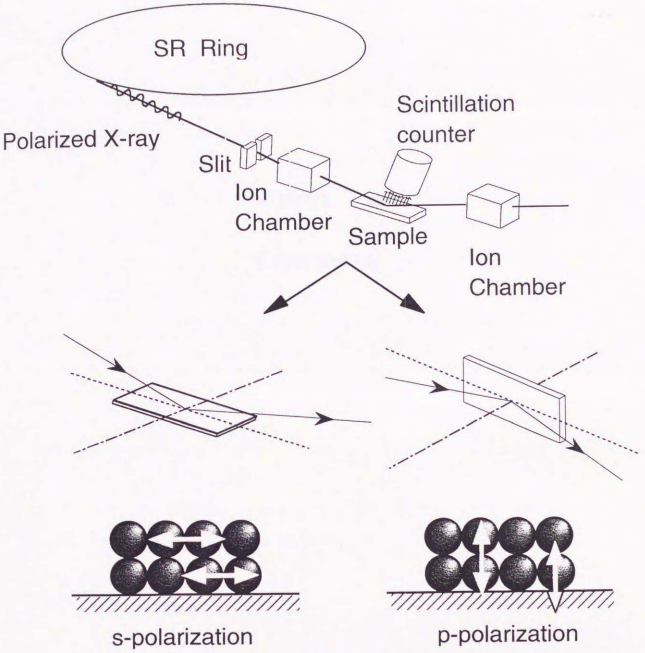

Fig.3 Polarization-dependent Total-Reflection Fluorescence XAFS.

Chapter 2

Experimental

PTRF-EXAFS measurements in this thesis were carried out at Beam Line 7C(BL-7C) for $Pt_4(\mu\text{-}CH_3COO)_8$ on an $\alpha\text{-}Al_2O_3$ (0001) and Beam Line 14A(BL14A) for Mo oxides on TiO_2(110) of the Photon Factory in the National Laboratory for High Energy Physics (KEK-PF). In this chapter, each beam line will be briefly described. I made the in-situ PTRF-XAFS cell for carrying out Mo K-edge PTRF-XAFS measurements at BL14A section(2.2.1). In order to set up the cell , I designed a cell which can be easily set up on a high-precision horizontal-type 4-circle goinometer, adjusting a total-reflection condition. In section 2.2.2, in-situ PTRF-XAFS chamber applied to the $Pt_4(\mu\text{-}CH_3COO)_8$ / $\alpha\text{-}Al_2O_3$ (0001) system will be mentioned.

2.1 About Beam Line

2.1.1 Beam Line 14A(BL14A)

Beam Line 14A has been designed for EXAFS as well as protein crystallography at high photon energies. Wiggler radiation with a 20-keV critical energy is highly polarized in the vertical direction. The vertical polarization allows to design the whole optical configuration laid out horizontally so that goniometers can be rotated rapidly with high precision. By taking the advantage of the wiggler radiation, a diffractometer station equipped with a double-crystal monochromator and a focusing mirror was built at BL14A[1]. A double -crystal monochromator is installed at the 12-m point from the source point of the wiggler as shown in Fig.1. Among the total of 9-mrad radiation available from the wiggler, bottom 1.28 mrad beam is accepted by the monochromator. Two goinometers of the monochromator are laid out in the horizontal plane. Two flat silicon crystals, 70 or 120 mm long, 30 mm wide, and 6 mm thick, are arranged in parallel to produce double reflection through three motions: rotation of the first crystal, and rotation and 1.7 m translation of the second one. The separation between the

incident and the output beams is 450 mm in order to install a four-circle diffractomater. The five motions of the monochromator(the remaining two tilt the axes on the crystals to move the reflected beam vertically) are driven concurrently by on-line-control stepping motors. The energy ranges converged are from 5.1 to 19 keV with Si(111), from 12.9 to 48 keV with Si(311), and from 22.7 to 84.5 keV with Si(553). In order to eliminate higher order harmonics, a toroidal mirror system which performs a 1:1 focusing of x rays is installed at 15.5 m from the source. For the system, Pt-coated cylindrical mirror blank of fused quartz(1m long, 69.9 mm radius) was employed. All procedures for adjustment of the monochromator as well as the diffractomator were controlled by a computer system. The radiation shielding hutch is located at ca. 30 m far from the source and its overall size is 2.4 m x 2.4 m.

A horizontal-type four-circle diffractometer(Fig.2) is equipped in a radiation safety hutch installed at beam line 14A for rapid and precise data collection[1]. The vertically-polarized nature of the vertical-wiggler beam allows to set up a conventional diffractometer configuration. The motions of the four axes are driven by stepping motors and are monitored by encoders to ensure correct rotations. Maximum rotation speeds are 100 deg/min for 2θ axis, 500 deg/min for ω, and 2000 deg/min both for χ and for ϕ. The ϕ-circle is on the center of the χ-circle. Both circles can be rotated freely but the ϕ rotation has to be driven simultaneously in accordance with the χ rotation. The inner diameter of the χ-circle is 280 mm which allows mounting of carious attachments. The 2θ axis was reinforced so that it can rotate a 60 cm long counter. The incident assembly of the slit system consists of a shutter, two positioning half slits, three changeable receiving slits, and a changeable attenuator. For monitoring the intensity, it was employed an ionization chamber as well as a NaI(Tl) scintillation detector for EXAFS measurements.

The control and measuring system for the station equipments is connected to a IBM/AT computer. Interfacing the computer utilizes the IEEE Standard 488-1975 General Purpose Interface Bus(GPIB). The intensity measuring system is controlled by

a CAMAC(IEEE Standard 583-1982) system, which is also interfaced to the computer through GPIB.

2.1.2 Beam Line 7C(BL7C)

The beam line(Fig.3) is designed to obtain clear intense monochromatic beam at rather low energy region by using a sagittal focusing double crystal monochromator and a focusing double mirror system: the photon flux is 10^{11}/ sec and the ratio of higher order is approx. 10^{-5} compared with the fundamental beam[2, 3]. The radiation is horizontally focused(4 mrad) by a sagittal focusing double-crystal monochromator and by a focusing double mirror vertically. A focusing double mirror system is designed to eliminate higher-order harmonics and focus the beam vertically. It consists of two parallel set flat fused quartz mirrors(80 mm(width) x 30 mm(thickness) x 700 mm(length)). The detection and data handling system for normal XAFS measurements in a transmission mode, that is, the ion current is amplified by a current amplifier(Keithley 427), converted to a pulse train by a V/F converter(Tsuji NVF-01), then the pulses are counted by a scalar(ORTEC 974). The counted data are read by a 16-bit microcomputer(NEC PC-9801). All procedures for monochromator as well as data handling were controlled by the microcomputer.. The size of radiation shielding hutch is 3.0 m x 2.1 m x 2.5 m.

2.2 About in-situ PTRF-XAFS Measurement Apparatus

2.2.1 in-situ PTRF-XAFS cell for Mo oxides on TiO_2(110) at BL14A

I designed an in-situ PTRF-XAFS cell for BL14A on the following purposes: (1) easy set up on the high-precision horizontal-type 4-circle goinometer; (2) easy adjustment of a total-reflection condition (a critical angle is 0.17 mrad for Mo K-edge). The cell is consist of two small stainless steel based compartments and a transporting device(Fig.4). Sample was attached on a holder in a preparation compartment which can be heated up to 873 K and also treated with reaction gases through a leak valve. After a sample preparation, the sample was moved to a measurement compartment by a transporting unit without exposure to air. The measurement compartment is designed to be fixed on the high precision 4-axis goniometer of BL14A and also for low temperature measurement (70 K) by connecting a cryocooler(CTI Cryogenics Co.). Kapton film was used for the windows of the measurement compartment. In order to improve the quality of XAFS signal, we applied a small NaI(Tl) scintillation counter(ϕ 14 mm) for monitoring X-ray fluorescent signal from the sample. We can remove the diffraction from the spectra simply by putting the detector at an appropriate position. The whole set up of the in-situ PTRF-XAFS apparatus is shown in Fig.5.

2.2.2 in-situ PTRF-XAFS measurement chamber for $Pt_4(\mu\text{-}CH_3COO)_8$ on an α-Al_2O_3 (0001)

The in-situ PTRF-XAFS measurement chamber (Fig.6) was designed to satisfy the following purposes: (1) to carry out in-situ preparation and measurement of catalyst model surfaces; (2) to adjust total reflection conditions and to change the orientation of the sample to the electric-field vector of the incident x-rays without exposure to air[4]. The system consists of four parts; sample preparation, PTRF-XAFS measurement, total-

reflection adjustment and vacuum system. Since metal is deposited on flat substrates by vacuum evaporation of metal wire or a chemical vapor deposition(CVD) method of organometallic complexes, the chamber is separated into two parts by a gate valve in order to avoid a contamination of Be windows. Since the irradiated area becomes large if the incident x-ray has a small glancing angle, thus, larger sample is desirable. A sample as long as 20-50 mm can be used for whole incoming x-ray to irradiate the sample with a 4 mrad glancing angle in the experiment where the beam size of the incident x-ray is 0.1 mm x 0.1 mm. The sample can be heated up to 873 K from the backside using a Ta resistive heating sheet and also cooled down to 100K by liquid N_2 . The sample holder is fixed to a cylinder which is connected to two bearing rotors. The axis of the cylinder is set on the x-ray light axis. By the linear motion rod F is moved independently from the sample holder, the cylinder can be rotated by 100 deg and the sample orientation relative to the polarized x-ray can be altered from the parallel arrangement to the perpendicular one as shown in Fig.7.

To attain a total-reflection condition, adopted was the XYZ and rotary tables on which the whole chamber is mounted(Fig.6). The XYZ and rotation tables are driven by stepping motors(Oriental Motors Co.) controlled with a personal computer (NEC PC9801). The top of the total-reflection adjustment part is the rotation table that can be driven with a precision of 0.02 mrad. On the bottom, X and Y tables are installed. In the middle of them, the Z table composed of three vertical jacks(Mitsutoyo Co.)are positioned in an equilateral triangle; one in the front side and the other two in the back side. The center of a sample is put over the mass center of this triangle. Total-reflection conditions for s polarization and for p polarization with respect to the surface are adjusted by the use of the three vertical jacks and the X-table as shown in Fig. 8. When the sample is tilted by the three vertical jacks, the X-table is moved by a calculated amount to ensure that the x-ray beam hits on the same position of the sample.

The prepared sample is transferred to the lower part of the chamber by a long flexible bellows attached to the top side of the preparation chamber during PTRF-XAFS

measurements. The lower part(PTRF-XAFS measurements) has three Be windows(thickness = 25 μm, Electrofusion Corporation Co. Purity 99.8 %) for incident, reflected, and fluorescent x-rays. The diameter of the Be window for the fluorescent x-ray is 50 mm in diameter and it is possible to bring the Be window close to the sample with a linear motion drive. Thus we can take out 50%/4πst of the total fluorescence x-ray when the sample surface is set parallel to the fluorescence window. Both parts are pumped out from the side ports by a diffusion pump and a rotary pump. The vacuum system is connected to the chamber by flexible tubes in order to diminish vibrational noises. Reaction gases can be introduced into the chamber through a leak valve. Thus, PTRF-XAFS spectra can be obtained under various conditions from high vacuum (1 x 10^{-9} Pa) to high pressure (1 x 10^{5} Pa) and from low temperature (100 K) to high temperature (873 K).

References

[1] Y. Satow and Y. Iitaka, *Rev. Sci. Instrum.* **60**, 2390(1989).

[2] M. Nomura and A. Koyama, *X-ray Absorption Fine Structure* (Ellis Horwood, Chichester, 1991).

[3] K. Nomura, A. Koyama, and M. Sakurai, *KEK Report* **91-1**, (1991).

[4] M. Shirai, M. Nomura, K. Asakura and Y. Iwasawa, *Rev. Sci. Instruments* **66**, 5493 (1995).

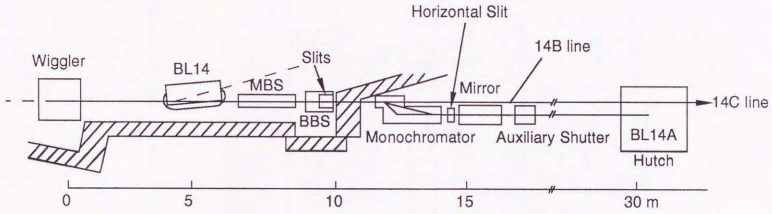

Fig.1 Arrangement of beam line 14A(BL14A), viewed down to the horizontal plane.
Both the main beam shutter(MBS) in the beam line front end and the branch beam shutter(BBS) are installed inside the shielding wall. The auxiliary downstream shutter is used to keep the monochromator crystal exposed to the photon beam during access to the hutch.

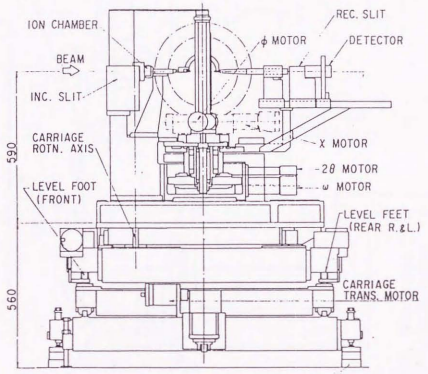

Fig.2 Side view of the four-circle diffractometer installed in BL14A.

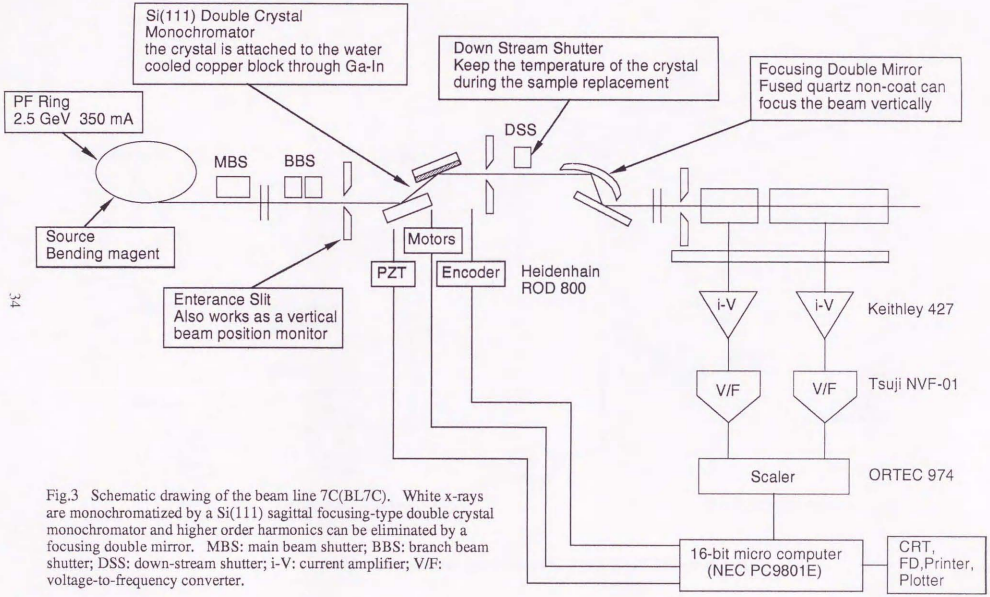

Fig.3 Schematic drawing of the beam line 7C(BL7C). White x-rays are monochromatized by a Si(111) sagittal focusing-type double crystal monochromator and higher order harmonics can be eliminated by a focusing double mirror. MBS: main beam shutter; BBS: branch beam shutter; DSS: down-stream shutter; i-V: current amplifier; V/F: voltage-to-frequency converter.

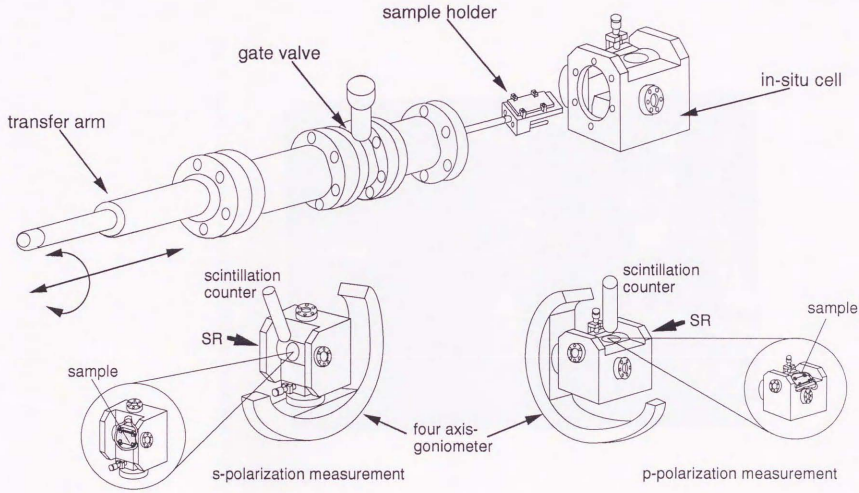

Fig.4 Schematic diagram for in-situ PTRF-XAFS cell for BL14A.

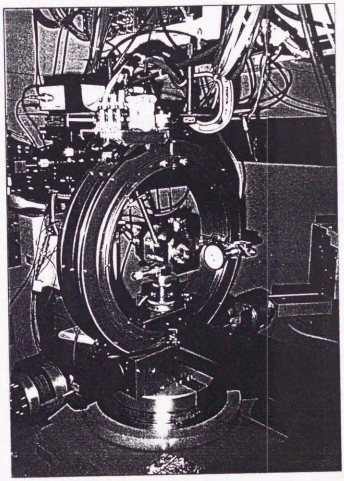

Fig. 5 Photograph of the in-situ PTRF-XAFS measurement at BL14A.

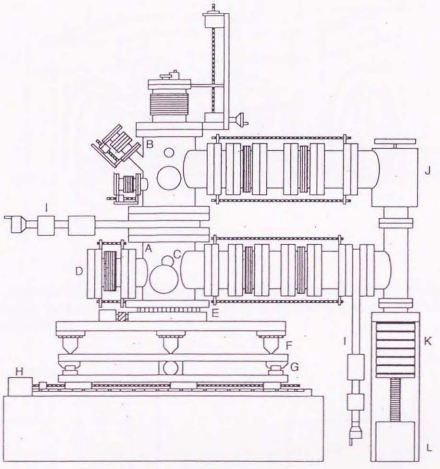

Fig.6 Layout of in-situ PTRF-XAFS chamber; A: measurement chamber; B: preparation chamber; C: window for reflected x-ray ; D: window for the fluorescent x-ray; E: rotation table; F: Z-table; G: X-table; H: Y-table; I: gate valve; J: angle valve; K: diffusion pump; L: rotary pump.

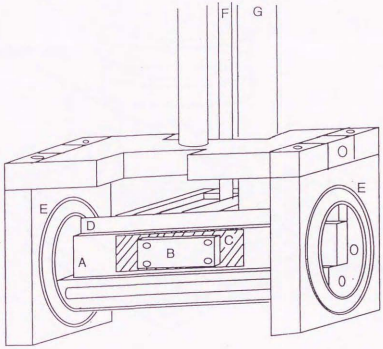

Fig.7 Layout of the sample holder; A: Alumina sheet; B: sample; C: Ta heater; D: Cylinder for a rotation of the sample; E: bearing rotors; F: linear motion rod; G: liquid N2 tube.

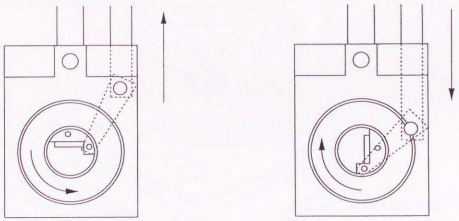

Fig. 8 Schematic diagram of rotation mechanism.

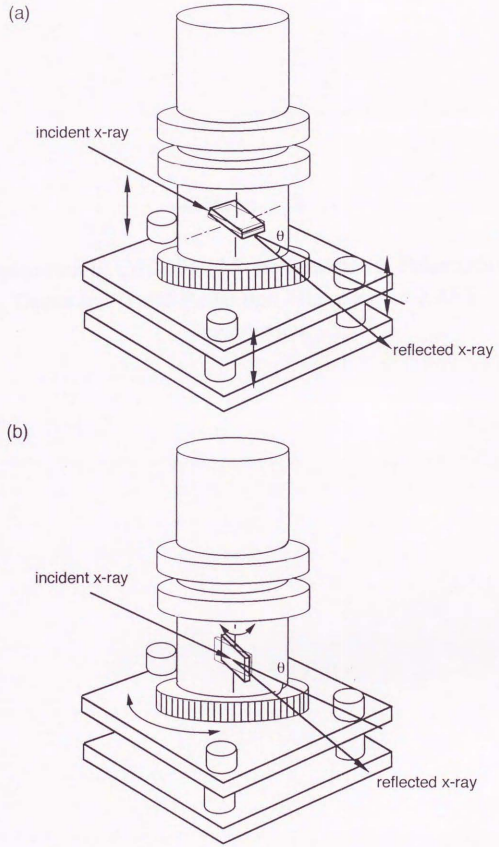

Fig.9 Total-reflection adjustment for s-polarization (a) and p-polarization(b) measurements.

Chapter 3

Application of CdTe Solid State Detector to Polarization-Dependent Total-Reflection Fluorescence XAFS Measurement

ABSTRACT

A CdTe solid state detector was applied to the measurements of polarization-dependent total-reflection fluorescence XAFS spectra. The data revealed that the detector has good sensitivity, and this, together with its compact size, make it appropriate for the in-situ measurements and removal of X-ray Bragg diffraction. The detector efficiently recorded the high-energy K-edge XAFS spectra for molybdenum oxides supported on TiO_2(110).

3.1 Introduction

X-ray Absorption Fine Structure(XAFS) spectroscopy is one of the most useful techniques for characterization of supported metal catalysts in that it can provide the information on bond lengths and coordination number around particular metal sites[1, 2]. Since the catalytic properties of supported metals and metal oxide are strongly affected by the morphology of the particle and the interaction with the support, it is indispensable to clarify the active-site structure. However, conventional XAFS spectroscopy using powder sample has the disadvantage of averaging XAFS information over all directions.

Applying polarized synchrotron radiation to a model catalyst with active sites on a flat surface, it has been possible to separate the information in directions parallel and perpendicular to the surface and to obtain the anisotropic structure of active sites by analyzing polarization-dependent XAFS spectra. The total-reflection fluorescence technique had also been applied as a surface sensitive technique for the heavy elements[3]. Under these consideration I have applied polarization-dependent total-reflection fluorescence XAFS(PTRF-XAFS) and successfully determined the three-dimensional model active-sites structure of catalysts supported on flat substrates such as α-Al_2O_3 and quartz[4-6].

I have employed a CdTe solid-state detector for the PTRF-XAFS measurements. CdTe is a II-VI semiconductor material having a band gap of 1.47 eV, which can be used

as a detector at room temperature[7-9]. Moreover, it has a high X-ray stopping power due to the high atomic number of the elements(Cd = 48, Te = 52) which is enough for developing a high sensitive PTRF-EXAFS system. In this chapter I report the application of the CdTe detector to a PTRF-XAFS study on molybdenum oxides supported on TiO_2(110).

3.2 Experimental

CDTE-XBE(Toyo Medic Co., Ltd., Japan)(Fig. 1), a CdTe solid-state detector, was used to monitor X-ray fluorescence signal from the sample. In this study I employed a CdTe single crystal(4 x 4 x 2 mm^3) detector for achieving high efficiency. The energy resolution of the detector is 4.5 keV at 54.8 keV. The PTRF-XAFS measurements were carried out at room temperature. The detector was placed as close as possible to the window of the in-situ cell where no Bragg diffraction having sharp directionality was observed.

Measurements were performed at BL14A of the Photon Factory in the National Laboratory for High Energy Physics(KEK-PF). A four-circle goniometer was used to set the particular orientation of the sample against the polarization direction of the incident X-ray and to achieve the total reflection condition. The incident X-ray was monitored by an ion chamber filled with Ar. The PTRF-XAFS spectra at Mo K-edge for molybdenum oxide on TiO_2(110) were obtained with the electric field vector parallel to [001] direction of TiO_2(110).

The TiO_2(110) single crystal(20 x 40 x 1 mm^3) (Earth Jewelry Co., Ltd., Japan) was annealed for 5 h at 823 K in air. Molybdenum oxide was supported on TiO_2(110) surface by an impregnation method using aqueous solution of heptaammonium molybdate, followed by calcination at 773 K. The sample was mounted in a small in-situ cell illustrated in Fig.2. Details of the sample preparation will be described in Chapter 4.

3.3 Results and Discussion

3.3.1 CdTe detector

Using the synchrotron radiation from BL14A at KEK-PF to excite the Ka fluorescence lines from molybdenum and titanium of the sample, it was compared the measurement of a benchmark with three different-sized($1 \sim 4\ mm^2$) CdTe detectors. The detector exhibited an energy resolution of ca. 4 keV FWHM for Mo Kα line. The 4 x 4 x 2 mm^3 Cd-Te single crystal was found to have good efficiency in Mo K-edge XAFS measurements. However, in the lower photon energy region below 10 keV, the pulse height of the X-ray fluorescence signal was at the same level as the noise. Thus, the application of a CdTe detector is limited to fluorescent X-ray measurement at energies higher than 10 keV.

3.3.2 Mo K-edge XAFS

I used a specially devised small cell for the Mo sample applicable to in-situ measurements as shown in Fig.2. Since the total counting rate is 10^3 - 2 x10^4 counts s^{-1} due to the small size of incident X-ray, it is desirable to place the detector as close as possible. Large detectors such as a solid-state detector or a conventional scintillation counter could not be placed close to the sample surface because of the geometrical hindrance of the in-situ cell. The small and light CdTe detector is an ideal solution in this sense. The CdTe detector was placed as close as to the window of the cell (within 1 mm) using a simple adjustment device. Since the Bragg diffraction has a sharp directivity, the adjustment device made it easy to find the non-Bragg parts of reciprocal space for the CdTe detector.

Fig. 3 (b) shows the PTRF-XANES spectra at the Mo K-edge in the 19950 ~ 20100 eV energy region recorded by the CdTe detector. The measuring time for each point was only 5 s. For comparison, the spectrum was also measured by a NaI(Tl)

scintillation counter (ϕ45 x 120 mm), as shown in Fig.3(a). Since the size of the scintillation counter was large, it was difficult to place even at 30mm to the window of the cell. Thus the signal-to-noise ratio of the spectrum was very low with the scintillation counter. It is clear that the quality of the spectra is much improved by employing the CdTe detector. The 1s $\rightarrow$ 5p/4d transition peak in the K-edge region can be seen distinctly seen in the case of the CdTe detector. The XANES spectrum indicates a Td structure around Mo atom[10].

3.4 Conclusions

The CdTe detector showed good efficiency and high cost-performance in measurement of in-situ PTRF-XAFS spectra. The small detector made it easy to avoid Bragg diffraction from the substrate by setting it an appropriate position and direction. The price of the detector including a preamplifier and a main amplifier was not high($5,000). The compact body and cheap price of the CdTe detector are a great advantage when constructing a multi-element detection system. However, the CdTe detector has a fatal disadvantage: owing to the high noise peak height in the low-energy region it is difficult to use the CdTe detector for elements with X-ray absorption edges lower than 10 keV.

References

[1] B. K. Teo, *EXAFS Spectroscopy: Basic Principles and Data Analysis* (Springer-Verlag, Berlin, 1986).

[2] D. C. Koningsberger and R. Prins, *X-ray absorption, Principles, applications, techniques of EXAFS, SEXAFS, and XANES* (John Wiley & Sons, New York, 1988).

[3] S. M. Heald, E. Keller, and E. A. Stern, *Phys. Lett.* **A 103**, 155 (1984).

[4] M. Shirai, K. Asakura, and Y. Iwasawa, *Chem. Lett.* **15**, 247 (1992).

[5] M. Shirai, T. Inoue, H. Onishi, K. Asakura, and Y. Iwasawa, *J. Catal.* **145**, 159 (1994).

[6] Y. Iwasawa, in *World Scientific Series on Synchrotron Radiation Techniques and Applications*, edited by D. H. Bilderback, K. O. Hodgeson, M. P. Kiskinova and R. Rosei (World Scientific, Singapore, 1996), Vol. 2, p. 410

[7] T. E. Schlesinger, R. B. James, P. Siffert, and L. Franks, in *Semiconductors for Room-Temperature Radiation detector Application.*(Material Research Society, 1993).

[8] P. Siffert, in *Cadmium Telluride Detector and Applications.*(Elsevier Science Publishing Co., Inc. , 1983).

[9] K. Zanio, in *Semiconductor and Semimetals.* (Academic press., 1978) .

[10] J. Evans, and J. F. W. Mosselmans, *J. Am Chem Soc.* **113**, 3737 (1991).

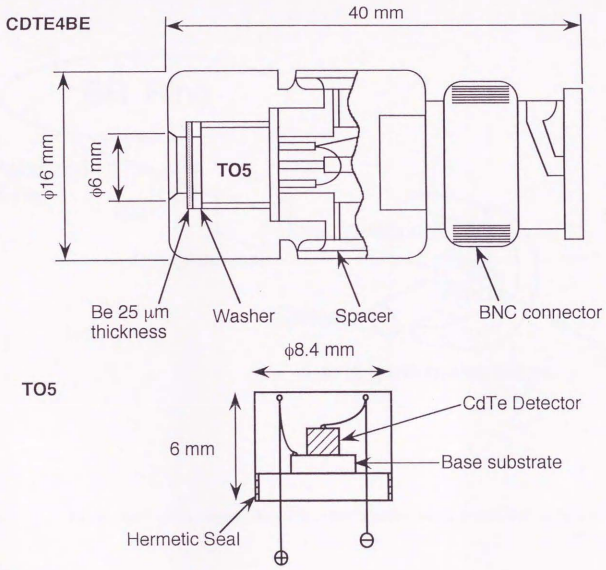

Fig. 1 Layout of a CDTE-XBE(CdTe solid-state detector) system.

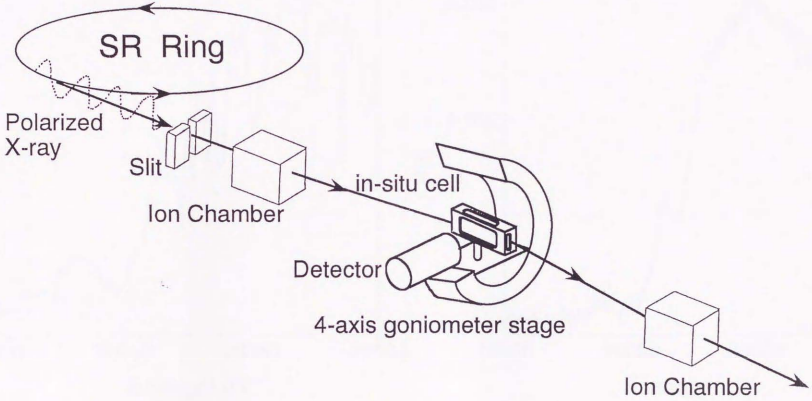

Fig. 2 A schematic diagram for a PTRF-XAFS measurement system with an in-situ cell.

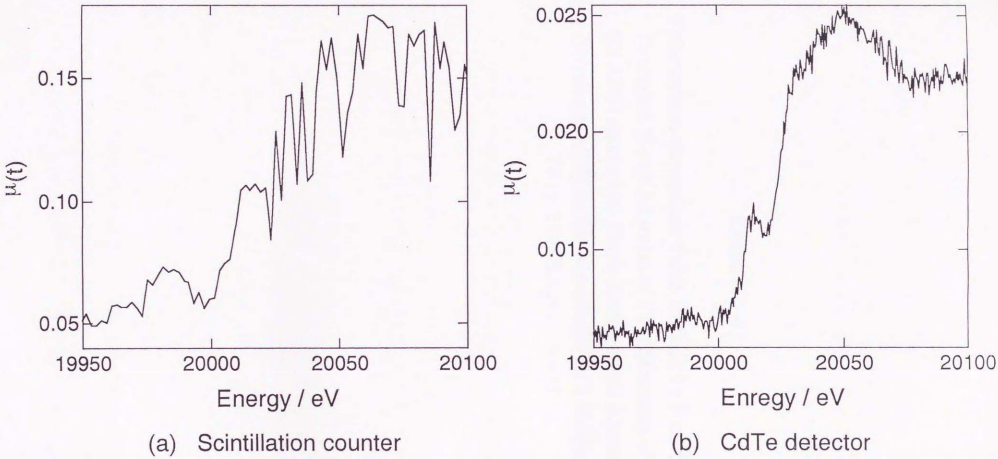

Fig. 3 Mo K-edge PTRF-XANES spectra for molybdenum oxide on TiO_2(110) recorded by a NaI scintillation counter(a) and a CdTe detector(b).

Chapter 4

Polarization-dependent Total-Reflection Fluorescence Extended X-ray Absorption Fine Structure (PTRF-EXAFS) Studies of Three-dimensional Anisotropic Structure Analysis for Mo oxides on a Rutile-type TiO_2(110) Single Crystal

ABSTRACT

Three dimensional structure analysis by means of polarization-dependent Total Reflection Fluorescence Extended X-ray Absorption Fine Structure(PTRF-EXAFS) was carried out to reveal the surface structure of Mo oxide species in its initial growing stage on a rutile TiO_2 (110) single crystal substrate. Since the substrate has the anisotropic surface property, the PTRF-EXAFS measurements were performed in three different directions by the polarized incident X-rays parallel to [1 $\bar{1}$ 0], [001], and [110] of TiO_2 (110). Comparing the observed data to the calculated data using FEFF 6.01 in the three directions, it was concluded that the Mo dimer species were formed on the surface with Mo-Mo bond (0.335 nm) parallel to the [1 $\bar{1}$ 0] direction and existing at 0.220 nm far from the surface of TiO_2 (110).

4.1 Introduction

To reveal the surface structure of active sites in industrial heterogeneous supported metal catalysts has been a topic of considerable interest from both fundamental and technological viewpoints. Most of supported metal catalysts involve metal particles deposited on oxide supports possessing high surface areas. The oxide supports not only work to disperse metal particles but also play a role to reform the morphology, orientations and electronic states of metal particles through metal-support interaction which is one of the most relevant factors to affect the activity and selectivity in heterogeneous catalysts.

Extended X-ray Absorption Fine Structure(EXAFS) is regarded as a useful method to obtain the information about the morphology of metal particles and metal-support bonding[1]. Particle morphology can be obtained by the analysis of the coordination number of metal-metal bonds. The distance of metal-support bonds can be determined by detecting the EXAFS signal of atoms(mostly oxygen) on the support

surface. The amplitude of EXAFS oscillation depends on the direction of X-ray electric-field vector, as given by equation (1)[2, 3],

$$\chi(k) = \sum \chi_j(k) \cos\theta_j \qquad (1)$$

where θ_j is the angle between the polarization vector and the j-th bond vector, and $\chi(k)$ and $\chi_j(k)$ are total EXAFS oscillation and EXAFS oscillation accompanied to the j-th bond, respectively.

When the polarization vector is parallel to the surface (s-polarization), only the bondings which laid parallel to the surface contribute to EXAFS signal. The bondings normal to the surface i.e., metal-support bonds, will be obtained when the polarization vector is perpendicular to the surface (p-polarization), selectively. However, it is not straightforward to obtain a precise structural information from a conventional EXAFS using a powder catalyst, where the angle dependence properties of EXAFS become nominal one. Employing a single crystal metal oxide as a support, the structural information on parallel and normal bonding to the surface can be independently obtained. However, there are a couple of problems employing a flat substrate as a support. First, concentration of surface species is very low, and thus it isn't available to measure in a transmission mode as in case of powder samples. Concentrations of monolayer metal on a flat surface are in the range 10^{14}-10^{15} atoms cm^{-2}, which is 4-5 orders of magnitude lower than those of metals for conventional catalysts in a powder form[4]. Usually fluorescence yield detection is more preferable for dilute samples than monitoring of direct absorption[5]. In a soft X-ray region, the fluorescence-detection mode successfully gives the EXAFS signals with high quality, and the polarization-dependent EXAFS studies determine the adsorption sites of lighter elements such as C, O, S, Cl, and P[6, 7].

Most of catalytically interesting elements placed their x-ray absorption edges at higher energies than 20 keV. Therefore, the fluorescence detection at the region works no more surface sensitive since the penetration depth of the incident beam becomes so large that the emitted fluorescence from the bulk substrates suffers detecting monolayer

species supported on the flat substrate.. Under a total-reflection condition that occurs when a x-ray hits on a flat substrate below a critical angle(δc), the incident x-rays are totally reflected and penetrate only a few nm into the bulk. Consequently, the scattering X-ray from the bulk is dramatically reduced, and surface sensitivity can be improved. When the fluorescence method is used with glancing incidence angle of X-ray satisfying a total reflection condition, it becomes a surface sensitive technique in the high energy region and suitable for the study of the structure of growing overlayers without long range order[8]. The technique called as polarization-dependent total-reflection fluorescence EXAFS (PTRF-EXAFS) method hereinafter has proved capable of determining asymmetric structure of Co oxides on α-Al_2O_3 (0001) and Cu oxides on α-quartz(0001)[9, 10].

Molybdenum oxide is a principal component in catalysts for the selective oxidation and ammoxidation of propylene as well as many other catalysts of industrial importance[11-13]. For titania-supported molybdenum oxide catalysts, Eon et al.[14] have suggested that molybdena-titania interaction leads to an epitaxial growth of molybdenum oxides over TiO_2. Delmon et al. also reported that Mo oxides expitaxially grow on TiO_2 from the results of TEM and XPS[15].

In this chapter I report the PTRF-EXAFS analysis of Mo oxide(0.2 ML) on TiO_2(110) surface in 3 different directions. Rutile TiO_2(110) has an anisotropic surface structure with alternative alignment of the bridging oxygen ridge and the groove composed of rows of five-fold coordinated Ti^{4+} cations along the [001] axis as shown in Fig. 1(a). The surface has been extensively investigated, and its electronic and geometric structures and adsorption properties have been characterized by various techniques such as LEED, XPS, MEED, SPM, SXRD and also ab-initio calculation[16-20]. Considering the anisotropic surface properties of TiO_2(110) surface, the characteristic growth of Mo oxides on the substrate might be expected if Mo oxides are deposited on it. Moreover, this work is the first report of the successful application of PTRF-EXAFS measurements for elements with high K-edge energies(over 20 keV).

The high K-edge EXAFS measurement in a total reflection condition has been believed to be quite difficult since an extremely small critical angle, typically 1.7 mrad, for satisfying a total reflection condition.

4.2 Experimental

4.2.1 Sample preparation

A rutile TiO_2(110) single crystal(20 x 40 x 1 mm^3)(Earth Jewelry Co., Ltd.; optical grade) polished was annealed for 2 h at 823 K in air. Mo was deposited with an ultra-pure aqueous solution of $(NH_4)_6Mo_7O_{24}{\cdot}4H_2O$. The sample was calcined for 3 hr at 773 K under O_2.

4.2.2. X-ray photoelectron spectroscopic(XPS) measurement

The XPS spectrometer(Rigaku XPS-7000) was equipped with a magnesium anode(Mg Kα = 1253.6 eV) operated at 10 kV and 30 mA. The C1s, O1s Mo 3d and Mo 3p peaks were recorded. Charging effects were corrected by refering the binding energies to that of the adventitious C1s line at 284.8 eV.

4.2.3. PTRF-EXAFS measurements

PTRF-XAFS spectra were measured at BL14A vertical wiggler line of the Photon Factory in the National Laboratory for High Energy Physics(KEK-PF) using a Si (311) double-crystal monochromator. The storage ring was operated at 2.5 GeV with 350 ~ 200 mA. The Mo K-edge EXAFS spectra were taken from 19780 to 20500 eV with the energy interval of 3 eV at room temperature. A typical critical angle in the hard X-ray region is several miliradians. While Cu K-edge(8.9 keV) has a 4.7 mrad

of critical angle(δc), for Mo K-edge at 20 keV it is as extremely small as 1.7 mrad. In order to adjust the angle of incidence θ around δc, a 4-axis high-precision goniometer was used with a minimum step of 0.17 mrad[21]. Both fluorescent X-ray and the reflected X-ray beam intensities were monitored to determine a proper θ value. In order to prevent unnecessary irradiation, the beam size was adjusted to ϕ 0.1 mm . The incident X-ray was monitored by a 5 cm-long ion chamber filled with Ar. To detect the fluorescence X-ray coming from the sample I employed a pencil-type small NaI(Tl) scintillation counter(ϕ14 mm) in order to avoid the Bragg diffraction from the substrate effectively[22]. Since the substrate has an anisotropic surface structure, PTRF-XAFS measurements were carried out where the electric vector is parallel to $[1\bar{1}0]$, [001] and [110] directions of TiO_2(110) as shown in Fig.1(b).

4.2.4. Data analysis

PTRF-EXAFS spectra were calculated directly from the ratio of the fluorescence from the sample to the incident X-ray signal detected by an scintillation counter and ionization chamber (I_f / I_0) without any correction for self absorption. The EXAFS oscillation, $\chi(k)$, was extracted from the spectra by a spline smoothing method and normalized by the edge height using an EXAFS analysis program REX[23]. The energy dependence of the edge height was taken into account using the McMaster equation. The origin of kinetic energy of photoelectron was temporarily taken in an inflection point of the edge jump. Analysis for the surface structure of Mo oxides on TiO_2(110) was carried out using theoretical amplitude and phase shift functions calculated by FEFF 6.01[24-26].

FEFF 6.01 simulations were carried out with the following flags enabled. Core hole 1 = K edge for Mo; S_0^2(amplitude reduction factor) = 0.90; Rmax = 0.5 nm; NLEG = 5 (up to five scattering paths with total distances less than 0.5 nm were evaluated). Debye-Waller factors were set to 0.0036 for the simulations. Unique

potentials were assigned to Mo, O and Ti atoms. Twenty-nine atoms were included in the simulation of each model structure. Polarization dependence was also considered in the simulation because PTRF-XAFS measurements were obtained from 3 different directions [1 $\bar{1}$ 0] , [001] and [110] axis of TiO_2(110). Debye-Waller factors and interatomic distances were optimized. The residual factor ε^2 was calculated according to the following equation (2),

$$\varepsilon^2 = \sum((\chi_{obs}(k_j) - \chi_{cal}(k_j))/error(k_j))^2 \qquad (2),$$

where only static errors were taken into account. The evaluation of ε^2 was carried out in the range of 40-75 nm^{-1}. Models satisfying ε^2 less than 1 for all three directions simultaneously were adopted as a plausible one.

4.3 Results and Discussion

4.3.1. XPS measurement

Photoelectron spectra of the Mo 3d5/2 and Mo 3d3/2 levels for Mo/TiO_2(110) were measured. To gain an insight into the relative abundance of the Mo species at the surface, the Mo 3d/Ti 2p intensity ratio was measured. As a result, the Mo species existed as 0.2 ML(1 Mo atom / nm^2) on TiO_2(110). The spectrum for Mo/TiO_2(110) in the Mo 3d region showed the presence of two well-resolved peaks at 232.4 and 235.6 eV. These were assigned to the Mo 3d5/2 and Mo3d3/2 spin-orbit components, respectively. The Mo oxidation number can also be assumed as 6 by the binding energies[27, 28].

4.3.2. Structure of Mo species on TiO_2(110)

PTRF-XAFS spectra where the electric vectors are parallel to the [110], [001] and [1 $\bar{1}$ 0] direction of TiO_2(110) are shown in Fig. 2. Different oscillations for each

direction should be assumed that the surface atoms of the support influenced the formation of anisotropic or asymmetric Mo structure. Especially, the short-period oscillation was observed in the EXAFS spectrum for the [1 $\bar{1}$ 0] direction. It can suggest that a certain heavier atom bonding is involved in the [1 $\bar{1}$ 0] direction in the surface structure. In order to analyze the structure, thus, I calculated several plausible models based on various literatures with FEFF 6.01. Delmon. et al have suggested that molybdena-anatase titania interaction leads to an epitaxial growth of MoO_3 crystals over the TiO_2[15]. Volta et. al reported that the rate of the MoO_3 crystal growth is strongly anisotropic[29]. Also, the coordination of symmetry around Mo atoms that form active sites is influenced by the support, and a recent X-ray absorption fine structure(XAFS) study[30] concludes that while the predominant structure of molybdates on Al_2O_3 support changes from tetrahedral to octahedral with increasing Mo loading. MoO_3-like structure is formed on SiO_2 support, and dispersed Mo atoms in octahedral coordination are favored over TiO_2. Ng and Gulari et. al, who used laser Raman and IR spectroscopies, reported that a high dispersion of octahedral polymolybdates over titania surface[31]. In order to reveal the surface structure of Mo oxides on TiO_2(110), potential models were filtered through following prior conditions based on the experimental results. First, the symmetric structure such as tetrahedral one was extracted. For symmetric structure, the PTRF-EXAFS provides the same oscillations in all directions[32]. Second, the short-period oscillation which is usually contributed by the heavier atoms, possibly Mo, was observed in the PTRF-EXAFS spectra when the polarized X-ray vector was parallel to direction of [1 $\bar{1}$ 0]. FEFF simulations were begun with (100), (010), (001) faces of MoO_3 as potential surface structures. They, though many literatures suggested (100) and (010) faces of MoO_3 on TiO_2 support, did not reproduce the observed EXAFS oscillations as shown in Fig. 3-5. As for polymolybdates such as $Mo_2O_7^{2-}$ and $Mo_7O_{24}^{6-}$, the simulations did not show suitable results(Fig. 6-7).

On the other hand, many authors have reported various structures which are

proposed to generate specific surface molybdenum oxide species, isolated mono-oxo MoO_6 species[33, 34] or dimeric molybdenum oxide structure[35, 36]. Thus, those potential models were also considered. Monomers did not reproduce the experimental oscillations as shown in Fig. 8. Two dimer structures based on MoO_3 bulk crystal, edge shared and corner shared models as shown in Fig. 9-10, were simulated. While the corner shared Mo dimer model was not satisfied, it was the firstly obtained ε^2 value less than 1 for $[1\,\bar{1}\,0]$ and [001] directions when the edge-shared dimer model was suggested as shown in Fig. 10. As a result, the short-period oscillation for the $[1\,\bar{1}\,0]$ direction of TiO_2(110) was nearly reproduced by the Mo-Mo bond at 0.335 nm. It is proposed that the Mo dimer species has a 0.335 nm Mo-Mo bond which is parallel to the $[1\,\bar{1}\,0]$ direction of TiO_2(110) as shown in Fig. 11. However, it was claimed that the proposed model was not reproduced well for the [110] direction EXAFS oscillation which should include the metal-oxide support interaction because I did not consider the influence of the substrate. In order to obtain a precise structural information, I included the surface atoms such as Ti and O for the simulation. Since the location of the Ti atoms was important for the reproduction of EXAFS oscillation in the [110] direction, I assumed two possible locations of the Mo dimer on the TiO_2 substrate as shown in Fig. 12. One is the groove sites(Fig. 12 (a)). The other is the bridging oxygen ridge sites(Fig. 12(b)). The former model produced ε^2 higher than 1 for the [110] direction(Fig. 13(a)). On the other hand, the latter produced ε^2 less than 1 for the direction as shown in Fig 13 (b). Thus, I adopted the latter model in which the distance between Mo and the surface was 0.220 nm. It was obtained ε^2 value less than 1 for all directions and well reproduced the observed EXAFS oscillation as shown in Fig.14. In the proposed model structure as presented in Fig.15, the determined Mo-Ti distance was 0.296 nm which is well corresponding to the previously observed Mo-Ti distance by conventional EXAFS of Mo /TiO_2(powder sample) [37]. On the other hand, it was also observed that the two protruding oxygen atoms shared by two Mo atoms in the latter model structure are distorted from their original position. The

observed EXAFS oscillation for [110] direction was not reproduced if it was calculated with the model that the two oxygens are present on their original positions. Thus, it was suggested that the oxygen atoms in the protruding oxygen ridge are distorted from their original positions as the result of the strong interaction with Mo atoms.

The Mo dimer structure is unique in several points. First, the structure on the TiO_2(110) surface is Mo dimer interacting with the support; they are neither monomer nor origomer. It was found that Mo monomer was formed on TiO_2(110) if a trace amount of Na or K existed on the surface[32]. About the formation of the dimer species, there are various studies related with W, Cu, Mo, etc. Burrow et. al suggested that WO_4 dimers species are formed on titania by High resolution electron microscopy (HREM)[38]. It was also reported that Cu dimer species are grown on α-Al_2O_3 (0001) which was realized by means of surface sensitive X ray absorption spectroscopy (SEXAFS) at the Cu K-edge[39]. Iwasawa et. al also indicated that Mo dimer species formed on SiO_2 work as active sites for ethanol oxidation by EXAFS[40]. Second, the direction of the Mo-Mo is perpendicular to the protruding oxygen ridge along the [001] axis of TiO_2(110). Onishi et. al suggested that Ni atoms are grown along the oxygen row by the interaction between the metal particles and the substrate[41]. There are other examples about the growth depending on the direction of substrates. Al, In, and Ga atoms form dimers that bond to Si(100), forming dimers rows parallel to the underlying Si dimer rows based on calculations of the interaction energy[42-44]. Finally, the Mo dimer steps over the protruding oxygen ridge. It was also found that the two bridging oxygens shared by two Mo atoms were deviated from their original position for bridging atoms, shown in Fig.15. The formation of the Mo dimer structure on the TiO_2 surface can be explained as follows (Fig.16). As the result of the strong interaction with the protruding oxygen ridge which has more ionic property than the in-plane oxygen, the molybdenum was preferentially deposited on site A of TiO_2(110) as shown in Fig.16. Since the oxygen atoms around the Mo were distorted by the interaction, the protruding oxygen ridge should be unstable. If two Mo atoms happen

to be located on the neighboring positions in the two adjacent grooves, they share two distorted oxygens in an protruding oxygen ridge instead of 4 distorted oxygens before Mo dimer formation. Thus, the distortion energy will be released by the Mo dimer formation. If the Mo dimer was formed along the oxygen row, the Mo-Mo bond distance should be 0.296 nm considering from the lattice oxygen distance. Since the value is considerably smaller than one in usual Mo oxide structures, the growth of Mo dimer in this direction should be less stable. When Mo atoms adsorbed on the TiO_2 surface, the bridging oxygens contacting the Mo atoms were distorted. The distortion energy was expressed by E_{dis} per Mo atom. When two Mo atoms were paired by sharing the two bridging oxygens, the distortion energy(Ef_{dis}) would be less than $2E_{dis}$ because the bridging oxygens had already been distorted. Therefore the pair formation of two Mo atoms would stabilize the system by $Ef_{dis}-2E_{dis}<0$.

4.4 Conclusion

I carried out Mo K-edge PTRF-EXAFS measurements for Mo oxides on $TiO_2(110)$ in the 3 different directions of the substrate, which indicated the formation of Mo dimer structure which stepped over the bridging oxygen row with its Mo-Mo distance at 0.335 nm along the $[1\,\bar{1}\,0]$ direction of $TiO_2(110)$. It was also found that the Mo dimer species existed at 0.220 nm far from the surface.

References

[1] B. K. Teo, *EXAFS Spectroscopy: Basic Principles and Data Analysis* (Springer-Verlag, Berlin, 1986).

[2] D. C. Koningsberger and R. Prins, *X-ray absorption, Principles, applications, techniques of EXAFS, SEXAFS, and XANES* (John Wiley & Sons, New York, 1988).

[3] Y. Iwasawa, in *World Scientific Series on Synchrotron Radiation Techniques and Applications*, edited by D. H. Bilderback, K. O. Hodgeson, M. P. Kiskinova and R. Rosei (World Scientific, Singapore, 1996), Vol. 2, p. 410.

[4] H. Oyanagi, R. Shioda, Y. Kuwahra, and K. Haga, *J. Synchrotorn Rad.* **2**, 99 (1995).

[5] J. Jaklevic, J. A. Kirby, M. P. Klein, A. S. Robertson, G. S. Brown, and P. Eisenberger, *Solid State Communications* **23**, 679 (1977).

[6] J. Stohr, in *X-ray absorption Principles, Applications, Techniques of EXAFS, SEXAFS, and XANES.*, edited by R. P. D.C.Koningsberger (A John Wiley & SONS, New York, 1988), Vol. 92, p. 443.

[7] T. Ohta, K. Asakura, and T. Yokoyama, *Application to Surface Structure Analyses* (Elsevier, Amsterdam, 1996).

[8] S. M. Heald, E. Keller, and E. A. Stern, *Phys. Lett.* **A 103**, 155 (1984).

[9] M. Shirai, T. Inoue, H. Onishi, K. Asakura, and Y. Iwasawa, *J.Catal.* **145**, 159 (1994).

[10] M. Shirai, K. Asakura, and Y. Iwasawa, *Chem. Lett.* 1037 (1992).

[11] C. R. Adams and T. S. Jennings, *J. Catal.* **2**, 63 (1963).

[12] J. D. Krenze and G. W. Keulks, *J. Catal.* **61**, 316 (1980).

[13] J. D. Burrington, C. T. Kartisch, and R. K. Graseli, *J. Catal.* **81**, 489 (1983).

[14] J. G. Eon, E. Bordes, A. Vejux, and P. Courtine, in *Proceedings-9th Symposium on the Reactivity of Solids*, edited by K. Dyrek, J. Harber and J. Nowontny, Warnzac, 1982) p603.

[15] T. Machej, B. Doumain, B. Yasse, and B. Delmon, *J. Chem. Soc. Faraday Trans. I* **84**, 3905 (1988).

[16] V. E. Henrich and P. A. Cox, *The Surface Science of Metal Oxides* (Cambridge University Press, Cambridge, Great Britain, 1994).

[17] B. L. Maschoff, J. Pan, and T. E. Madey, *Surf. Sci.* **259**, 190 (1991).

[18] H. Onishi and Y. Iwasawa, *Chem. Phys. Lett.* **226**, 111 (1994).

[19] G. Charlton, P. B. Hows, C. L. Nicklin, P. Steadman, J. S. G. Tayor, C. A. Muryn, S. P. Harte, J. Mereer, R. McGrath, D. Norman, T. S. Turner, and G. Turner, *Phys. Rev. Lett.* **78**, 495 (1997).

[20] M. Ramamoorthy, D. Vanderbilt, and R. D. King-Smith, *Phys.Rev.B* **49**, 16721 (1994).

[21] Y. Satow and Y. Iitaka, *Rev. Sci. Instrum.* **60**, 2390 (1989).

[22] W.-J. Chun, K. Asakura, and Y. Iwasawa, *J. Synchrotron Rad.* **3**, 160 (1996).

[23] EXAFS analysis program package"REX ver. 2.04" (Rigaku Industrial Corporation, 1993).

[24] J. J. Rehr, J. M. de Leon, Zabinsky, S. I. , and R. C. Albers, *J. Am. Chem. Soc.* **113**, 5135 (1991).

[25] J. J. Rehr, *Jpn. J. Appl. Phys.* **32**, 8 (1993).

[26] J. J. Rehr, C. H. Booth, F. Bridges, and S. I. Zabinsky, *Phys. Rev. B* **49**, 12347 (1994).

[27] R. B. Quincy, M. Houalla, A. Proctor, and D. M. Hercules, *J. Phys. Chem.* **94**, 1520 (1990).

[28] J.-G. Choi and L. T. Thompson, *Appl. Surf. Sci.* **93**, 143 (1996).

[29] J. C. Volta and J. L. Portefaix, *Appl. Catal.* **18**, 32 (1985).

[30] H. Shimada, N. Matsubayashi, T. Sato, T. Yoshimura, and A. Nishijima, *J. Catal.* **138**, 746 (1992).

[31] K. Y. S. Ng and E. Gulari, *J. Catal.* **92**, 340 (1985).

[32] W.-J. Chun, M. Shirai, K. Tomishige, K. Asakura, and Y. Iwasawa, *J. Molecular*

Catal. A: Chemical **107**, 55 (1996).

[33] C. C. Williams, J. G. Ekerdt, J.-M. Jehng, F. D. Hardcastle, A. M. Turek, and I. E. Wachs, *J. Phys. chem.* **95**, 8781 (1991).

[34] F. H. Jones, R. Dixon, J. S. Foord, R. G. Egdell, and J. B. Pethica, *Surf. Sci.* **376**, 367 (1997).

[35] Y. Iwasawa, K. Asakura, H. Ishii, and H. Kuroda, *Dynamic Behaviour of Active Sites of a SiO_2-Attached Mo(VI)-Dimer Catalyst durign Ethanol Oxidation Observed by Means of EXAFS* (R. Oldenbourg Velag, Munchen, 1985).

[36] A. N. Desikan, W. Zhang, and S. T. Oyama, *J. Catal.* **157**, 740 (1995).

[37] H. Shimada, N. Matsubayashi, T. Sato, Y. Yoshimura, A. Nishijima, N. Kosugi, and H. Kuroda, *J. Catal.* **138**, 746 (1992).

[38] A. Burrows, C. Kiely, R. W. Joyner, H. K. Knozinger, and F. Lange, *Catal. Lett.* **39**, 219 (1996).

[39] S. Gota, M. Gautiersoyer, L. Douillard, J. P. Duraud, and P. Lefevre, *Surf. Sci.. May* **352**, 1016 (1996).

[40] Y. Iwasawa, *Catal.Today* **6**, 27 (1989).

[41] H. Onishi, T. Aruga, C. Egawa, and Y. Iwasawa, *Surf.Sci.* **233**, 261 (1990).

[42] A. A. Baski, J. Nogami, and C. F. Quate, *J. Vac. Sci. Technol.* **A 8**, 245 (1990).

[43] J. E. Northrup, M. C. Schabel, C. J. Karlsson, and R. I. G. Uhrberg, *Phys. Rev. B* **44**, 13799 (1991).

[44] G. Brocks, P. J. Kelly, and R. Car, *Phy. Rev. Lett.* **70**, 2786 (1993).

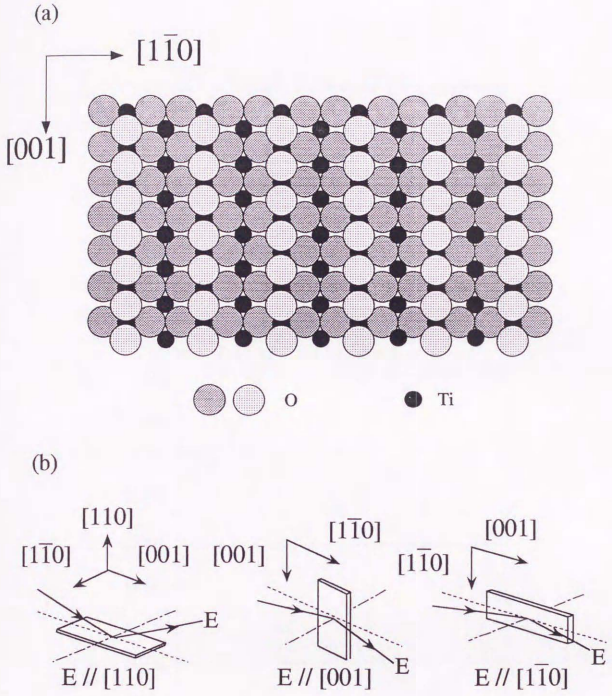

Fig. 1 PTRF-EXAFS measurement scheme: (a) TiO_2(110) surface structure; (b) Schematic diagram for PTRF-EXAFS measurement. *E: electric vector.

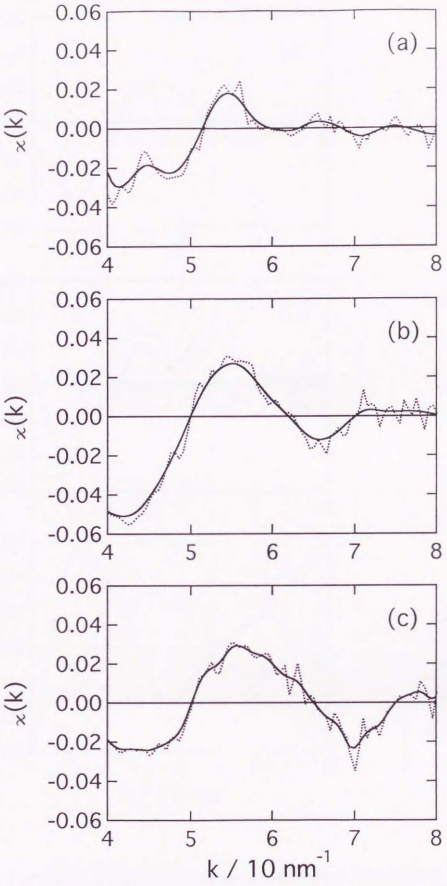

Fig. 2 k^0-weighted, background-subtracted raw Mo K-edge PTRF-EXAFS oscillation for Mo oxides on $TiO_2(110)$: (a) *E // [1 $\bar{1}$ 0]; (b) E // [001]; (c) E // [110]. Broken line: observed; solid line: smoothing treated. *E: electric vector.

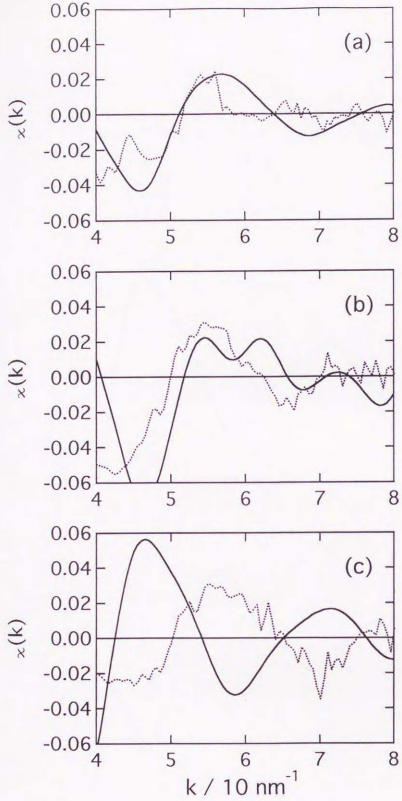

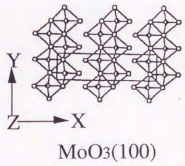

Fig. 3 k^0-weighted, background-subtracted raw Mo K-edge PTRF-EXAFS oscillation for Mo oxides on TiO_2(110) compared to FEFF simulation with MoO_3 (100) surface; (a) *E // [1 $\bar{1}$0] with the model calculated on (100) polarization; (b) E // [001] with the model calculated on (010) polarization; (c) E // [110] with the model calculated on (001) polarization. Broken line: observed; solid line: calculated. *E: electric vector.

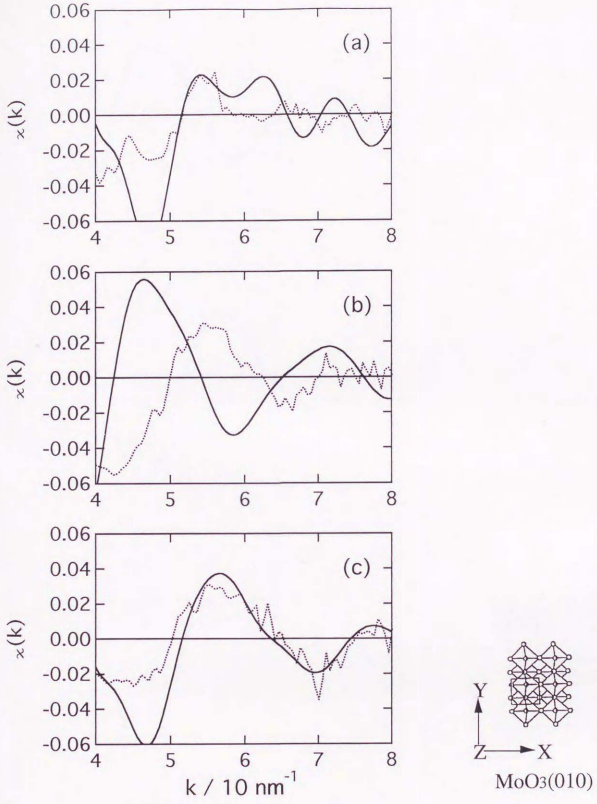

Fig. 4 k^0-weighted, background-subtracted raw Mo K-edge PTRF-EXAFS oscillation for Mo oxides on TiO_2(110) compared to FEFF simulation with MoO_3 (010) surface; (a) *E // [1 $\bar{1}$ 0] with the model calculated on (100) polarization; (b) E // [001] with the model calculated on (010) polarization; (c) E // [110] with the model calculated on (001) polarization. Broken line: observed; solid line: calculated. *E: electric vector.

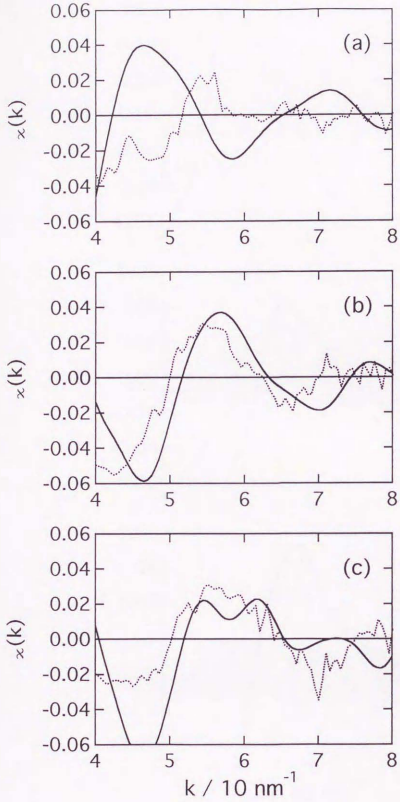

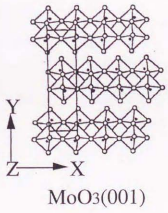

Fig. 5 k^0-weighted, background-subtracted raw Mo K-edge PTRF-EXAFS oscillation for Mo oxides on TiO_2(110) compared to FEFF simulation with MoO_3 (001) surface; (a) *E // [1 $\bar{1}$0] with the model calculated on (100) polarization; (b) E // [001] with the model calculated on (010) polarization; (c) E // [110] with the model calculated on (001) polarization. Broken line: observed; solid line: calculated. *E: electric vector.

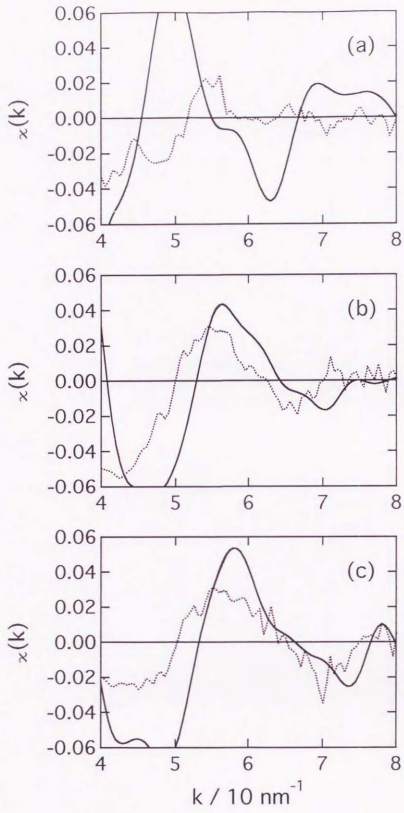

Fig. 6 k^0-weighted, background-subtracted raw Mo K-edge PTRF-EXAFS oscillation for Mo oxides on TiO_2(110) compared to FEFF simulation with $Mo_2O_7^{2-}$ structure; (a) *E // [1 $\bar{1}$0] with the model calculated on (100) polarization; (b) E // [001] with the model calculated on (010) polarization; (c) E // [110] with the model calculated on (001) polarization. Broken line: observed; solid line: calculated. *E: electric vector.

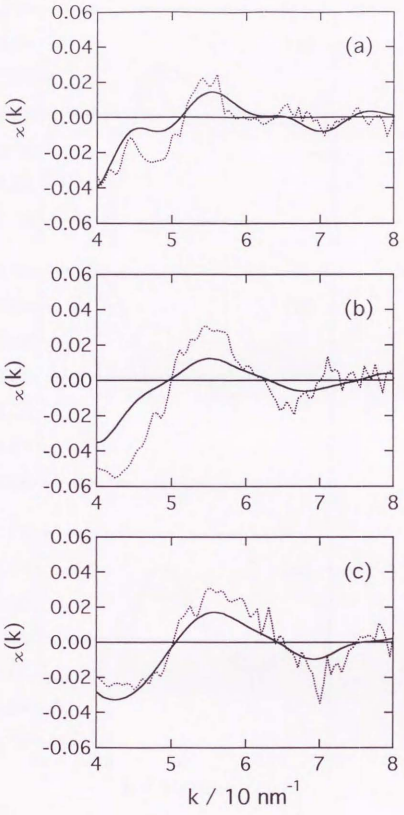

Fig. 7 k^0-weighted, background-subtracted raw Mo K-edge PTRF-EXAFS oscillation for Mo oxides on TiO_2(110) compared to FEFF simulation with $Mo_7O_{24}^{6-}$ structure; (a) *E // [1 $\bar{1}$0] with the model calculated on (100) polarization; (b) E // [001] with the model calculated on (010) polarization; (c) E // [110] with the model calculated on (001) polarization. Broken line: observed; solid line: calculated. *E: electric vector.

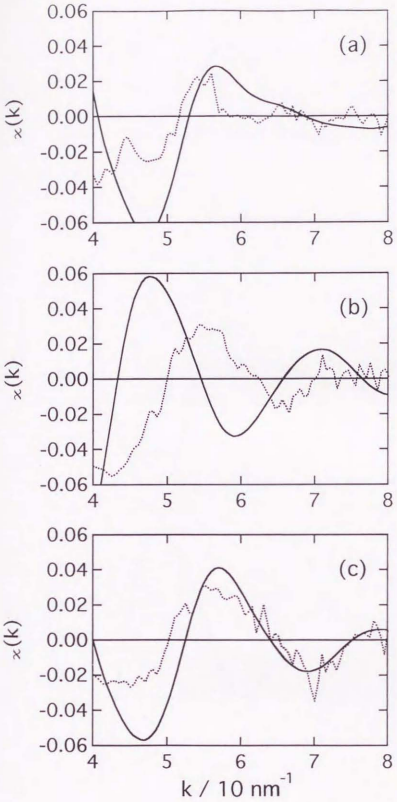

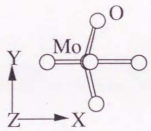

Monomer model

Fig. 8 k^0-weighted, background-subtracted raw Mo K-edge PTRF-EXAFS oscillation for Mo oxides on TiO_2(110) compared to FEFF simulation with the monomer structure; (a) *E // [1 $\bar{1}$ 0] with the model calculated on (100) polarization; (b) E // [001] with the model calculated on (010) polarization; (c) E // [110] with the model calculated on (001) polarization. Broken line: observed; solid line: calculated. *E: electric vector.

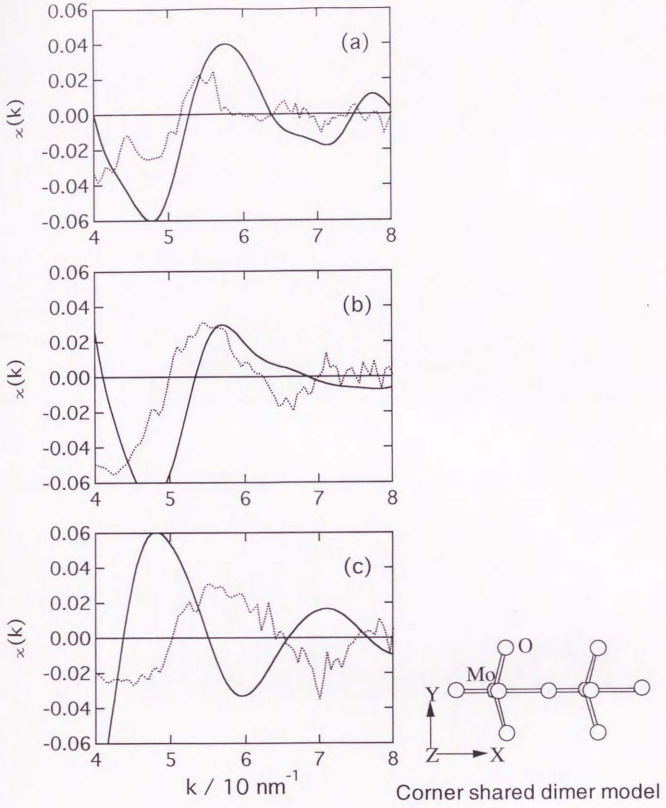

Fig. 9 k^0-weighted, background-subtracted raw Mo K-edge PTRF-EXAFS oscillation for Mo oxides on TiO_2(110) compared to FEFF simulation with the corner-shared dimer structure; (a) *E // [1 $\bar{1}$0] with the model calculated on (100) polarization; (b) E // [001] with the model calculated on (010) polarization; (c) E // [110] with the model calculated on (001) polarization. Broken line: observed; solid line: calculated. *E: electric vector.

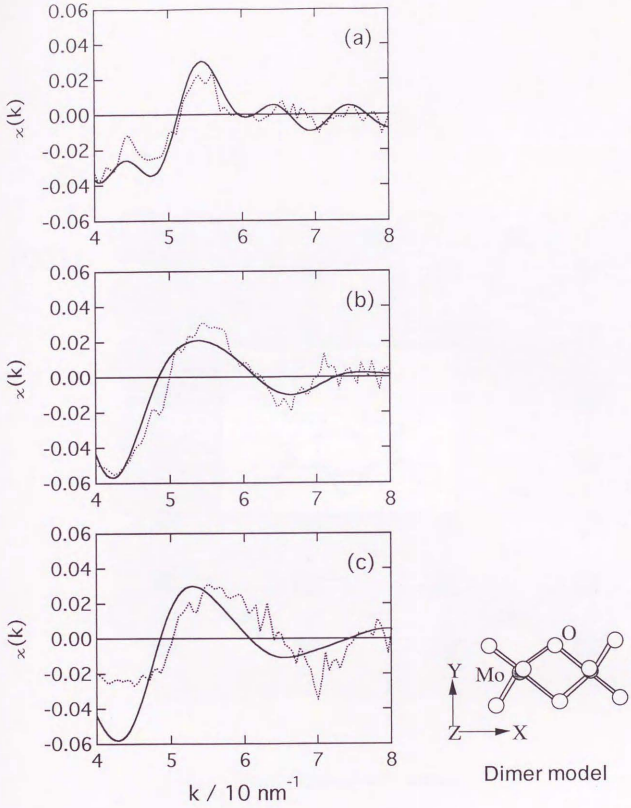

Fig. 10 k^0-weighted, background-subtracted raw Mo K-edge PTRF-EXAFS oscillation for Mo oxides on TiO_2(110) compared to FEFF simulation with the edge-shared dimer structure; (a) *E // [1 $\bar{1}$ 0] with the model calculated on (100) polarization; (b) E // [001] with the model calculated on (010) polarization; (c) E // [110] with the model calculated on (001) polarization. Broken line: observed; solid line: calculated. *E: electric vector.

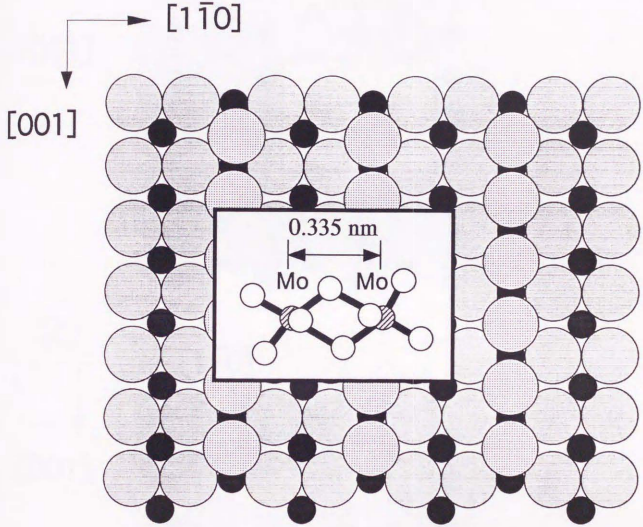

Fig. 11 Proposed model structure.

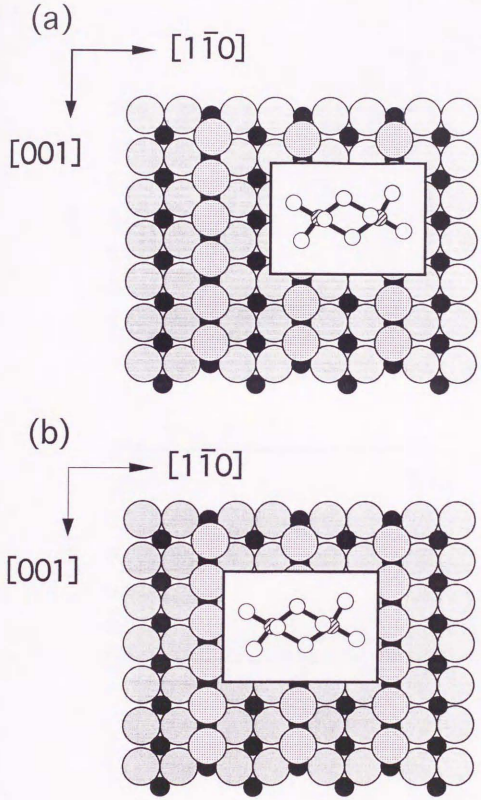

Fig. 12 Proposed model of potential locations of the Mo dimer on TiO_2(110): (a) Mo dimer on the groove of TiO_2(110); (b) Mo dimer step over the bridging oxygen ridge.

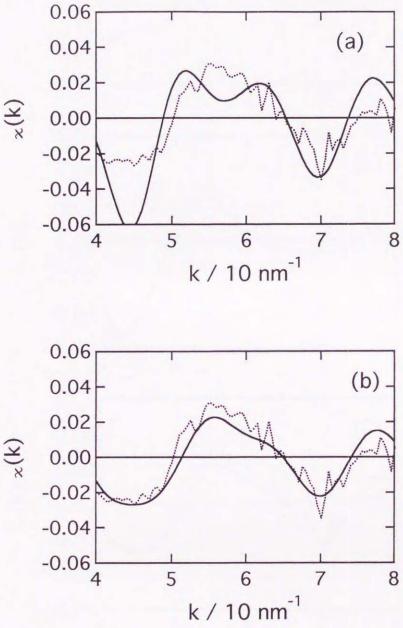

Fig. 13 k^0-weighted, background-subtracted raw Mo K-edge PTRF-EXAFS oscillation for Mo oxides on TiO_2(110) compared to FEFF simulation for determining plausible location of Mo dimer species on the substrate; (a) *E // [110] with the Mo dimer on the groove of TiO_2(110) on (001) polarization; (b) E // [110] with the Mo dimer step over the bridging oxygen ridge on (001) polarization. Broken line: observed; solid line: calculated. *E: electric vector.

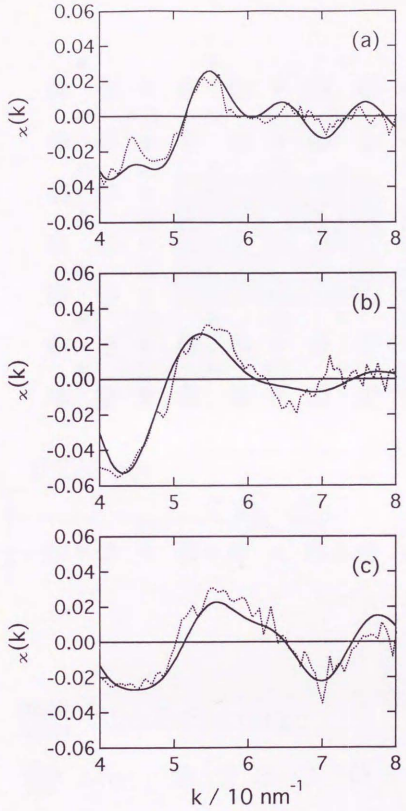

Fig. 14. k^0-weighted, background-subtracted raw Mo K-edge PTRF-EXAFS oscillation for Mo oxides on TiO_2(110) compared to FEFF simulation with the Mo dimer structure; (a) *E // [1 $\bar{1}$0] with the model calculated on (100) polarization; (b) E // [001] with the model calculated on (010) polarization; (c) E // [110] with the model calculated on (001) polarization. Broken line: observed; solid line: calculated. *E: electric vector.

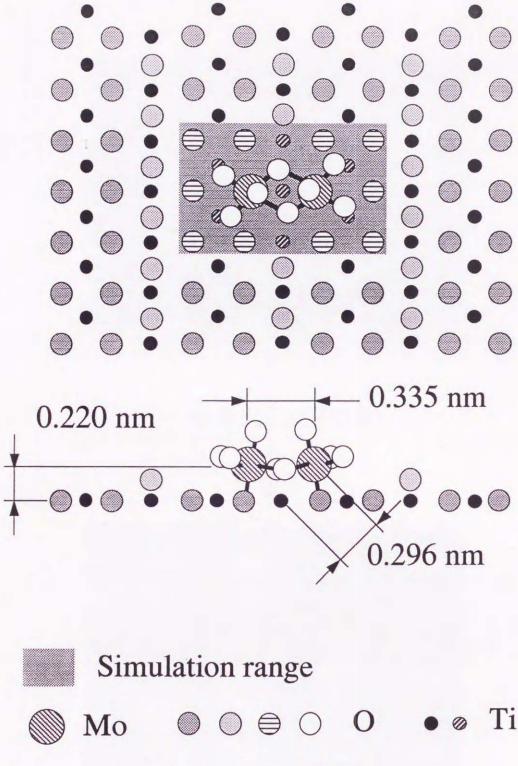

Fig. 15 Proposed optimized model.

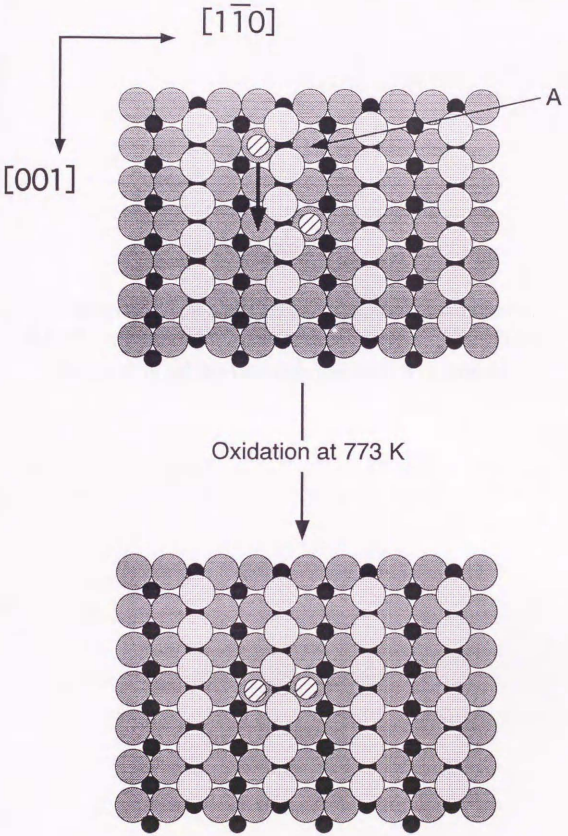

Fig. 16 Schematic diagram for the formation of Mo dimer species on TiO_2(110).

Chapter 5

Polarization-Dependent Total Reflection Fluorescence XAFS studies for Structure of Mo oxides on TiO_2(110) Single Crystal Surface Induced by Alkali Metals

ABSTRACT

In this chapter, the polarization-dependent total-reflection fluorescence EXAFS(PTRF-EXAFS) was applied to investigate the change of Mo oxides structure on TiO_2(110) surface that induced by alkali metals. PTRF-EXAFS measurements revealed that the Mo oxide species on TiO_2(110) has a symmetric tetrahedral Mo oxide structure with Mo-O at 0.176 nm by interaction between molybdenum and alkali metals.

5.1 Introduction

Dispersion and growth mode of the catalytically active metal sites in supported metal catalysts are effected by many factors such as chemical states of the metal, morphology of the supports, and the interaction between metal and support. In the view of design of active sites in catalysis, it is very interesting to manipulate the surface structure by employing alkali metals and thus has been investigated[1, 2]. Alkali additives play an important role in adsorption and catalysis and also have been an intense subject in connection with catalytic promotion and adsorbate-adsorbate interaction[3-6]. Polarization-dependent total-reflection fluorescence EXAFS(PTRF-EXAFS) already presented the possibility of the EXAFS measurements for higher atomic-number elements over 42 in the previous Chapter 4 and was suggested as a powerful method to investigate the surface structure by Shirai et. al.[7, 8]. In this chapter, it was carried out to investigate the change of surface structure of Mo oxides on TiO_2(110) doped with K by means of polarization-dependent total-reflection fluorescence EXAFS(PTRF-EXAFS).

5.2 Experimental

A rutile $TiO_2(110)$ single crystal was annealed for 2 h at 823 K in air. Mo was deposited on the $TiO_2(110)$ surface using an aqueous solution of $(NH_4)_6Mo_7O_{24}$•$4H_2O$ with a distilled water containing a trace of alkali metals and oxidized for 3 h at 773 K under O_2. The loading of the sample was 0.4 ML determined by XPS measurement. PTRF-EXAFS measurements for 3 different directions, i.e. [1 $\bar{1}$ 0], [001], and [110] directions of the substrate, were carried out at BL14A of the Photon Factory in the National Laboratory for High Energy Physics(KEK-PF) as in the previous Chapter 4. The EXAFS oscillation, $\chi(k)$, was extracted from the spectra by a spline smoothing method and normalized by the edge height. The spectra of Mo oxides on $TiO_2(110)$ were also analyzed with feff 6.01. In order to investigate the amount of alkali metals on $TiO_2(110)$, a Total Reflection Fluorescence X-ray Analysis was employed. The measurement was equipped with a W anode operated at 30 kV and 200 mA under ψ is 0.020 ° (Technos I. T. Co., Japan TREX610T).

5.3 Results and Discussion

Mo K-edge PTRF-EXAFS spectra of the Mo oxides on $TiO_2(110)$ in 3 different directions, i.e. [1 $\bar{1}$ 0], [001], and [110] directions, are shown in Fig.1. It is found that the PTRF-EXAFS spectra have similar oscillations in every different direction. It is different results comparing with Mo K-edge PTRF-EXAFS spectra in Chapter 4. In the previous chapter, the PTRF-EXAFS spectra for the sample prepared by an ultra-pure aqueous solution of $(NH_4)_6Mo_7O_{24}$•$4H_2O$ showed different oscillations for each direction (Fig.2) and considered the formation of the anisotropic surface structure. Thus, it is indicated that a symmetric surface structure was formed on the sample prepared with a distilled water solution. Comparing Fig.1 with 2, remarkable changes are found. First, the characteristic oscillation of Fig.2(a) related with the Mo-Mo bond drastically

disappeared and changed to the oscillation due to Mo-O bond in Fig.1(a). Second, the EXAFS oscillation in the [110] direction as presented in Fig.2 (c) which is most influenced by the interaction between Mo and substrate surface is also changed. Third, the EXAFS spectra in Fig.1 have almost same period oscillation. From these results it can be expected that the coordination numbers and bond distances for the three directions are similar. In order to determine the structure formed on TiO_2(110), the simulation was performed using the theoretical amplitude and phase shift functions calculated from Feff 6.01. On the other hand, a total reflection fluorescence x-ray analysis revealed that K of almost equal amounts to Mo existed on TiO_2(110)(Table 1). O'Young and Kantschewa et. al described that the employment of alkali metals as promoters in an alumina-supported molybdenum oxide catalyst changes Mo oxide structure from octahedral to tetrahedral induced by the presence of these dopants[9, 10]. And it is also suggested that the formation of tetrahedral structure on the surface suppresses reducibility of molybdenum and NO uptake[10]. As a most plausible model for the simulation from these results, symmetric coordinated tetrahedral Mo oxide structure such as K_2MoO_4 was evaluated. The analysis well reproduced the observed EXAFS oscillations in all the directions as presented in Fig.3. The breakdown of the surface structure is considered by interaction between molybdenum atoms and alkali metals. The decrease in Mo-Mo coordination number is induced by doping alkali metals such as K[1, 2]. Finally, in case of titania supported catalysts(powder) doped with Na, the change only becomes to occur at Alkali/Mo atomic ratios higher than two. However, I obtained the structural change even at unity of Alkali/Mo atomic ratio[1, 9, 10]. The present analysis indicates that the PTRF-XAFS technique is a considerably powerful method to investigate the surface structure with a high sensitivity.

In conclusion, it is found that Mo oxides with Mo-O distance at 0.176 nm in a tetrahedral symmetry are stabilized on TiO_2(110) which provides no anisotropic spectra.

References

[1] C. Martin, I. Maritn, and V. Rives, *J. Catal.* **147**, 465-475 (1994).

[2] C. Martin, I. Martin, and V. Rives, *J. Chem. Soc. Faraday Tran.* **89**, 4131 (1993).

[3] H. P. Bonzel, *Surf. Sci. Rept.* **8**, 43 (1987).

[4] H. Onishi, T. Aruga, C. Egawa, and Y. Iwasawa, *Surf.Sci.* **199**, 54 (1988).

[5] H. Onishi, T. Aruga, C. Egawa, and Y. Iwasawa, *J. Chem. Soc., Faraday Trans 1* **85**, 2597 (1989).

[6] H. Onishi and Y. Iwasawa, *Catalysis Letters* **38**, 89 (1996).

[7] M. Shirai, T. Inoue, H. Onishi, K. Asakura, and Y. Iwasawa, *Journal of Catalysis* **145**, 159 (1994).

[8] M. Shirai, K. Asakura, and Y. Iwasawa, *Chem. Lett.* **15**, 247 (1992).

[9] M. Kantschewa, F. Delannay, H. Jeziorowski, E. Delgado, S. Eder, G. Ertl, and H. Knozinger, *J. Catal.* **87**, 482 (1984).

[10] C. L. O'Young, *J. Phys. Chem.* **93**, 2016 (1989).

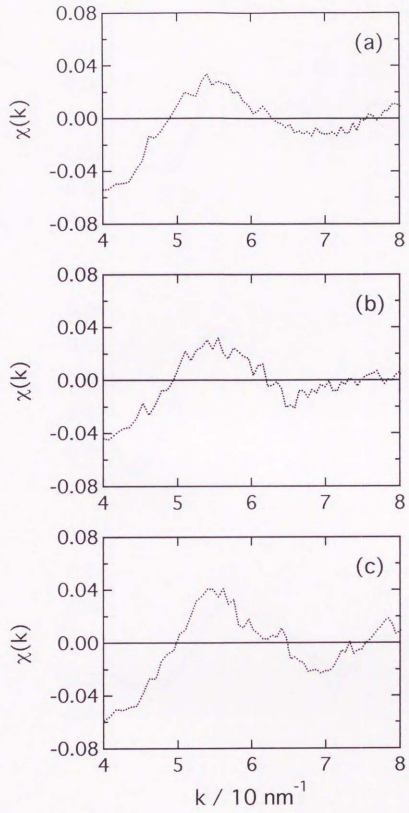

Fig. 1 k^0-weighted, background-subtracted raw Mo K-edge PTRF-EXAFS oscillation for Mo oxides on TiO_2(110) prepared with a distilled water solution: (a) *E // [1 $\bar{1}$ 0]; (b) E // [001]; (c) E // [110]. *E: electric vector.

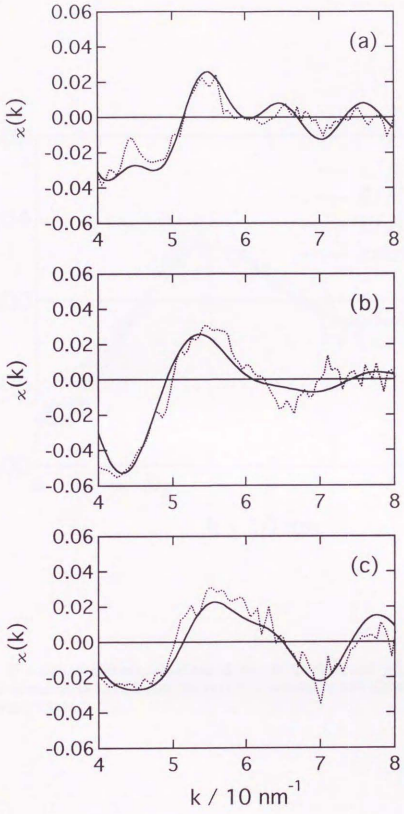

Fig. 2. k^0-weighted, background-subtracted raw Mo K-edge PTRF-EXAFS oscillation for Mo oxides on TiO_2(110) compared to FEFF simulation with the Mo dimer structure; (a) *E // [1 $\bar{1}$ 0] with the model calculated on (100) polarization; (b) E // [001] with the model calculated on (010) polarization; (c) E // [110] with the model calculated on (001) polarization. Broken line: observed; solid line: calculated. *E: electric vector.

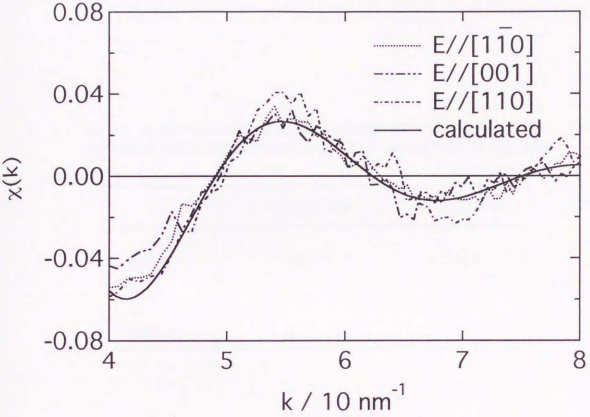

Fig.3 k^0-weighted, background-subtracted raw Mo K-edge PTRF-EXAFS oscillation for Mo oxides on TiO_2(110) compared to FEFF simulation with K_2MoO_4.
*E: electric vector.

Table 1 Results from total reflection x-ray fluorescence analysis.
Operated at 30 kV, 200 mA under 0.02 deg. of incident angle by Si(Li) SSD.

	Energy / keV	Intensity / cps
K-Kα	3.31	389.8
Ti-Kα	4.51	13936.7
Mo-Lα	2.29	391.2

Chapter 6

Surface Structure Change of a $[Pt_4(\mu\text{-}CH_3COO)_8]/SiO_2$ Catalyst Active for the Decomposition of Formic Acid

ABSTRACT

Pt_4-cluster/SiO_2 catalyst, prepared from the [$Pt_4(\mu$-$CH_3COO)_8$] cluster, has shown remarkably high catalytic activity with 100% selectivity to CO_2 and H_2 for the decomposition formic acid as compared with the Pt particle/SiO_2. In order to elucidate the genesis and the mechanism for the catalysis by Pt_4-cluster/SiO2, the samples were characterized by kinetics, Pt L_3-edge EXAFS, and FT-IR. EXAFS and IR data revealed that the surface structure of the catalyst changed from the tetramer to dimers during an induction period, then to monomers which were active for the catalysis. Eventually Pt particles were formed of much lower catalytic activity. The structural transformations of the Pt_4-cluster/SiO_2 catalyst are discussed in relation to the catalytic reaction profiles.

6.1 Introduction

Knowledge of the structure and chemical state of the active site of catalyst is indispensable to elucidate the catalytic reaction mechanism. New-catalytic materials generate unique catalysis which may provide information on the genesis and the mechanism for efficient catalysis. At the surface of an inorganic oxide such as SiO_2 and Al_2O_3, novel metallic and metal-oxide species, which cannot be obtained in homogeneous solution systems, can be produced from organometallic and metal cluster compounds as precursors, followed by chemical treatments when necessary[1-3]. The surface species obtained are often entirely different in nuclearities and structures, from those prepared by a traditional impregnation method using aqueous solution of metal salts[1-5]. One of methods supporting very small metal particles or clusters on oxide surfaces is the use of metal-cluster compounds as precursors, which are characterized by their unique frame work consisting of three or more metal atoms and stabilized by appropriate ligands such as carbonyl, phosphines, halides, acetates, oxides, etc.[1-5]. I found that the catalyst prepared by supporting [$Pt_4(\mu$-$CH_3COO)_8$] on SiO_2 showed a

remarkably high activity for formic acid decomposition compared with a Pt particle catalyst.

Decomposition of formic acid on metal and oxide surfaces has served as a convenient testing reaction for fundamental research for catalysis; e.g. to determine the factors which can affect the catalytic properties of metals and metal oxides[6-11]. It was also the first reaction which demonstrated that the catalytic performance of a metal was drastically influenced by the nature of the support[12-15]. There are also examples of the studies related with the mechanism of the catalytic decomposition of formic acid, such as water-gas shift reaction(WGSR)[16-22] and the synthesis and decomposition of methanol[23-27]. Those examples indicate that the study of HCOOH decomposition is not only of academic interest, but also of strong relevance to some important industrial catalytic processes.

In the present study $[Pt_4(\mu\text{-}CH_3COO)_8]$ (octakis(μ-acetato-O,O') tetraplatinum (II)) was employed as a precursor for SiO2-supported platinum catalyst, which is shown in Fig.1[28-30]. The cluster has a square framework composed of four Pt atoms with strong metal-metal bonds at the distances 0.2493 ~ 0.2501 nm, and is coordinated by eight bridging acetate groups. Note that the Pt-Pt distance of the Pt_4-cluster is shorter than other Pt clusters(0.258 - 0.265 nm) such as dimers[31, 32] and trimers[33, 34]. The arrangement of acetate ligands is such that four groups are approximately in the cluster plane, while four others are alternately above and below it. The molecular structure is similar to that for the tetragonal form, but shows a twisting distortion away from ideal 42m(D2d) symmetry. Yamaguchi et.al. reported facile regioselective ligand substitution for the in-plane bridging acetate in the Pt cluster[35, 36]. They observed that only in-plane acetate groups were easily replaced by carboxylic acids(RCOOH; R=CH_3, CCl_3, CF_3, C_6H_5) in solution, then the structure was changed to $[Pt_4(\mu\text{-}CH_3COO)_4(\mu\text{-}HCOO)_4]$. From those properties, it could be expected that the catalyst employing the cluster would exhibit unique catalytic properties for formic acid decomposition(R=H) because decomposition of formate intermediate in the WGRS was remarkably promoted

by co-adsorbates, showing a drastic change of the selectivity[18-22]. Thus, I studied the performance of the catalyst prepared from $[Pt_4(\mu\text{-}CH_3COO)_8]$ on silica support for decomposition of formic acid.

The aim of this study is to examine the catalytic properties of the Pt_4-cluster/SiO_2 catalyst, to reveal the structure of the active species by EXAFS and FT-IR spectroscopy, and to discuss the reaction mechanism.

6.2 Experimental

6.2.1 Preparation of Pt_4-cluster/SiO_2 catalyst

The cluster $[Pt_4(\mu\text{-}CH_3COO)_8]$ was prepared using the method of Yamaguchi et.al., and was characterized with ^1H-NMR[35, 36]. SiO_2(Fuji-Davison Silicagel #952, Surface area: 300 m^2/g), was calcined at 573 K for 1h in air, followed by evacuation. The cluster was dissolved in CH_2Cl_2, and impregnated on the pretreated SiO_2 for 1h, followed by evacuation to remove the solvents. All procedures of preparation of the catalyst except for the calcination of SiO_2 were carried out on vacuum line or under Ar atmosphere. The Pt content of the catalysts was 1.0 wt%.

6.2.2 Preparation of Pt particle/SiO_2 catalyst

A 1.0 wt% Pt/SiO_2 catalyst was prepared by an ion-exchange method. SiO_2 was stirred overnight in an excess of aqueous ammonium hydroxide. The preparation was followed by adding $Pt(NH_3)4Cl_2 \cdot H_2O$ dissolved in distilled water to the system for the ion-exchange. The solution was stirred overnight. The sample was then filtered, washed with distilled water, then dried at 343 K. The catalyst was calcined at 573 K for 1h, followed by reduction with H_2 at 473 K for 1h.

6.2.3 Decomposition of formic acid on the Pt_4-cluster/SiO_2 catalyst

The catalytic decomposition of formic acid was carried out in a closed circulating system equipped with a gas chromatograph. 5A molecular sieve and Porapak PS columns were used for the analysis of reactant and products. A quadrupole mass spectrometer(AQA-100R, ANELVA) was also employed to analyze the products. Research-grade formic acid was purified over $MgSO_4$, followed by distillation. The pressure of formic acid was maintained at 1.47 kPa during the catalytic reaction. In the study on the induction period, 0.07 kPa of the initial pressure of formic acid was introduced into the system. Isotope effects were examined with DCOOH, DCOOD, and HCOOD (purchased from Cambridge Isotope Laboratories). These were used without further purification. The composition for the isotopes are listed as follows; DCOOH(D: 89%), DCOOD(D: 89%), and HCOOD(D: 89%).

6.2.4 Characterization by ^{1}H-NMR

^{1}H-NMR spectra were recorded on a HITACHI R-24B by using $CDCl_3$ as the solvent.

6.2.5 Characterization by FT-IR Spectroscopy

IR spectra of the catalyst in the course of formic acid decomposition were recorded with a JASCO FT/IR-7000 Spectrometer using a liquid nitrogen-cooled MCT detector. The measurements were conducted at room temperature and over 100 ~200 scans at a resolution of 2 cm^{-1}. The IR cell used in this study was made from Pyrex glass and has a pair of NaCl windows, which were cooled with circulating water to avoid the damage to the windows during heat treatments of the catalyst. The cell was combined with a closed circulating system. A self-supporting disk of SiO_2 powder(50 mg) mounted in the IR cell was calcined at 573 K, similarly to the catalyst preparation.

The spectrum of the treated SiO_2 was recorded after cooling to room temperature. $[Pt_4(\mu\text{-}CH_3COO)_8]/SiO_2$, was prepared by impregnating the SiO_2 disk with a solution of $[Pt_4(\mu\text{-}CH_3COO)_8]$ in CH_2Cl_2 by using a capillary under Ar atmosphere in the IR cell. Then the remaining solvent was removed by evacuation. The IR spectrum was recorded with the fresh sample. The spectra during the formic acid decomposition reactions under various conditions were taken successively as a function of reaction time. All the spectra shown in this chapter were background subtracted.

6.2.6 Characterization by in-situ EXAFS

X-ray absorption fine structure spectra at the Pt L_3-edge were measured at a beam line BL10B of the National Laboratory for High Energy Physics(KEK-PF). The storage ring operated at an electron energy of 2.5 GeV with the beam current 250 ~ 350 mA. A Si(311) channel-cut crystal monochromator was used to produce monochromatic X-rays from the synchrotron radiation, since this monochromator produces almost no second-order harmonics. X-ray absorption data were collected in transmission mode using two ionization chambers filled with N_2(I0) and N_2 85% + Ar 15%(I) as X-ray detectors. Samples for the EXAFS measurement were prepared and treated in the same way as the samples used for the catalytic reaction in a closed-circulating system and were transferred without contacting air to glass cells equipped with Kapton windows for the EXAFS measurement. The cell for the Pt L_3-edge EXAFS measurement was 10 mm thick which allows enough edge height for total absorbance enough $\mu x = 1 \sim 2$. The sample in the sealed glass cell was kept in a container at 195 K until the measurement, which was performed at 70 K and at room temperature. Data were analyzed using the program EXAFS2[37]. The analysis was involved pre-edge extrapolation, background removal by a cubic spline method to extract EXAFS data, and Fourier transformation using a Hanning window function with one-tenth of the FT range. The typical ranges of Fourier transformation from the k space to the r space were 30 ~ 150 nm^{-1} for the Pt L_3-edge. The inverse Fourier transformation to the k space and the curve fitting were carried out to

obtain detailed structural information. Empirical parameters extracted from Pt foil and $(NH_4)_4[H_4PtMo_6O_{24}]$ for Pt-O bond were used as references to analyze Pt-Pt and Pt-O bonds, respectively[38]. The coordination number in this report was corrected for the R dependence of the EXAFS amplitude by equation[39],

$$N = N^* \exp[2(R - R_s)/\lambda]$$

where N is the corrected coordination number and N^* is the coordination number determined from the analysis. Rs is the interatomic distance found from the analysis of the sample, R is the crystallographic distance of the reference sample and λ is the mean free path(1 nm). The accuracy of the values from the analysis is reported to be better than 0.02 nm for distance and ca. 10% in coordination number[40]. The validity of the curve fitting was judged from not only $\Delta E0$ and s but also the R factor(R_f)

$$R_f = \int_{k\,min}^{k\,max} | k^3\chi^{obs}(k) - k^3\chi^{calc}(k)|^2\, dk \,/ \int_{k\,min}^{k\,max} | k^3\chi^{obt}(k)|^2\, dk$$

6.3. Results and Discussion

6.3.1 Characterization of the Pt_4-cluster/SiO_2 catalyst

In order to investigate the structure of the catalyst, I performed the EXAFS analysis which was compared with the unsupported cluster. The k^3-weighted Fourier transformation of the EXAFS data for $[Pt_4(\mu\text{-}CH_3COO)_8]$/BN and the supported cluster was achieved over the range $30 < (k/nm^{-1}) < 150$. The range of the inverse Fourier transformation was $0.14 < (R/\,nm) < 0.29$. EXAFS spectra, Fourier transformation and curve fitting for the precursor are shown in Fig.2(a). The first shell(0.14 ~ 0.20 nm) in the Fourier transformation is assigned to Pt-O bond and the second one(0.20 ~ 0.29 nm) is assigned to Pt-Pt bond. Based on the crystallographic structure of the precursor, it were performed three-wave (Pt-O+Pt-O+Pt-Pt) curve fitting as shown in Fig.2(a-3). In the present analysis the number of independent parameters ($NI=2\Delta k\Delta R/\pi+2$) is 13.5 , which would also make the three-wave analysis valid[41]. However, the curve fitting analysis was conducted by fixing the coordination

numbers(C.N.) to give the best agreement with the result of crystallographic data as shown in Table 1[28-30]. The results for the Pt4-cluster/SiO2 catalyst are presented in Fig.2(b) and Table 1. There was difference between two spectra for [$Pt_4(\mu$-$CH_3COO)_8$] and the Pt_4-cluster/SiO_2 sample. The best fit result for the catalyst in Table 1 was obtained by changing the parameters, C.N., R and σ, while ΔE_0 was fixed to the same values as those for the precursor. The structural data for the catalyst are almost the same as those for the precursor itself.

To confirm the results of the EXAFS analysis the IR spectra of both [$Pt_4(\mu$-$CH_3COO)_8$] /$CDCl_3$ and [$Pt_4(\mu$-$CH_3COO)_8$] /SiO_2 systems were measured. The peaks at 1565, 1438, 1414, 1457 and 1347 cm^{-1} for the acetate ligands of the cluster in $CDCl_3$ are straightforwardly assigned to va(OCO), vs(OCO)(out-of-plane); vs(OCO)(in-plane), $\delta a(CH_3)$, and $\delta s(CH_3)$, respectively,[42, 43] as listed in Table 2. The [$Pt_4(\mu$-$CH_3COO)_8$] /SiO_2 catalyst showed almost the same spectra at 1564, 1442, 1418, 1462 and 1350 cm^{-1} for the above assigned bands, respectively.

Accordingly, the EXAFS and IR data conclude that the framework of the cluster is maintained upon supporting on SiO2.

6.3.2 Catalytic decomposition of formic acid

The profile of the catalytic decomposition of formic acid HCOOH on the [$Pt_4(\mu$-$CH_3COO)_8$] /SiO_2 catalyst is shown in Fig.3. There was an induction period of ca. 10 min for the reaction, during which time no product was observed in the gas phase. Then the reaction of HCOOH(constant pressure of 1.47 kPa at 288 K) began and the catalytic decomposition of HCOOH was found to be remarkably promoted at ca. 18 min, then a steady -state reaction proceeded as shown in Fig.3. In the steady-state, equal amounts of CO_2 and H_2 were produced in a closed circulation system (Fig.3). The catalytic reaction rates in the steady-state[turnover frequency(TF): CO_2 molecule produced per min per Pt atom] were plotted vs. the reciprocal reaction temperature in Fig.4, which gave an

Fig.4, which gave an activation energy of 69 kJ mol^{-1}. The selectivity toward CO_2 + H_2(dehydrogenation) was 100%. On the other hand, the catalytic decomposition of formic acid on the Pt particle/SiO_2 catalyst under identical conditions was negligible(two ~ three orders of magnitude less than the activity for the Pt_4-cluster/SiO_2 catalyst). In Fig.4 the Arrhenius plots for the dehydrogenation and dehydration reactions of HCOOH are also shown over a much higher temperature range. Both combinations, CO_2 + H_2 and CO + H_2O, were produced, which is in contrasted with the case of the Pt_4-cluster/SiO_2 catalyst. The activation energies for the dehydrogenation and the dehydration were calculated to be 41 and 73 kJ mol^{-1}, respectively. The remarkably high catalytic activity of the Pt_4-cluster/SiO_2 catalyst almost ceased to exist eventually after 60 min reaction as shown in Fig.3.

The detailed profile of the decomposition reactions of HCOOH, DCOOH and DCOOD is shown in Fig.5 in order to understand the genesis of the highly active catalysis of the supported clusters and to trace the behavior and mechanism of the reaction. As a common feature with formic acid and deuterium-labeled formic acid, is that there is an induction period for the first 10 ~ 14 min, followed by a slow reaction step prior to the high-rate reaction(Fig.5). The reaction rates(TF) for HCOOH, DCOOH and DCOOD in the slow reaction step were 0.0059, 0.0025 and 0.0017 min^{-1}, respectively, showing isotope effects for both C-H and O-H bonds of formic acid molecule. Isotope effects were also observed in the high-rate reaction step as shown in Fig.6; the activation energies for the decomposition reactions of HCOOH, HCOOD, DCOOH, and DCOOD were 69, 54, 49, and 24 kJ mol^{-1}, respectively. From those results, I presume that the formic acid decomposition reaction is accompanied with an induction period, a slow reaction step, a high-rate reaction step, and a deactivation process.

6.3.3 Characterization of the surface Pt sites

6.3.3.A Preceding induction period

IR spectra were measured to investigate what kind of structural change occurred in the induction step. Since HCOOH reacted too fast to observe easily, I employed DCOOD as the reactant to follow the behavior of surface active species. Fig.7 shows the IR spectra recorded at intervals in the decomposition reaction of DCOOD at 305 K on the $[Pt_4(\mu\text{-}CH_3COO)_8]/SiO_2$ catalyst disk. The peak at 1418 cm^{-1} for the in-plane acetate ligands was replaced by the in-plane formate ligands characterized by the 1304 cm^{-1} peak, whereas the out-of-plane acetates were not replaced by formic acid as proved by no change of the peak at 1442 cm^{-1}. This preferential replacement of the in-plane acetates was also observed in a $CDCl_3$ solution of $[Pt_4(\mu\text{-}CH_3COO)_8]$ and was also confirmed by ^1H-NMR which revealed ready exchange of the in-plane acetates(2.40 ppm) with formic acid in $CDCl_3$ which was completed within 2 min at room temperature, whereas the intensity of the peak(1.98 ppm) for the out-of-plane acetates remained almost unchanged. The exchange reaction favorable at the in-plane sites agrees with the results in the literature for organic carboxylates[44]. Thus it may be concluded that the cluster $[Pt_4(\mu\text{-}CH_3COO)_8]$ on SiO_2 is converted to $[Pt_4(\mu\text{-}CH_3COO)_4(\mu\text{-}HCOO)_4]/SiO_2$ by exposing the cluster to HCOOH vapor. After the replacement of four in-plane acetates in $[Pt_4(\mu\text{-}CH_3COO)_8]/SiO_2$ by formates within 2 min, no further significant change in the IR spectrum was observed in the induction period(Fig.7(b) and (c)).

To characterize the structure of the cluster $[Pt_4(\mu\text{-}CH_3COO)_4(\mu\text{-}HCOO)_4]$ on SiO_2, it was performed the EXAFS analysis for this cluster. Figure 8 shows the EXAFS oscillation in the range $30 \leq (k/nm^{-1}) \leq 150$, its associated Fourier transformation and the curve fitting[inversed Fourier transform range, $0.14 \leq (R/nm) \leq 0.29$]. Comparing with the EXAFS spectra of the $[Pt_4(\mu\text{-}CH_3COO)_8]/SiO_2$ catalyst , there is

no sign of change of the cluster structure, except slight depression around 0.16 nm in the Fourier transformation which can be referred to the replacement of in-plane acetates by formates. The curve fitting analysis was conducted in a similar way to that for the $[Pt_4(\mu\text{-}CH_3COO)_8]/SiO_2$ catalyst. The best-fit result for $[Pt_4(\mu\text{-}CH_3COO)_4(\mu\text{-}HCOO)_4]/SiO_2$ is shown in Fig.8(C) and Table 3. There was no significant difference in the structural parameters determined by EXAFS between $[Pt_4(\mu\text{-}CH_3COO)_8]/SiO_2$ and $[Pt_4(\mu\text{-}CH_3COO)_4(\mu\text{-}HCOO)_4]/SiO_2$(Table 1 and Table 3).

Accordingly, IR and EXAFS data revealed that $[Pt_4(\mu\text{-}CH_3COO)_8]$ on SiO2 was transformed to $[Pt_4(\mu\text{-}CH_3COO)_4(\mu\text{-}HCOO)_4]$ without change of the cluster framework in the induction period.

6.3.3.B Slow reaction step

I assume this step as a transformation stage for the cluster structure because the cluster framework did not change during the preceding induction period, while in the subsequent period the decomposition of formic acid gradually proceeded. Under the catalytic reaction conditions at saturation of adsorbed formic acid, it is impossible to characterize the structure of the active sites formed at this stage, because the next step is too rapid in the presence of gas-phase formic acid. Therefore, I adopted a different reaction condition for the study of the step by introducing a low pressure of formic acid(0.07 kPa). The amount of introduced formic acid is more than the in-plane acetate sites in the catalyst employed, but there is no more in gas phase during the reaction. The reaction proceeded gradually, and stopped after 180 min and 420 min for HCOOH and DCOOH, respectively as shown in Fig.9. The total amount of CO_2 produced in the low-pressure reactions was the same with both HCOOH and DCOOH, although the reaction rates were different each other. The total amount of CO_2 was also almost the same as the expected value produced by the decomposition of the replaced in-plane formate ligands. After the decomposition reaction completed, HCOOH or DCOOD of

1.47 kPa was admitted to the system. The reaction began again, showing similar high reaction rates to those in the catalytic reaction conditions in Fig.5. Thus, the state at which the low-pressure reaction stopped may be an active intermediate species on which the high-rate reaction is induced.

To obtain information on the active intermediate platinum species, IR spectra (Fig.10) for the slow step were taken under the identical conditions to the reaction. The 1418 cm^{-1} peak for the in-plane acetates was replaced by a peak at 1302 cm^{-1} for the in-plane formate (DCOO), where the 1418 cm^{-1} peak did not completely diminish. The peak of 1302 cm^{-1} decreased gradually and disappeared completely by the decomposition reaction. The decreasing rate of the formate ligands in the IR spectra coincided well with the rate of CO_2 formation. Thus, the CO_2 formation observed in the slow reaction period is suggested to be due to the decomposition of the in-plane formate ligands in the $[Pt_4(\mu\text{-}CH_3COO)_4(\mu\text{-}HCOO)_4]$ on SiO_2. Acetate ligands were found on Pt species at the end of the slow decomposition reaction, as shown in Fig.10. The number of acetate ligands coordinated to Pt atoms was estimated to be approximately an acetate ligand per Pt atom from comparison of the intensity of the IR peaks for the surface species at the end of the slow reaction with that of the IR peaks for the incipient Pt species $[Pt_4(\mu\text{-}CH_3COO)_8]/SiO_2$.

In order to determine the structure of the Pt species formed in the slow decomposition step, an EXAFS analysis was performed for the sample at the end of the slow reaction (at 180 min in Fig.9). The Pt L3-edge EXAFS data are presented in Fig.11. The oscillation [FIg.11(a)] and Fourier transform [Fig.11(b)] are entirely different from those for $[Pt_4(\mu\text{-}CH_3COO)_8]$ itself [Fig.2(a)], $[Pt_4(\mu\text{-}CH_3COO)_8]/SiO_2$ [Fig.2(b)], and the sample during the induction period (Fig.8), which suggests a partial decomposition of the original cluster framework at this reaction stage. The best-fit for the inversely Fourier-transformed oscillation was carried out in Fig.11(c) and the determined bond distances and coordination numbers for Pt-O, Pt-O, and Pt-Pt bonds are

listed in Table 4, which indicates the existence of Pt-Pt bond and two different Pt-O bonds.

From the IR and EXAFS results, I suspect that the shorter Pt-O bonds at 0.203 nm are related to the remaining acetate ligands, where the acetate : Pt ratio is 1 suggested by the IR data is compatible with the coordination number (2.1) for the Pt-O bond only if the Pt species is a dimer. The Pt-Pt bond at 0.250 nm exhibits a coordination number of 1.2, which may confirm a dimeric structure, comparing the coordination numbers of 2.0 for the Pt_4 tetramers in Tables 1 and 3. Then, the longer Pt-O bond at 0.220 nm(C.N. = 1.5) may be assigned to the bonding of Pt atom with an oxygen atom at the SiO_2 surface. It is considered that the in-plane formate ligands were decomposed to CO_2 and H_2, accompanied by the reaction of the resultant coordinately unsaturated Pt atoms with the surface OH groups. The participation of the surface OH groups in the decomposition of the in-plane formates during the slow-reaction period at an initial pressure of formic acid at 0.07 kPa was suggested by the isotope effects observed in Fig.5. When DCOOD was used as a reactant, the surface OH groups were converted to the OD groups immediately after the introduction of DCOOD to the system as proved by IR, while the OH groups were not transformed to the OD groups by DCOOH. In both cases the same peak for the in-plane DCOO ligands was observed. Therefore, the difference of the isotope effect between DCOOH and DCOOD during the slow reaction period is referred to the contribution of the surface OH groups to the in-plane formate decomposition at least in the absence of gas phase formic acid. The ratio of CO_2 to H_2 produced by the in-plane formate decomposition in the slow process as 1 : 0.8, which is close to 1 : 1, considering the experimental error in a mass-spectrometric quantification. If the in-plane formate ligands decomposed by themselves, the ratio of CO_2 to H_2 would be 1 : 0.5 and almost no isotope effect would be observed with the OH hydrogen.

6.3.3.C Catalytic high-rate reaction

IR spectra in the catalytic high-rate reaction region exhibited no peak for acetate ligands, when only physisorbed formic acid was observed at 1689 and 1388 cm^{-1} for ν(C=O) and νs(OCO), respectively. Thus, it is likely that the dimeric Pt structure as an active intermediate species was further converted to other species which is catalytically active.

The sample for the EXAFS measurement was prepared as follows. The [$Pt_4(\mu$-$CH_3COO)_8$] /SiO_2 catalyst was exposed to a constant pressure (1.47 kPa) of formic acid, then was monitored by a mass spectrometer for CO_2 and H_2 formations. Immediately after the reaction attained the steady-state rate, the sample was cooled to a liquid nitrogen temperature during evacuation followed by transfer of the sample to an EXAFS cell which was kept in the container at 195 K until the EXAFS measurement. The Pt L_3-edge k^3-weighted EXAFS oscillation, its associated Fourier transformation and the curve fitting analysis are shown in Fig.12. Initially it was tried to fit a peak at 0.23 nm(phase shift uncorrected) in the Fourier transform by assuming it to be due to Pt-Pt bonding, but a satisfactory fit was never achieved. On the other hand, a peak at 0.17 nm was straightforwardly assigned to Pt-O bonding. Next, the curve fitting analysis over a whole range (0.11 ~ 0.27 nm) was performed by assuming the first and second peaks in the Fourier transform as Pt-O bonds. The results are shown in Fig.12(c) and in Table 5, where two different Pt-O bondings at 0.201 and 0.266 nm were discriminated, reflecting the two separated peaks in the Fourier transformation [Fig.12(b)]. From these results I can conclude that the catalytically active species is a structure of Pt monomer. I also propose a unique Pt monomeric structure which has 2 ~ 3 long Pt-O bonds at 0.266 nm besides two usual Pt-O bonds at 0.201 nm as illustrated in Scheme 1. Similar observation of long Pt-O bonds has been reported in the literature[45]. In regard to the oxidation state of Pt monomers, it is likely that the Pt atoms are dispersed in the oxidized state close to a bivalent state, judging from the peak

intensity of the white line at the Pt L_3-edge, compared to those for $[Pt_4(\mu\text{-}CH_3COO)_8]$ /BN, $[Pt_4(\mu\text{-}CH_3COO)_8]$ /SiO_2 and Pt metal.

6.3.3.D Deactivation process

After the catalytic decomposition of formic acid proceeded at the high reaction rate, eventually the catalyst was deactivated as shown in Figs.3 and 5. To examine the deactivation process the EXAFS spectra for the almost deactivated catalyst were recorded in a similar manner to the others. Comparing the EXAFS spectra of this sample with those for the Pt4-cluster and the supported Pt4-cluster catalysts in the induction period, in the slow reaction region, and in the high-rate reaction region, it is obvious that a drastic change in the Pt structure has occurred. That is, the oscillation and Fourier transform in Fig.13 are similar to those for Pt foil, which demonstrates that the Pt monomers aggregated to Pt particles under formic acid decomposition reaction conditions which are reducible atmosphere. In fact, the k-space oscillation was well reproduced by Pt-Pt bonding as shown in Fig.13(c). The bond distance and coordination number for Pt-Pt were determined to be 0.276 nm and 6.6, respectively, in Table 6. It was estimated that the Pt particles to have ca. 0.9 nm in diameter, assuming a sphere shape[46]. A particle is equivalent to approximately five Pt4-clusters. Thus, the aggregation to form particles is concluded to be the deactivating factor.

When the $[Pt_4(\mu\text{-}CH_3COO)_8]/SiO_2$ sample was reduced with H_2 at room temperature, particles did not aggregate. It implies that formic acid induced the aggregation of Pt atoms, not enforced by H_2 formed in the formic acid decomposition. Many studies for aggregation of dispersion of metal particles by CO have been reported[47-52]. The present observation suggests the existence of mobile Pt-formates on SiO_2.

6.4. Conclusions

The catalyst employing $[Pt_4(\mu\text{-}CH_3COO)_8]$ as a precursor showed the characteristic reaction profile in the decomposition reaction of formic acid. The $[Pt_4(\mu\text{-}CH_3COO)_8]/SiO_2$ catalyst showed remarkably high catalytic activity (more than two orders of magnitude) as compared to the ion-exchanged Pt/SiO_2 catalyst. The products detected were only CO_2 and H_2 (100 % dehydrogenation), while the ion-exchanged catalyst also yielded $CO + H_2O$ in addition to $CO_2 + H_2$. The reaction on the cluster catalyst involved four characteristic steps: an induction period; a slow reaction period; a catalytic high-rate reaction period; a deactivation step. There was no change in the cluster structure in the induction period, but fast replacement of the in-plane acetate ligands by formic acid took place. In the subsequent step the in-plane formate ligands decomposed to form CO_2 and H_2, and the tetramer framework reformed to give a new Pt dimer with two acetate ligands. The dimer structure was stable under vacuum, but it was transformed quickly to a catalytically active structure in excess formic acid. The EXAFS analysis revealed that the active species was Pt monomer which has both short and long Pt-O bonds at 0.201 and 0.266 nm. The Pt monomers were unstable under a formic acid atmosphere, so aggregated to form 0.9 nm particles in competition with the catalytic decomposition of formic acid. The Pt particles were almost inactive for the decomposition reaction under the present conditions. Thus, the Pt_4-clusters were found to behave dynamically, changing the structure during the course of the formic acid decomposition reaction.

References

[1] Y. Iwasawa, *Tailored Metal Catalysts*, edited by. Y. Iwasawa(D. Reidel Publishing Company, Dorrecht , 1986).

[2] Y. Iwasawa, *Adv. Catal.*, **35**, 187 (1987).

[3] Y. Iwasawa, *Catal. Today*, **18**, 21 (1993).

[4] R. B. Bjorklund and R. L. Burwell, *J. Colloid Interface Sci.*, **70**, 383 (1979); R. L. Burwell and A. Brenner, *J. Mol. Catal.*, **1**, 77 (1975 / 76).

[5] Y. I. Yermakov, B. N. Kuznetsov and V. A. Zakharov, *Catakysis by Supported Complexes*(Elsevier, Amsterdam, 1981).

[6] W. M. H. Sachtler, and J. Fahrenfort, *Actes Congr.Int. Catal. 2nd(1960)*, 831 (1961).

[7] P. Maes, J. J. F. Scholten and P. Zwietering, *Adv. Catal.*, **14**, 35 (1963).

[8] J. M. Trillo, G. Munuera and J. N. Craido, *Catal. Rev.*, **7**, 51 (1972).

[9] Z. G. Szabó, Ed., *Contact Catalysis,*(Elsevier, Amsterdam, 1976).

[10] R. J. Madix, *Surf. Sci.*, **89**, 540 (1979).

[11] F. Solymosi, J. Kiss and I. Kovács, *J. Phys. Chem.*, **92**, 796 (1988).

[12] Z. G. Szabó, F. Solymosi, and I. Z. Batta, *Phys. Chem., N. F.*, **17**,125 (1958).

[13] Z. G. Szabó, F. Solymosi, and I. Z. Batta, *Phys. Chem. N.F.*, **23**, 56 (1960).

[14] Z. G. Szabó, and F. Solymosi, *Proc. 2nd Int. Congr. Catal., Paris*,1627 (1961).

[15] F. Solymosi, *Catal. Rev.*, **1**, 233 (1967).

[16] D. C. Grenoble, M. M. Estadt and D. F. Ollis, *J. Catal.*, **67**, 90 (1981).

[17] Y. Amenomiya, *J. Catal.*, **57**, 64 (1979).

[18] T. Shido, K. Asakura, and Y. Iwasawa, *J. Catal.*, **122**, 55 (1990).

[19] T. Shido and Y. Iwasawa, *J. Catal.*, **129**, 343 (1991).

[20] T. Shido and Y. Iwasawa, *J. Catal.*, **136**, 493 (1992).

[21] T. Shido and Y. Iwasawa, *J. Catal.*, **140**, 575 (1993).

[22] T. Shido and Y. Iwasawa, *J. Catal.*, **141**, 71 (1993).

[23] A. Deluzarche, R. Kieffer, and A. Muth, *Tetrahedron Lett.*, 3357 (1997).

[24] D. B. Clarke, D.-K. Lee, M. J. Sandoval and A. T. Bell, *J. Catal.*, **150**,81 (1994).

[25] G. C. Chinchen, K. C. Waugh and D.A. Whan, *Appl. Catal.*, **25**, 101 (1986).

[26] F. Solymosi and H. Knözinger, *J. Catal.*, **122**, 166 (1990).

[27] R. G. Herman, *Stud. Surf. Sci. Catal., (L. Guczi ed.) Elsevier*, **64**, 1 (1991).

[28] M. A. A. F. de C. T. Carrondo and A. C. Skapski, *J. Chem. Soc. Chem. Commun.*, 410 (1976).

[29] M. A. A. F. de C. T. Carrondo and A. C. Skapski, *Acta Crystallogr.*, **B34**, 1857 (1978).

[30] M. A. A. F. de C. T. Carrondo and A. C. Skapski, *Acta Crystallogr.*, **B34**, 3576 (1978).

[31] A. C. Skapski and P. G. H. Troughton, *J. Chem. Soc. (A)*, 2772 (1969).

[32] G. Albano, G. Ciani, M. I. Bruce, G. Shaw and F. G. A. Stone, *J. Organometallic Chem.*, **C99**, 42 (1972).

[33] L. T. Guggenberger, *Chem. Comm.*, 512 (1968).

[34] J. C. Calabrease, L. F. Dahl, P. Chini, G. Longoni and S. Martinengo, *J. Am. Chem. Soc.*, **96**, 2614 (1974).

[35] T. Yamaguchi, Y. Sasaki, A. Nagasawa, T. Ito, N. Koga and K. Morokuma, *Inorg. Chem.*, **28**, 4311 (1989).

[36] T. Yamaguchi, Y. Sasaki and T. Ito, *J. Am. Chem. Soc.*, **112**, 4038 (1990).

[37] N. Kosugi and H. Kuroda, *EXAFS2* ; Library of the Research Center for Spectrochemistry, The Univ. of Tokyo.

[38] T. Liu, K. Asakura, U. Lee, Y. Matsui and Y. Iwasawa, *J. Catal.*, **135**, 367 (1992).

[39] F. W. H. Kampers, C. W. Engelen, J. H. C. van Hooff and D. C. Koningsberger, *J. Phys. Chem.*, **94**, 8574 (1990).

[40] D. C. Koningsberger and R. P. Prins, *X-Ray Absorption*(J. Wiley-Interscience Publication, New York, 1980).

[41] E. A. Stern, *Phys. Rev.*, **B48**, 9825 (1993).

[42] K. Nakamoto, *Infrared and Raman Spectra of Inorganic and Coordination Compounds, 3rd ed.,* (J. Wiley-Interscience Publication, New York, 1978).

[43] S. Pinchas and I. Laulicht, *Infrared Spectra of Labelled Compounds*(Academic Press, London and New York, 1971) p126.

[44] T. Yamaguchi, Y. Sasaki, A. Nagasawa, T. Ito, N. Koga and K. Morokuma, *Inorg. Chem.*, **28**, 4312 (1989).

[45] D. C. Konigsberger, B. C. Gates, *Catal. Lett.*, **14**, 271 (1992).

[46] R. B. Greegor and F. W. Lytle, *J. Catal.*, **63**, 476 (1980).

[47] S. C. Anderson, T. Mizushima and Y. Udagawa, *J. Phys. Chem.*, **95**, 6603 (1991).

[48] H. F. J. van't Blik, J. B. A. D. van Zon, T. Huizinga, J. C. D. Vism, D. C. Koningsberger and R. Prins, *J. Phys. Chem.*, **87**, 2264 (1983).

[49] H. F. J. van't Blik, J. B. A. D. van Zon, T. Huizinga, J. C. D. Vism, D. C. Koningsberger and R. Prins, *J. Am. Chem. Soc.*, **107**, 3139 (1985).

[50] T. Mizushima, K. Tohji and Y. Udagawa, *J. Am. Chem. Soc.*, **110**, 459 (1988).

[51] T. Mizushima, K. Tohji, Y. Udagawa and A. Ueno, *J. Phys. Chem.*, **94**, 4980 (1990).

[52] F. Solymosi and M. Pasztor, *J. Phys. Chem.*, **90**, 5312 (1986).

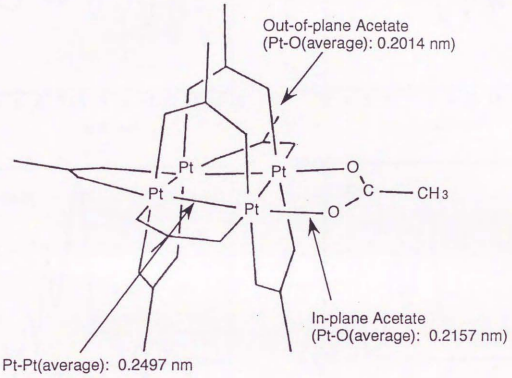

Fig. 1 Structure of $[Pt_4(\mu\text{-}CH_3COO)_8]$.

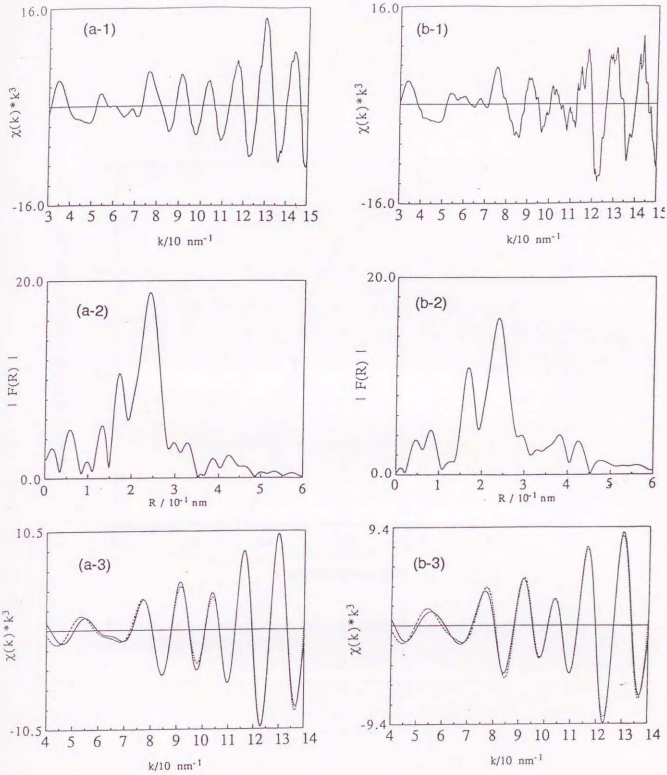

Fig. 2 EXAFS spectra for (a) $[Pt_4(\mu\text{-}CH_3COO)_8]$/BN and (b) $[Pt_4(\mu\text{-}CH_3COO)_8]$ /SiO_2 measured at 70 K; (1) k^3-weighted EXAFS oscillation; (2) Fourier transformation ($k = 30 - 150\ nm^{-1}$); (3) curve fitting (R = 0.14 - 0.29 nm)(Pt-O, Pt-O and Pt-Pt). Solid line: observed; broken line; calculated.

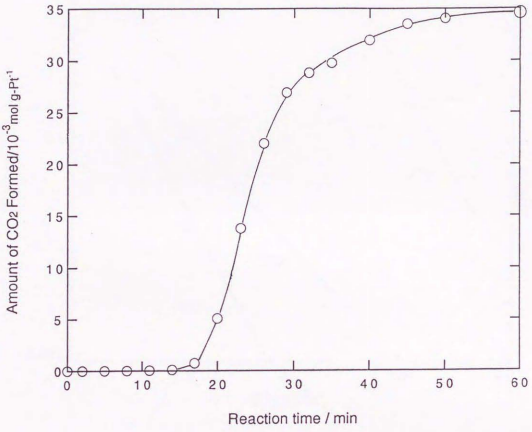

Fig. 3 Profile of the catalytic decomposition reaction of formic acid (1.47 kPa) on $[Pt_4(\mu\text{-}CH_3COO)_8]/SiO_2$ at 288 K.

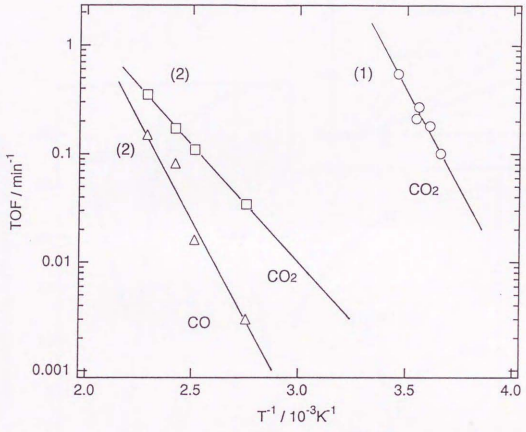

Fig. 4 Arrhenius plots for the catalytic decomposition reactions of formic acid on $[Pt_4(\mu\text{-}CH_3COO)_8]/SiO_2$ (a) and ion-exchanged Pt/SiO_2 (b).

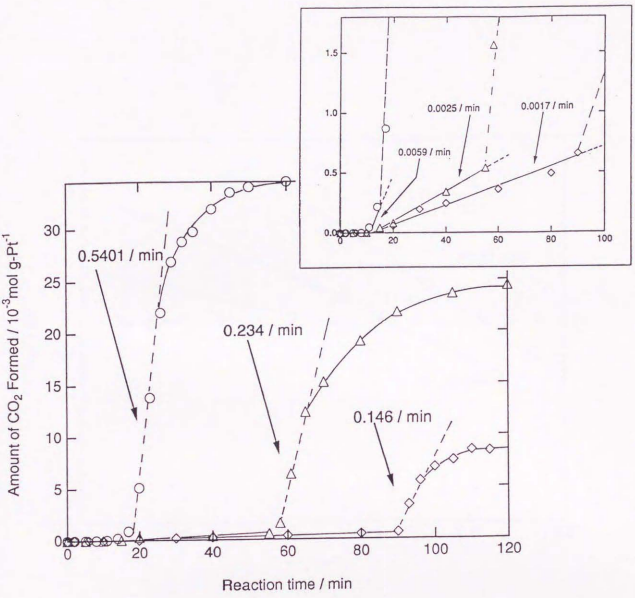

Fig. 5 Profiles of the decomposition reactions of HCOOH (○), DCOOH (△) and DCOOD(◇) at 288 K. HCOOH: 1.47 kPa; DCOOH: 1.07 kPa; DCOOD: 1.47 kPa (constant pressure). Gradients: (---, main figure) 0.5401 (○), 0.234 (△) and 0.146 min^{-1}(◇); (—, insert) 0.0059 (○), 0.0025 (△) and 0.0017 min^{-1}(◇).

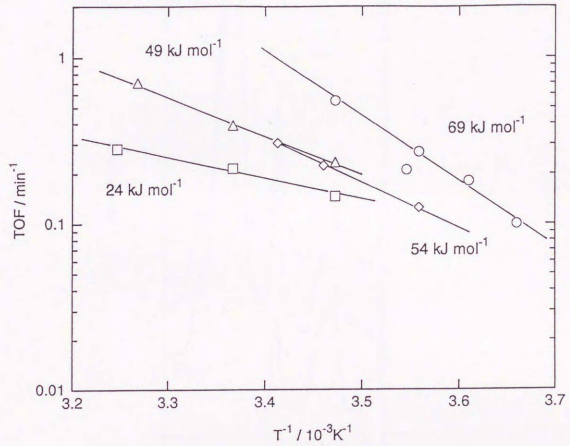

Fig. 6 Arrhenius plots for the decomposition reactions of HCOOH (○), DCOOH (△), HCOOD(◇) and DCOOD(□) with gradients of 69, 49, 54 and 24 kJmol^{-1}, respectively.

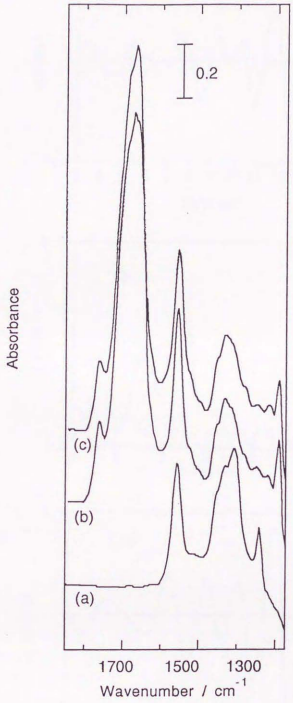

Fig. 7 IR spectra for $[Pt_4(\mu\text{-}CH_3COO)_8]/SiO_2$ in the induction period of DCOOD reaction at 305 K: (a) 0, (b) 2 and (c) 8 min.

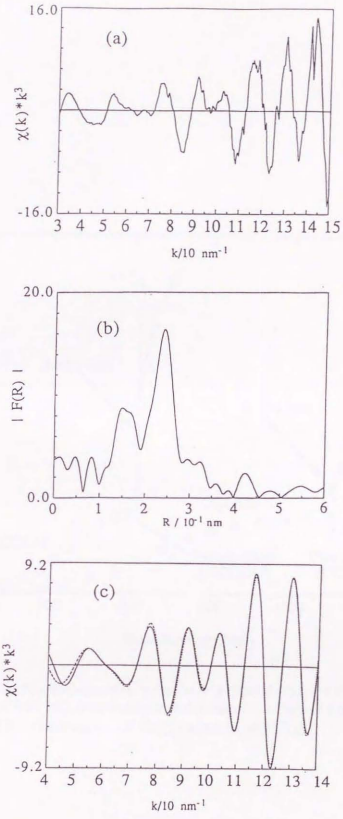

Fig. 8 EXAFS data for $[Pt_4(\mu\text{-}CH_3COO)_8]/SiO_2$ in the induction period of the HCOOH reaction at 289 K; measured at 110 K; (a) k^3-weighted EXAFS oscillation; (b) Fourier transformation($k = 30 - 150\ nm^{-1}$); (c) curve fitting ($R = 0.14 - 0.29$ nm) (Pt-O, Pt-O and Pt-Pt). Solid line: observed; broken line: calculated.

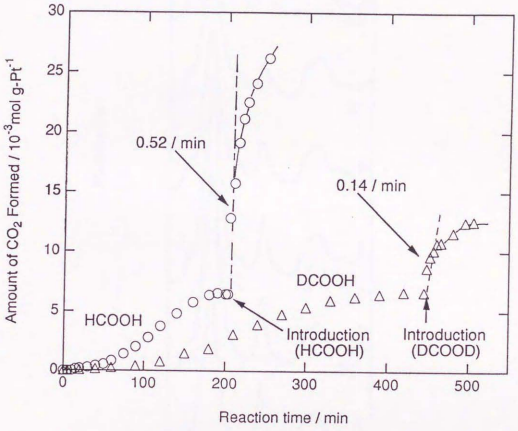

Fig. 9 Profiles of the decomposition reactions of HCOOH (○) or DCOOH (△) at an initial pressure of 0.07 kPa, followed by introduction of 1.47 kPa of HCOOH or DCOOD at 288 K. Gradient: (---) 0.52 (○) and 0.14 min^{-1}(△).

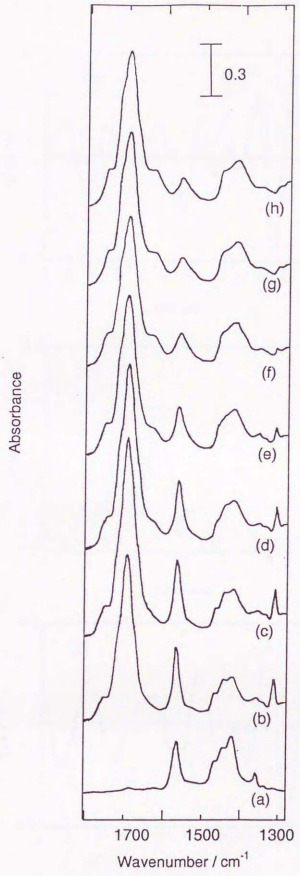

Fig. 10 IR spectra for $[Pt_4(\mu\text{-}CH_3COO)_8]/SiO_2$ in the slow reaction period at 303 K with 0.07 kPa of DCOOH: (a) 0, (b) 2, (c) 15, (d) 60, (e) 120, (f) 240, (g) 360 and (h) 420 min.

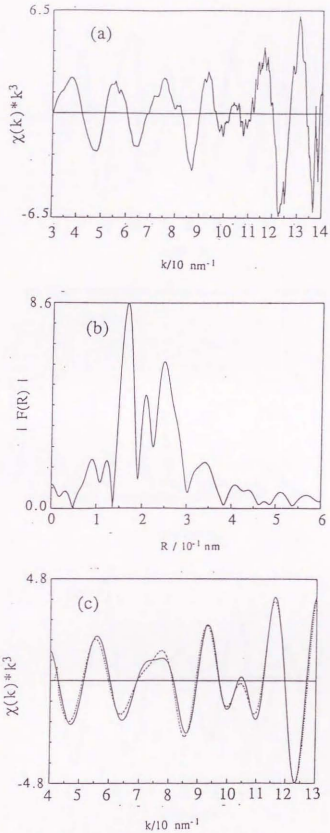

Fig. 11 EXAFS data for $[Pt_4(\mu\text{-}CH_3COO)_8]/SiO_2$ at the end of the slow reaction period at 288 K with 0.07 kPa of HCOOH after 180 min; measured at 70 K; (a) k^3-weighted EXAFS oscillation; (b) Fourier transformation($k = 30 - 140$ nm^{-1}); (c) curve fitting ($R = 0.14 - 0.30$ nm) (Pt-O, Pt-O and Pt-Pt). Solid line: observed; broken line: calculated.

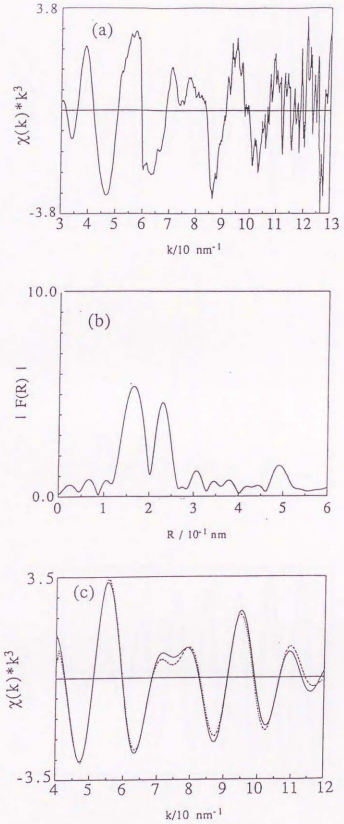

Fig. 12 EXAFS data for the catalyst in the catalytic reaction region; HCOOH: 1.47 kPa at 284 K; measured at 70 K; (a) k^3-weighted EXAFS oscillation; (b) Fourier transformation($k = 30 - 130\ nm^{-1}$); (c) curve fitting (R = 0.11 - 0.27 nm) (Pt-O + Pt-O). Solid line: observed; broken line: calculated.

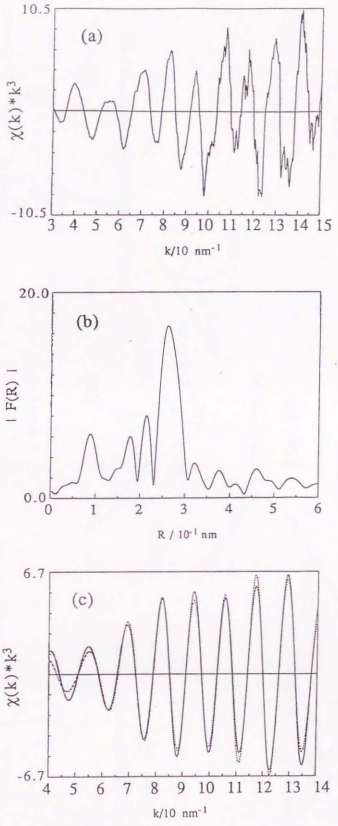

Fig. 13 EXAFS data for the deactivated catalyst measured at 70 K; (a) k^3-weighted EXAFS oscillation; (b) Fourier transformation($k = 30 - 150\ nm^{-1}$); (c) curve fitting (R = 0.18 - 0.31 nm) (Pt-Pt). Solid line: observed; broken line: calculated.

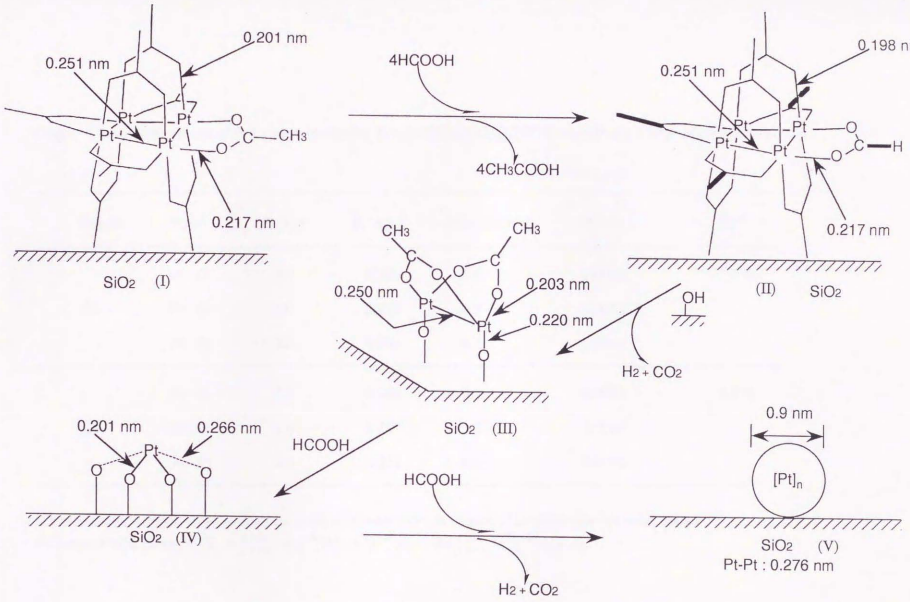

Scheme 1 Structural transformation of the $[Pt_4(\mu\text{-}CH_3COO)_8]/SiO_2$ catalyst during the course of the HCOOH decomposition reaction.

Table 1 Curve fitting results of Pt L3-edge spectra for $[Pt_4(\mu\text{-}CH_3COO)_8]/BN$ (1) and $[Pt_4(\mu\text{-}CH_3COO)_8]/SiO_2$ (2).

Sample	Bond	C. N. [a]	R / nm [b]	ΔE_0 / eV [c]	σ / nm [d]	R_f [e]
	Pt - O	2.0	0.201	-3.5	0.0056	2.2 %
(1)	Pt - O	2.0	0.217	-3.5	0.0075	
	Pt - Pt	2.0	0.251	-0.5	0.0048	
	Pt - O	2.3	0.201	-3.5	0.0060	2.6 %
(2)	Pt - O	1.9	0.217	-3.5	0.0080	
	Pt - Pt	2.0	0.251	-0.5	0.0055	

a: coordination number, b: bond distance, c: the difference between origins of the photoelectron wave vector
d: Debye-Waller factor, e: $R_f = \int_{k\,min}^{k\,max} | k^3\chi^{obs}(k) - k^3\chi^{calc}(k) |^2 \, dk \,/\, \int_{k\,min}^{k\,max} | k^3\chi^{obs}(k) |^2 \, dk$.

Table 2 IR peaks (cm^{-1}) of the bridging acetates for $[Pt_4(\mu\text{-}CH_3COO)_8]/CDCl_3$ and (b) $[Pt_4(\mu\text{-}CH_3COO)_8]/SiO_2$ (2)

assignment	(1)	(2)
$\nu_a(OCO)$	1565	1564
$\nu_s(OCO)$ [a]	1438	1442
$\nu_s(OCO)$ [b]	1414	1418
$\nu_a(CH_3)$	1457	1462
$\nu_s(CH_3)$	1347	1350

a: out-of-plane acetate; b: in-plane acetate.

Table 3 Three-wave curve fitting result of Pt L_3-edge spectra for the catalyst during the induction period

Bond	C. N.	R / nm	ΔE_0 / eV	σ / nm	R_f
Pt - O	2.4	0.198	-3.5	0.0058	2.1 %
Pt - O	2.4	0.217	-3.5	0.0070	
Pt - Pt	2.0	0.251	-0.5	0.0050	

Table 4 Three-wave curve fitting result of Pt L3-edge spectra for the catalyst at the end of the slow reaction period.

Bond	C. N.	R / nm	ΔEo / eV	σ / nm	Rf
Pt - O	2.1	0.203	2.0	0.0050	3.4 %
Pt - O	1.5	0.220	2.5	0.0040	
Pt - Pt	1.2	0.250	2.0	0.0050	

Table 5 Two-wave curve fitting result of Pt L_3-edge spectra for the catalyst for the catalyst during the catalytic reaction.

Bond	C. N.	R / nm	ΔE_0 / eV	σ / nm	R_f
Pt - O	2.2	0.201	-1.6	0.0056	3.4 %
Pt - O	2.6	0.266	1.8	0.0075	

Table 6 One-wave curve fitting result of Pt L_3-edge spectra for the deactivated catalyst.

Bond	C. N.	R / nm	ΔE_0 / eV	σ / nm	R_f
Pt - Pt	6.6	0.276	-2.3	0.0081	3.3 %

Chapter 7

In-situ Polarization-Dependent Total-Reflection Fluorescence XAFS Studies on the Structure Transformation of Pt Clusters on α-Al_2O_3 (0001)

ABSTRACT

Structures of Pt species derived from $Pt_4(\mu\text{-}CH_3COO)_8$ on an $\alpha\text{-}Al_2O_3$ (0001) single crystal surface were studied by means of in-situ polarization-dependent total reflection fluorescence XAFS(EXAFS and XANES) techniques. The Pt_4 cluster framework was destroyed upon the deposition of $Pt_4(\mu\text{-}CH_3COO)_8$ by the reaction on the $\alpha\text{-}Al_2O_3$ surface at room temperature. The isolated Pt species were converted to one-atomic layer thick Pt rafts with the Pt-Pt distance of 0.273 nm when the cluster was treated with H_2 at 373 K. The raft-like Pt clusters were stabilized by the formation of direct Pt-O-Al bonding with the $\alpha\text{-}Al_2O_3$ surface. The raft-like Pt clusters were redispersed to isolated oxidized Pt species by the reaction with NO. They were also transferred to 3-dimensional Pt particles by reduction with H_2 at 773 K.

7.1 Introduction

Industrial metal catalysts are usually used as metal particles supported on high surface area metal oxide surfaces. The role of support oxides is not only to disperse the metal particles but also to modify the morphology, orientation and electronic state of the metal particles through metal-support interaction, which are the most relevant factor to supported metal catalysis. EXAFS (Extended X-ray Absorption Fine Structure) is regarded as a powerful tool to gain the information about the morphology of metal particles and metal-support bonding. The particle morphology can be obtained by the analysis of the coordination number of metal-metal bonding[1]. The metal-support distance can be determined by detecting the EXAFS signal of atoms(mostly oxygen) at the support surface. However, it is not straightforward to obtain such type of precise structural information from conventional EXAFS for powder catalyst sample because of the following reasons. First, the coordination number determined by EXAFS suffers from many factors like the effects of thermal and static disorder or asymmetry of pair

distribution function. Second the metal-support bond, especially metal-oxygen bond with a small coordination number has a small contribution to whole EXAFS spectra and is hindered by metal-metal bond because the EXAFS oscillation for oxygen does not continue to the high k-region.

The amplitude of EXAFS oscillation depends on the direction of X-ray electric-field vector [2, 3]. As a result the effective coordination number N* is expressed by eq. (1),

$$N^* = 3\sum_j \cos^2\theta_j \qquad (1),$$

where θj is an angle between the polarization vector and the bond vector. When the polarization vector is parallel to the surface (s-polarization), EXAFS will provide the information on the bondings parallel to the surface. When the polarization vector is perpendicular to the surface (p-polarization), the information about the structure perpendicular to the surface, i.e., the metal-support bond is selectively obtained. Since the conventional supported metal catalysts are used in a powder form, the EXAFS oscillations are averaged over all directions. On the other hand, when the flat oxide substrates are used, the structural information parallel and perpendicular to the surface can be separately obtained by the polarization-dependent EXAFS measurements. However, a problem is to measure the surface species of low concentrations. Concentrations of monolayer metal on a flat surface are in the range 10^{14}-10^{15} atoms cm^{-2}, which is 4 - 5 orders of magnitude lower than concentrations of metals for conventional catalysts in a powder form. Usually fluorescence yield detection is more preferable for dilute samples than monitoring of direct absorption. In a soft X-ray region, the fluorescence-detection mode successfully gives the EXAFS signals with high quality[4-7] and the polarization-dependent EXAFS studies determine the adsorption sites of lighter elements such as C, O, S, Cl, and P [8, 9]. On the other hand, most of the catalytic important elements have the X-ray absorption edges higher than 4 keV. The X-ray with such a high energy can penetrate deeply into the bulk, yielding a large amount of scattering X-rays which make it difficult to measure

monolayer species supported on the flat substrate. When the X-ray hits on the flat substrate with the incident angle less than the critical angle δc, it undergoes a total reflection and penetrates only a few nm into the bulk. Consequently the scattering X-ray from the bulk is dramatically reduced[10]. After Heald et al. showed the possibility of the detection of EXAFS signals from a monolayer Au film deposited on a flat glass substrate by use of a total reflection fluorescence technique [11], the total-reflection fluorescence EXAFS technique has been applied to semiconducting materials, electrodes and corrosive surfaces[12]. The technique has also been applied to catalytically interesting systems[13-17]. By analyzing the polarization dependence of EXAFS amplitude, it was revealed the orientation and growth mode of catalytic active species such as Co oxides and Cu oxides on flat inorganic oxide substrates as model systems for supported powder catalysts.

XANES (X-ray Absorption Near Edge Structure) spectra give information about electronic state and geometrical configuration and also show similar polarization dependence. Thus the combination of EXAFS and XANES, so-called XAFS (X-ray Absorption Fine Structure), will give clear insight into the morphology, orientation and metal-support interaction. Moreover, the fluorescence XAFS allows us to carry out in-situ measurements on the structure of catalysts in the working conditions. An in-situ chamber for polarization-dependent total reflection fluorescence EXAFS measurement were designed to carry out under various conditions from UHV (10^{-9} Pa) to high pressure (10^{5} Pa) and from low temperature (100 K) to high temperature (800 K)[18] .

In this chapter this in-situ chamber was employed for the measurement of the polarization-dependence total-reflection fluorescence XAFS (hereinafter it is abbreviated as PTRF-XAFS) for Pt species deposited on α-Al_2O_3 (0001) using a [$Pt_4(\mu$-$CH_3COO)_8$] complex as a precursor. The PTRF-XAFS technique demonstrated that isolated Pt monomeric species and one-atomic layer thick Pt rafts were formed on the α-Al_2O_3 (0001) surface and reversibly transformed between them depending on the treatment and the atmosphere.

7.2 Experimental

7.2.1 Preparation of materials

The cluster $[Pt_4(\mu\text{-}CH_3COO)_8]$ was prepared following the literature-. An optical-grade polished $\alpha\text{-}Al_2O_3$ (0001) crystal was purchased from Earth Jewelry Co.. The single crystal (10 x 30 x 1 mm^3) was calcined at 573 K for 2 h followed by evacuation at the same temperature for 1 h. The preparation steps are summarized in scheme 1. Pt was deposited on the $\alpha\text{-}Al_2O_3$ (0001) surface by a dropwise impregnation method using a CH_2Cl_2 solution of $[Pt_4(\mu\text{-}CH_3COO)_8]$ in the in-situ chamber[18] under a flow of high purity Ar(99.999%). The loading was estimated to be 1.5 Pt_4 nm^{-2} by XPS, which corresponds to an atomic ratio of Pt: surface oxygen = 4 : 10. The solvent was removed by evacuation under high vacuum at room temperature. The incipient supported sample A was then reduced at 373 K with H_2 (13.3 kPa) to form species B in the chamber. The species B was further reduced to species C by H_2 (13.3 kPa) at 673 K. Species B was also exposed to NO (1.33 kPa) at room temperature in the chamber (Species D).

7.2.2 PTRF-XAFS measurements

The details of the in-situ XAFS chamber was described elsewhere[18]. Here it is briefly described about the in-situ XAFS chamber, in which the XAFS spectra can be obtained under various conditions: from high vacuum (1 x 10^{-9} Pa) to high pressure (1 x 10^5 Pa) and from low temperature (100 K) to high temperature (800 K). A wide degree (100 °) of rotation of the sample around the X-ray light axis enables us to measure the XAFS of the same sample in different X-ray polarization vectors without exposure to air. The fluorescence X-ray was detected by an NaI(Tl) scintillation counter which can be set close to the sample surface. The XAFS was measured at BL-7C of

the Photon Factory in the National Laboratory for High Energy Physics (KEK-PF) using Si(111) sagittal focusing double crystal monochromator[22]. Higher harmonics were removed by a double mirror made from fused quartz. The energy resolution was about 2 eV at 9 keV. The incident X-ray was monitored by a 5.5 cm ionization chamber filled with N_2 gas. Although it is better to measure Pt L_1-edge because eq. (1) can be directly used for the analysis of the polarization dependence of EXAFS amplitude, the edge height of Pt L_1 was so small that the EXAFS oscillation tolerable for data analyses could not be obtained. Instead, Pt L_3-edge spectra were measured . Thus eq. (1) should be modified as discussed later. All measurements were carried out at room temperature. One of the difficulties in the total-reflection fluorescence technique is diffraction from the single crystal substrate. It can be removed by putting small pieces of lead plates at the positions of the detector window on which the Bragg diffractions hit. The other one is low intensity of the signals. The X-ray beam was collimated onto the substrate surface using a pin-hole to eliminate undesirable scattering from the other part than substrate surface. It took 12 hours to obtain a whole spectrum. The species A was measured under high vacuum conditions. The measurements of samples B and C were done in the presence of H_2 and that of sample D was performed under NO atmosphere.

7.2.3 Data analysis

The EXAFS spectra were calculated directly from the ratio of the fluorescence from the sample to the incident X-ray signal detected by an ionization chamber (I_f / I_0) without any correction for self absorption because the Pt atoms were located only on the surface. The EXAFS oscillation, $\chi(k)$, was extracted from the spectra by a cubic spline method and normalized by the edge height using EXAFS analysis program REX[23]. The energy dependence of the edge height was taken into account using McMaster equation[24]. The origin of kinetic energy of photoelectron was temporarily taken in an

inflection point of the edge jump. The Fourier filtered data were then analyzed by curve fitting analysis using eq. (2)[25]:

$$\chi(k_j) = \sum_j \frac{N_j^* F_j(k_j)}{kr_j^2} \exp(-2\sigma_j^2 k_j^2) \exp(-2r_j/\lambda_j) \sin(2k_j r_j + \phi_j(k_j)), \qquad (2)$$

where k_j, r_j, σ_j, λ_j, $F_j(k)$ and $\phi_j(k)$ are wave-number of photoelectron, interatomic distance, Debye-Waller factor, mean free path of photoelectron, backscattering amplitude function and phase shift function for j-th shell, respectively. The $F_j(k)$ and $\phi_j(k)$ for Pt-Pt are derived from Pt foil. Those for Pt-O were calculated from feff v5.05 with Pt-O = 0.20 nm[26]. Since the absolute value of the theoretically derived amplitude is smaller by a factor of 0.7 - 0.9 than the actual amplitude, it was corrected by using the coordination number of 6 for Pt-O bonding in $(NH_4)_4[H_4PtMo_7O_{24}]$. The origin of photoelectron kinetic energy was adjusted using the following relation (3) in the curve fitting process:

$$k_j^2 = k^2 - 2m\Delta E_j / h \qquad (3),$$

where ΔE_j and m are the deviation of the origin of photoelectron kinetic energy and the mass of electron, respectively.

The equation (1) is no longer valid for L_3-edge spectra because the L_3-edge EXAFS corresponds to the transition of angular momentum from l=1 to l=0, 2. Therefore, the polarization dependence of EXAFS is expressed by eq. (4) for $L_{2,3}$ edges [27], instead of eq.(1).

$$\chi(k) = \sum_j \frac{F_j(k)}{kr_j^2} \exp(-2\sigma_j^2 k^2) \exp(-2r_j/\lambda)$$
$$\times\{1/2(1+3\cos^2\theta_j)|M_{21}|^2 \sin(2kr_j + \phi_{2j}) + 1/2|M_{01}|^2 \sin(2kr_j + \phi_{0j})$$
$$+ M_{01}M_{21}(1-3\cos^2\theta_j)\sin(2kr_j + \phi_{02j})\}/(|M_{21}|^2 + 1/2|M_{01}|^2), \qquad (4)$$

where M_{01} and M_{21} are dipole moments for the transitions from l = 1 to l = 0 and l = 2, respectively. ϕ_{0j}, ϕ_{2j}, and ϕ_{02j} are phase shift functions for the transitions from l=1 to l=0, from l=1 to l=2 and their cross term, respectively. Since (M_{01}/M_{21}) is about 0.2, it was adopted the following assumptions for simplification in the present EXAFS analysis:

$\phi_{02j}(k) = \phi_{2j}(k)$,

$(M_{01} / M_{21}) = 0.2$,

$(M_{01} / M_{21})^2$ is negligible small.

Then the equation (4) can be simplified to equation (5)[28]:

$$\chi(k) = \sum_j \frac{F_j(k)}{kr_j^2} \exp(-2\sigma_j^2 k^2) \exp(-2r_j / \lambda_j) \sin(2kr_j + \phi_{2j}(k_j)) \quad , \qquad (5)$$

In this case N* is expressed as follows:

$$N^* = \sum_k (0.7 + 0.9\cos^2\theta_k) \quad , \qquad (6)$$

Note that the polarization dependence for L_3 edge is not perfect and one may observe Pt-X bonding even though the Pt-X bond direction is perpendicular to the X-ray polarization. In this chapter, it refereed that s-polarization and p-polarization, the electric-field vectors are parallel to the surface and perpendicular to the surface, respectively.

7.2.4 Catalytic reaction

Catalytic activity for decomposition reaction of HCOOH on the α-Al_2O_3-supported $Pt_4(\mu\text{-}CH_3COO)_8$ powder was checked in a closed circulating system connected to a gas chromatography (Shimadzu Co, GC-8A) with a Porapack PS column. The pressure of HCOOH was 1.47 kPa and the reaction temperature was 288 K.

7.3 Results and discussion

7.3.1 Catalytic performance.

Figure 1 shows the activity of $Pt_4(\mu\text{-}CH_3COO)_8$ dispersed on α-Al_2O_3 for the HCOOH decomposition reaction at 288 K. HCOOH was selectively decomposed to CO_2 and H_2 without any formation of CO and H_2O, contrasted to the HCOOH

decomposition on Al_2O_3 -supported Pt particles prepared by a traditional impregnation method using an aqueous solution, followed by the reduction with H_2 where both CO_2 + H_2 and CO + H_2O were produced with a much lower activity. For comparison the activity of $Pt_4(\mu\text{-}CH_3COO)_8$ supported on SiO_2 is shown in Fig. 1. As has already been described in Chapter 6, the SiO_2-supported $Pt_4(\mu\text{-}CH_3COO)_8$ showed a long induction period which became much longer for DCOOH and DCOOD[29]. The reaction on the SiO_2 -supported $Pt_4(\mu\text{-}CH_3COO)_8$ terminated at ca. 10 min after the reaction initiation because the Pt species was reduced to Pt metal particles during the reaction. Unlike the SiO_2-supported Pt species, Pt species on α-Al_2O_3 did not show any induction period. The initial rate for the formation of CO_2 per Pt_4 (turnover frequency) was 4.4 min^{-1} which is twice as large as the maximum reaction rate for the $Pt_4(\mu\text{-}CH_3COO)_8/SiO_2$.

7.3.2 Structure of Pt species A

Figure 2(A) shows the EXAFS oscillations parallel (s-polarization) and perpendicular (p-polarization) to the α-$Al_2O_3(0001)$ surface. The period and amplitude of the EXAFS oscillations in both directions are similar with each other. The corresponding Fourier transforms over k = 30 - 90 nm^{-1} give one peak around 0.17 nm (phase shift: uncorrected) for both directions as shown in Fig. 2(B). The original cluster $Pt_4(\mu\text{-}CH_3COO)_8$ has the Pt-Pt distance at 0.2495 nm which will give the Fourier transform peak around 0.20 nm (phase shift: uncorrected)[29]. However, there was no peak in this region for both s and p-polarizations, indicating that the Pt_4 cluster framework was destroyed. Moreover, no peak corresponding to Pt-Pt bond of Pt metal particles was observed around 0.25 nm (phase shift: uncorrected) in the Fourier transforms for both directions. Thus Pt atoms are monoatomically dispersed on the α-Al_2O_3 surface by the interaction with the substrate surface.

The curve fitting analysis were carried out on the inversely Fourier transformed data of the first peaks filtered over 0.1 - 0.22 nm. Figure 3 shows the curve-fitting results in p-polarization and s-polarization. The structure parameters thus obtained are summarized in Table 1. The Pt-O bonds are found at about 0.200 ± 0.003 nm in both directions. The effective coordination numbers (N^*) for p-polarization and s-polarization are 3.3 and 3.0, respectively (Table 1). The effective coordination numbers were calculated using eq. (6) assuming typical adsorption site models for Pt atoms on α-Al_2O_3(0001) in Table 2. It was postulated three surface sites such as atop, bridge and three-fold sites on the unreconstructed α-Al_2O_3(0001) surface (O-O distance =0.275 nm) as shown in Fig. 4. Among the expected N^* values in both polarizations and their ratios for the three Pt sites, only the three-fold site model can reproduce the observed data as shown in Table 2. The location of Pt atoms are illustrated in Fig. 4. The α-Al_2O_3(0001) has two types of three-fold hollow site which are distinguished by the presence of the underneath Al atom. Here the site which has no Al atom underneath the Pt is called as fcc site and the other site which has an Al atom below is called as hcp site. In our previous report Co atoms on α-Al_2O_3(0001) were demonstrated to occupy the fcc hollow sites of the surface where no Al was located under the Co atoms in the second surface layer of Al_2O_3 because it was not observe the Co-Al interaction in the p-polarization PTRF-EXAFS spectrum[16]. Although the peak appeared around 0.3 nm in Fig. 2(B), it was difficult to assign it to Pt-Al because the peak height is nearly in the noise level. In this work I can not determine whether the location of Pt is fcc or hcp sites.

The Pt/α-Al_2O_3 and the Pt/SiO_2 catalysts derived from $Pt_4(\mu\text{-}CH_3COO)_8$ as precursor show high activity for the selective dehydrogenation of HCOOH described above. While the Pt/SiO_2 has a long induction period, the Pt/α-Al2O3 shows no induction period (Fig.1). The active species on Pt/SiO_2 was found to be Pt monomers which were bound to the SiO_2 surface making Pt-O bonds[29]. During the induction period the $Pt_4(\mu\text{-}CH_3COO)_8$ cluster framework on SiO_2 was decomposed to monomers via a Pt dimer structure with the Pt-Pt distance at 0.250 nm by the exposure

to HCOOH. The present EXAFS analysis reveals that Pt monomers are readily formed after the deposition of $Pt_4(\mu\text{-}CH_3COO)_8$ cluster on $\alpha\text{-}Al_2O_3(0001)$ surface. Since the Pt monomer structure has already been present before the catalytic reaction, there is no induction period in the reaction. Such a different behavior of $Pt_4(\mu\text{-}CH_3COO)_8$ clusters on SiO_2 and Al_2O_3 can be compared to the different structural transformation of Ru clusters and Rh dimers on SiO_2 and Al_2O_3[30, 31], where the metal-metal bonds of the cluster and the dimer were observed on SiO2 surface though the atomically dispersed species were present on the Al_2O_3.

7.3.3 Structure of Pt species B

Figure 5(A) shows the EXAFS oscillations for Pt species B prepared by the reduction of species A at 373 K with H_2 (scheme 1). The oscillation in s-polarization lasts to the high k-region compared to that in p-polarization. Figure 5(B) shows the Fourier transformation of the EXAFS oscillations. The peak appears around 0.22 nm (phase shift: uncorrected) in both directions. However, the peak height for the Fourier transform of the p-polarization is 60 % of that of the s-polarization. In addition the p-polarization has a shoulder structure in the lower side of the main peak. A curve fitting analysis was carried out assuming that the main peak in s-polarization was due to Pt-Pt bonding. Since the shoulder structure appears only in p-polarization and it is attributable to Pt-O bonding, two term fitting was carried out including Pt-Pt and Pt-O. Consequently, it was obtained better fitting by the two-term analysis than the one-term (Pt-Pt) analysis. The best fitting results are depicted in Fig. 6 and in Table 3. The Pt-Pt distances are determined to be 0.273 ± 0.003 nm which is 0.005 nm shorter than that of Pt foil. The effective coordination number (N^*) of Pt-Pt for s-polarization is twice as large as that for p-polarization. If the Pt particles have a spherical shape, the N^* would give an equal value for s- and p-polarizations. Thus it is suggested that the anisotropic structures such as thin layer, semi-spherical, and ellipsoid are formed for Pt clusters on

the Al_2O_3 surface. The N^* were calculated based on such as one atomic layer, two atomic layer and three atomic layer raft models using eq. (5). Figure 7 shows the relation between N^* for Pt-Pt and the number of the layer as a function of the particle size (in diameter). The observed N^*'s , 3 for p-polarization and 6 for s-polarization, fit the expected values only for the one atomic layer raft structure. The other model, such as more than two layer, semi-sphere and ellipsoid do not entirely reproduce the observed data. Furthermore, the particle size (diameter) of the Pt raft can be estimated to be ca. 1.5 ± 0.5 nm from the observed and calculated N^* values for the p- and s-polarization as shown in Fig. 7.

For the one layer raft structure strong Pt-support interaction may be expected. In fact, the better fitting results were obtained for the p-polarization EXAFS when Pt-O was assumed. The Pt-O distance was determined as 0.220 ± 0.009 nm as shown in Table 3. The large error bar in Pt-O was due to the overlap with the oscillation of Pt-Pt bond. The model structure for Pt rafts interacted with the oxygen layer of the α-Al_2O_3(0001) surface is illustrated in Fig. 8. Raft-like structures of supported metal particles have been proposed for Ru/SiO_2, Os/SiO_2, Ru-Os/SiO_2 and Ir-Pt/Al_2O_3 by TEM and EXAFS and Ru-Cu particles on SiO_2 by TEM and EXAFS[1, 32-35]. Yates et al. also reported a raft structure for Rh particles on Al_2O_3 by means of TEM, chemisorption and IR[36]. The raft-like structures have also been demonstrated by observing the direct metal-oxygen (support) bonding[37-40]. The PTRF-EXAFS can determine more directly the raft structure by comparing the EXAFS oscillations in two directions, perpendicular and parallel to the surface. The PTRF-EXAFS showed the presence of metal-oxygen (support) bond which was difficult to detect by conventional EXAFS because a small contribution of the metal-oxygen bonding as compared to a large contribution of the metal-metal bonding except for very small metal cluster systems. Koningsberger et al. used a difference file method to remove the large contribution of metal-metal bonding[40]. They reported the metal-oxygen distances in the supported noble metal powder catalysts which were present around 0.25-0.27 nm when the sample

was reduced at low temperatures and in the presence of H_2, while the Pt-O bond length decreased to ca. 0.22 nm when the sample was evacuated or reduced at high temperatures (>723 K)[41]. In the present work on the α-Al_2O_3(0001) single crystal surface I found the Pt-O distance at 0.220 nm even reduced with H_2 at low temperature (373 K) and in the presence of H_2 which indicated the formation of the covalent bonds between Pt atoms and surface oxygen atoms. Such a strong Pt-O interaction stabilizes the Pt raft-like structure.

When the Pt clusters were reduced at 673 K, the Pt atoms were aggregated to 3-dimensional particles. Figure 9 shows the polarization-dependent XANES spectra at the L_3-edge of Pt species on α-Al_2O_3(0001). The L_3-edge peak intensity reflects the vacancy of the 5 d state[42, 43]. The species A exhibits a strong edge peak for both s- and p-polarizations, which indicates that the monoatomically dispersed Pt atoms possess positive charge induced by the Pt-O-Al bonding. The species B formed by the reduction at 373 K shows different XANES spectra between s- and p-polarizations. The detailed analysis of XANES for the species B will be discussed elsewhere[44] but here the results derived from the XANES analysis are summarized. The XANES feature of species B for s-polarization (Fig. 9(c)) is similar to that of the supported small Pt metal particles with 100 % dispersion (H/Pt = 1.0) and with adsorbed hydrogen[45]. On the other hand, the XANES spectrum in p-polarization shows a strong white line peak, indicating the positive oxidation state. The XANES spectrum in s-polarization (Fig. 9(c)) reflects metal-metal bonding in the plane of the raft, while that in p-polarization (Fig. 9(d)) is influenced mainly by the Pt-O bonding. After the reduction of the species B at 673 K, the XANES spectra were found to be similar for s-(Fig. 9(e)) and p-polarizations (Fig.9(f)). The structures A, B, and C in the XANES spectra of Figs. 9(e) and (f) appeared at the same positions as those for Pt foil, which suggests the formation of Pt particles. No polarization dependence of the XANES spectra indicates the growth of 3 dimensional Pt particles on the α-Al_2O_3(0001) surface after the 673 K reduction.

7.3.4 Structure of species D after the exposure of B to NO

When species B was exposed to NO at room temperature, the Pt-Pt bond was cleaved. As shown in Fig. 10.(b), no peak due to Pt-Pt bond appeared in the Fourier transform for s-polarization in which the Pt-Pt peak in the sample B had been observed before NO adsorption. The Pt raft was destroyed to monomer species by the interaction with NO. The peak observed in the Fourier transform (Fig.10(b)) was analyzed to be due to Pt-O at 0.205 nm. In the p-polarization spectrum it was not able to find definite EXAFS oscillation and no peak above noise level was observed in Fig.10(a). The EXAFS oscillation for p polarization might be composed of Pt-oxygen (support) and Pt-NO (adsorbed). It is inferred that the EXAFS oscillation might smear out because of the interference of the different interatomic distances between Pt-oxygen (support) and Pt-adsorbates.

7.4 Conclusions

In this chapter, I have reported the polarization-dependent total-reflection fluorescence XAFS(EXAFS and XANES) studies on the Pt cluster on α-Al_2O_3(0001). This technique gives clearer information on adsorption sites of metal atoms, metal-support and metal-metal bondings, and anisotropic surface structures.

The structural transformation of the Pt_4 clusters on α-Al_2O_3((0001) is summarized in Fig.11. The Pt_4 cluster framework is destroyed to Pt monomers which occupy the 3-fold hollow sites of the oxygen atoms of α-Al_2O_3((0001) surface, making Pt-O bonds at the distance of 0.200 ± 0.003 nm. The isolated Pt atoms are reduced to one-atomic layer thick raft cluster with H_2 at 373 K. The Pt-Pt and Pt-O bondings are observed at 0.273 nm and 0.220 nm, respectively. The Pt rafts are redispersed to Pt monomers by the exposure of NO, or agglomerated to 3 dimensional particles by the 673 K-reduction.

References

[1] R. B. Greegor, F. W. Lytle, *J.Catal.*, **63**, 476 (1980).

[2] D. C. Koningsberger, R. Prins, R., *X-ray absorption, Principles, applications, techniques of EXAFS, SEXAFS, and XANES*(John Wiley & Sons: New York, 1988)Vol. 92. 141

[3] Y. Iwasawa, *X-ray absorption fine Structure for catalysts and surfaces* (World Scientific: Singapore, 1996) Vol. **2**.

[4] J. Stohr, E. B. Kollin, D. A. Fischer, J. B. Hastings, F. Zaera, F. Sette, *Phys.Rev.Lett.* , **55**, 1468 (1985).

[5] D. A. Fischer, J. B. Hastings, D. Zaera, J. Stohr, D. Sette, *Nulear Instrum.Methods*, A**246**, 561(1986).

[6] M. Funabashi, T. Ohta, T. Yokoyama, Y. Kitajima, H. Kuroda, *Rev.Sci.Instrum* , **60**, 2505(1989).

[7] M. Funabashi, T. Yokoyama, Y. Takata, T. Ohta, H. Kuroda, *Surf.Sci.*, **242**, 59(1990).

[8] J. Stohr, in *X-ray absorption Principles, Applications, Techniques of EXAFS, SEXAFS, and XANES.;* edited by R. Prins, D. C. Koningsberger(A John Wiley & Sons, New York, 1988) p 443.

[9] T. Ohta, in *X-ray absorption fine structure for catalysts and surfaces*; edited by Y. Iwasawa(World Scientific, Singapore, 1996)Vol. **2**, p 354.

[10] L. G. Parratt, *Phys.Rev.*, **95**, 359(1954).

[11] M. Heald, E. Keller, E. A. Stern, *Phys.Lett.*, **103A**, 155(1984).

[12] M. Shirai, Y. Iwasawa, in *XAFS application to catalysis and surface*; edited by Y. Iwasawa(Elsevier, Amsterdam, 1996) p332.

[13] M. Shirai, K. Asakura, Y. Iwasawa, *Catal.Lett.*, **15**, 247(1992).

[14] M. Shirai, K. Asakura, Y. Iwasawa, *Catal.Lett.*, 1037(1992).

[15] M. Shirai, K. Asakura, Y. Iwasawa, *Jpn. J. Appl. Phys.*, Part 1, **32**, 413(1993).

[16] M. Shirai, T. Inoue, H. Onishi, K. Asakura, Y. Iwasawa, *J.Catal.*, **145**, 159(1994).

[17] M. Shirai, K. Asakura, Y. Iwasawa, *Catal.Lett.*, **26**, 229(1994).

[18] M. Shirai, M. Nomura, K. Asakura, Y. Iwasawa, *Rev.Sci.Instrum.*, **66**, 5493(1995).

[19] T. Yamaguchi, Y. Sasaki, A. Nagasawa, T. Ito, N. Koga, K. Morokuma, *Inorg. Chem.*, **28**, 4311(1989).

[20] T. Yamaguchi; *Doctor Thesis*(Tohoku University, 1989).

[21] T. Yamaguchi, Y. Sasaki, T. Ito, *J.Am.Chem.Soc.*, **112**, 4038(1990).

[22] M. Nomura, A. Koyama, M. Sakurai; *KEK Report*, **91-1**, 1(1991).

[23] EXAFS analysis program package "*REX ver 2.04*"(Rigaku Industrial Corporation, 1993).

[24] K. Asakura, in *X-ray Absorption Fine Structure for Catalysts and Surfaces*; edited by Y. Iwasawa(World Scientific, Singapore, 1996)Vol. **2**, p 33.

[25] B. K. Teo, P. A. Lee, A. L. Simons, P. Eisenberg, B. M. Kincaid, *J.Am.Chem.Soc.*, **99**, 3854(1977).

[26] J. J. Rehr, J. Mustre de Leon, S. I. Zabinsky, R. C. Albers, *J.Am.Chem.Soc.* 1991, **113**, 5135.

[27] B. K. Teo, P. A. Lee, *J.Am. Chem.Soc.* **101**, 2815(1979).

[28] F. Comin, P. H. Citrin, P. Eisenberger, J. E. Rowe, *Phys.Rev.B*, **26**, 7060(1982).

[29] W. J. Chun, K. Tomishige, M. Hamakado, Y. Iwasawa, K. Asakura, *J.Chem.Soc., Faraday Trans.*, **91**, 4161(1995).

[30] K. Asakura, Y. Iwasawa, *J.Chem.Soc., Faraday Trans.*,I, **84**, 2445(1988).

[31] K. K. Bando, K. Asakura, H. Arakawa, K. Isobe, Y. Iwasawa, *J.Phys.Chem.*, **100**, 13636(1996).

[32] E. B. Prestridge, G. H. Via, J. H. Sinfelt, *J.Catal.*, **50**, 115(1977).

[33] F. W. Lytle, G. H. Via, J. H. Sinfelt, *J.Chem.Phys.*, **67**, 3831(1977).

[34] G. H. Via, J. H. Sinfelt, F. W. Lytle, *J.Chem.Phys.*, **71**, 690(1979).

[35] J. H. Sinfelt, G. H. Via, F. W. Lytle, *J.Chem.Phys.*, **76**, 2779(1982).

[36] D. J. C. Yates, L. L. Murrel, E. B. Prestridge, *J.Catal.*, **57**, 41(1979).

[37] A. S. Fung, P. A. Tooley, M. J. Kelly, D. C. Koningsberger, B. C. Gates, *J.Phys.Chem.*, **95**, 225(1991).

[38] F. B. M. Van Zon, S. D. Maloney, B. C. Gates, D. C. Koningsberger, *J.Am.Chem.Soc.*, **115**, 10317(1993).

[39] K. Asakura, M. Yamada, Y. Iwasawa, H. Kuroda, *Chem.Lett.*,511(1985): K. Asakura, Y. Iwasawa, *J.Chem.Soc., Faraday Trans.*, **86**, 2657(1990).

[40] J. B. A. D. van Zon, D. C. Koningsberger, H. F. J. van't Blik, R. Prins, D. E. Sayers, *J. Chem.Phys.*, **80**, 3914(1984).

[41] D.C. Koningsberger, B. C. Gates, *Catal.Lett.*, **14**, 271(1992).

[42] F. W. Lytle,P. S. P. Wei, R. B. Greegor, G. H. Via, J. H. Sinfelt, *J.Chem.Phys.*, **70**, 4849(1979).

[43] J. A. Horsley, *J.Chem.Phys.*,**76**, 1451(1982).

[44] K. Asakura, W.-J. Chun, T. Kubota, Y. Iwasawa, to be published.

[45] T. Kubota, K. Asakura, N. Ichikuni, Y. Iwasawa, *Chem. Phys. Lett.*, **256**,445(1986).

SCHEME 1: Preparation Route of Pt Cluster on α-Al_2O_3 (0001).

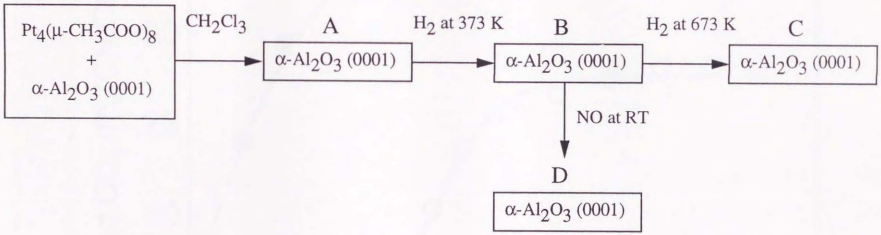

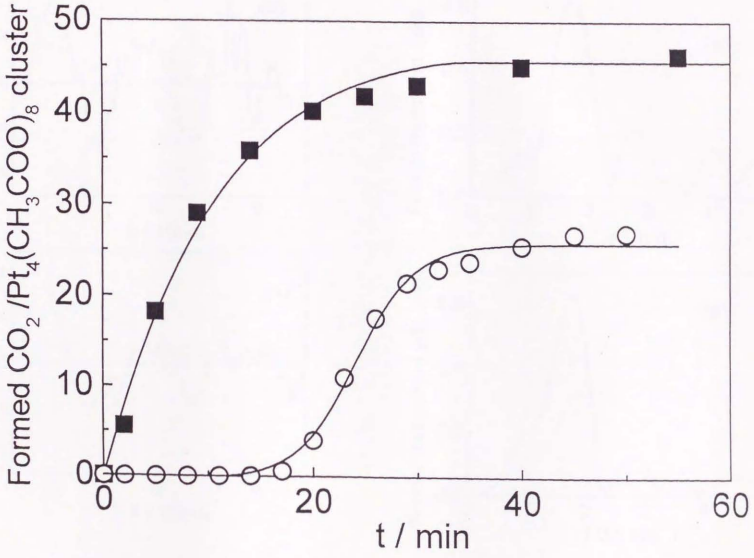

Fig. 1. The amount of formed CO_2 during HCOOH decomposition reaction on the Pt species derived from $Pt_4(\mu\text{-}CH_3COO)_8$/ $\alpha\text{-}Al_2O_3$ (■) and $Pt_4(\mu\text{-}CH_3COO)_8$ /SiO_2 (○) at 288 K.

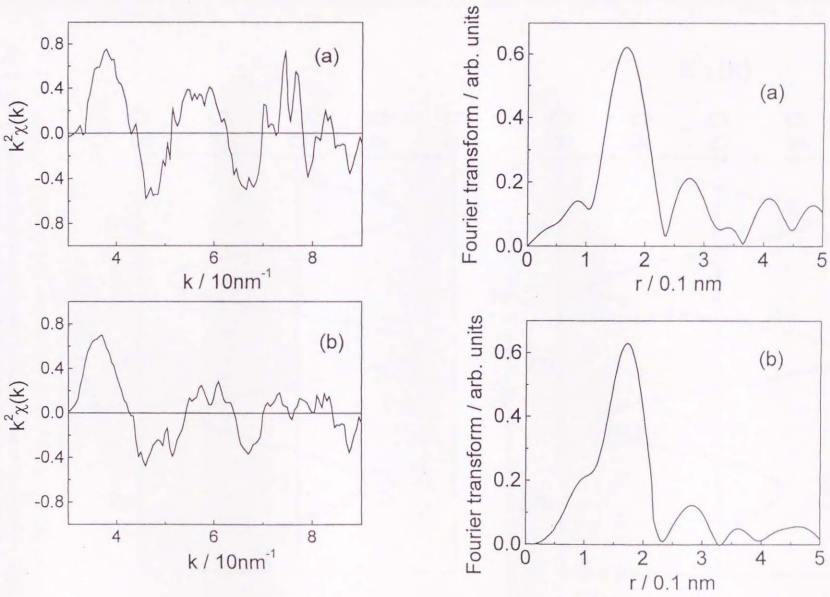

Fig. 2.(A): k^2-weighted EXAFS oscillations for species A, (a) p-polarization; (b) s-polarization. (B): Fourier transforms of the k^2-weighted EXAFS oscillations for species A: (a) p-polarization; (b) s-polarization.

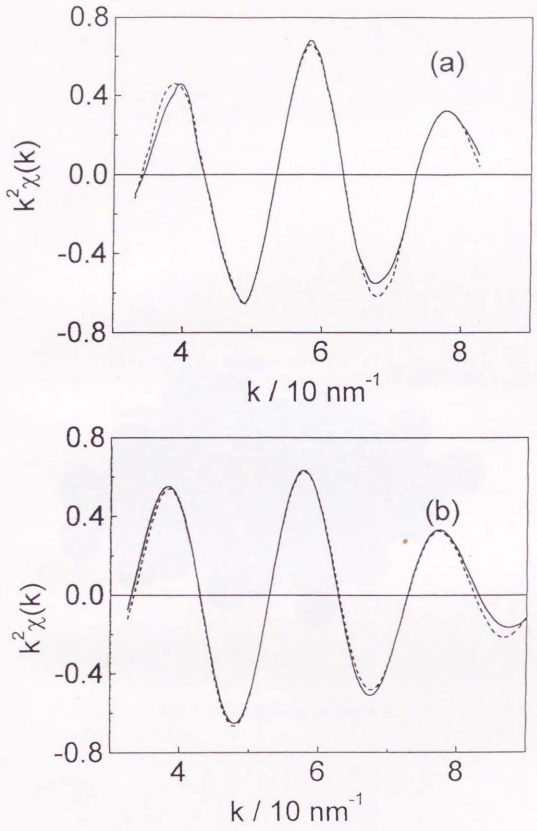

Fig. 3. Best fitting results for inversely Fourier transformed data of the species A. (a) p-polarization; (b) s-polarization. Solid line: filtered data, broken line : calculated data.

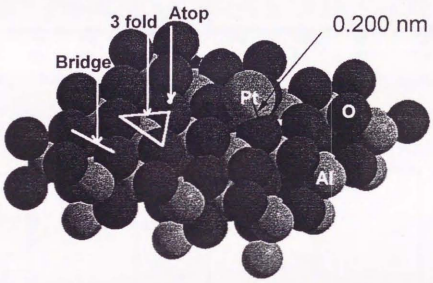

Fig. 4. Model structure for species A.

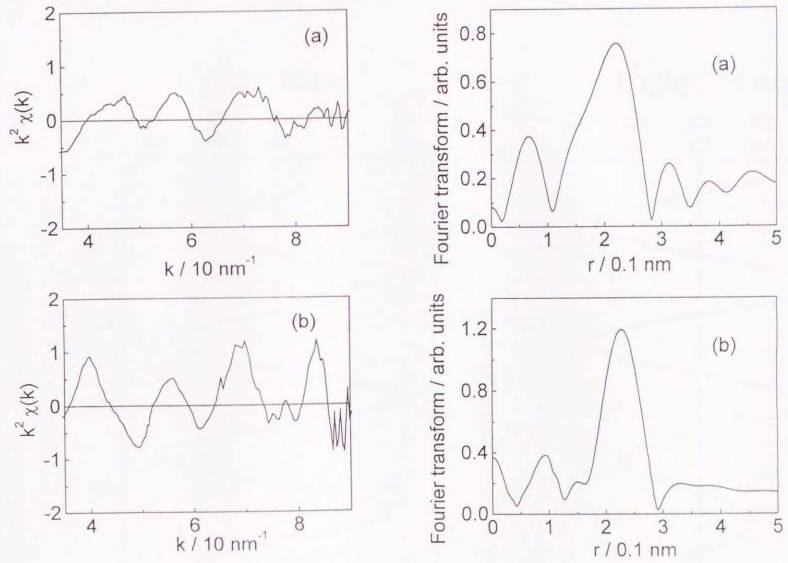

Fig. 5. (A): k^2-weighted EXAFS oscillations of species B obtained by the reduction of species A with hydrogen at 373 K, (a) p-polarization; (b) s-polarization. (B): Fourier transforms of the k^2-weighted EXAFS oscillations for species B , (a) p-polarization; (b) s-polarization.

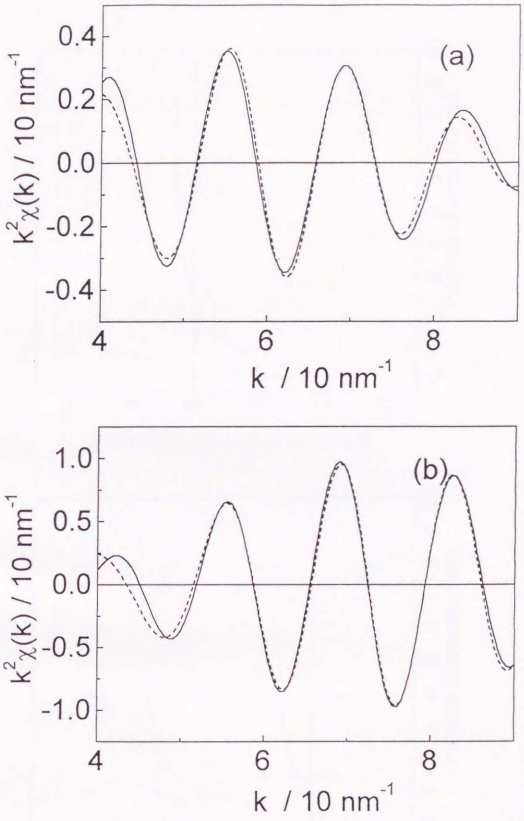

Fig. 6. Best fitting results for the inversely Fourier transformed data of the species B. (a) p-polarization; (b) s-polarization. Solid line: observed data. broken line: calculated data.

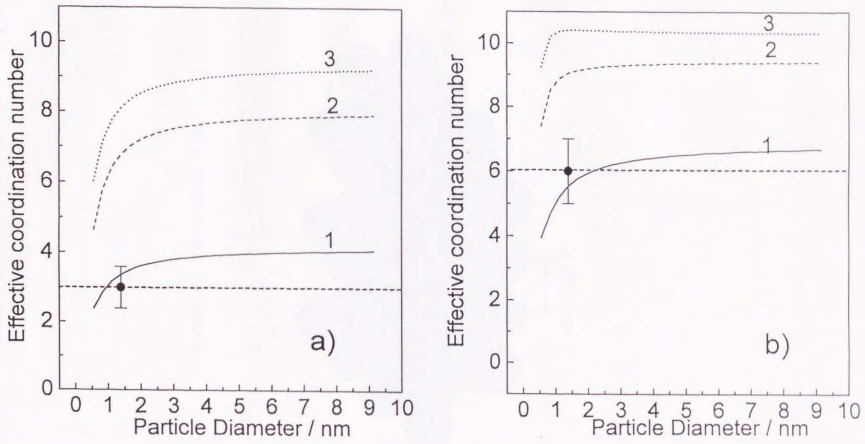

Fig.7. Calculated effective coordination numbers of Pt-Pt for p-polarization (a) and s-polarization (b) as a function of particle size based on the one layer model (solid line 1), the two layer model (broken line 2) and the three layer model (dotted line 3). The observed data are given in a broken line with error bars.

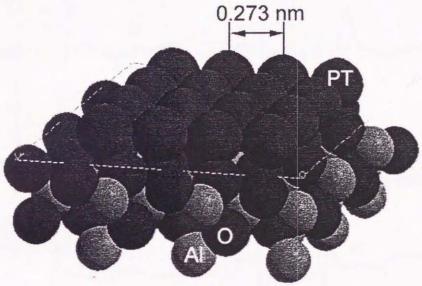

Fig. 8 Model structure for species B.

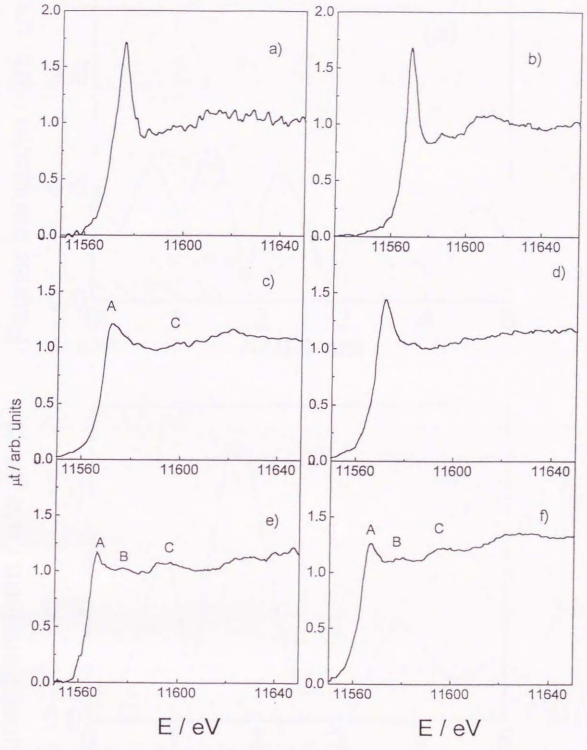

Fig. 9. XANES spectra at Pt L_3-edge for species A (a, b), species B (c, d), and species C (e, f). Frames (a), (c), (e) are for s-polarization and frames (b), (d), (f) are for p-polarization.

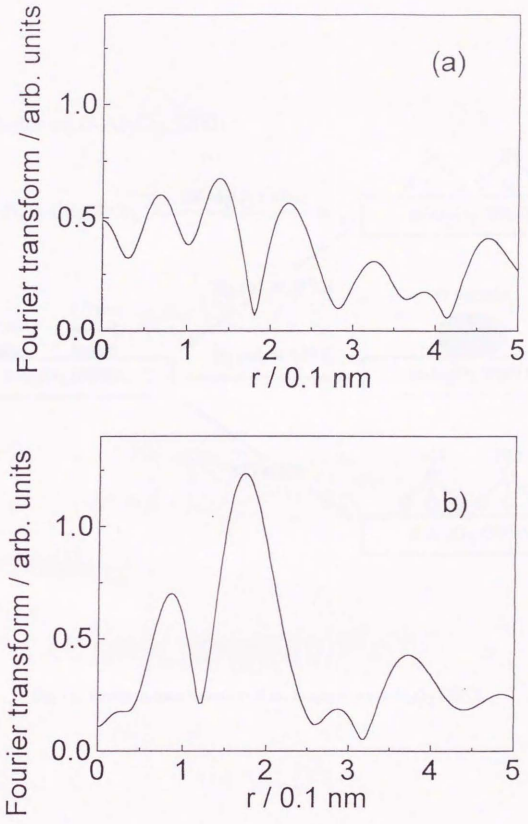

Fig. 10. Fourier transforms of the k^2-weighted EXAFS oscillations for species D after the reaction of species B with NO, (a) p-polarization; (b) s-polarization.

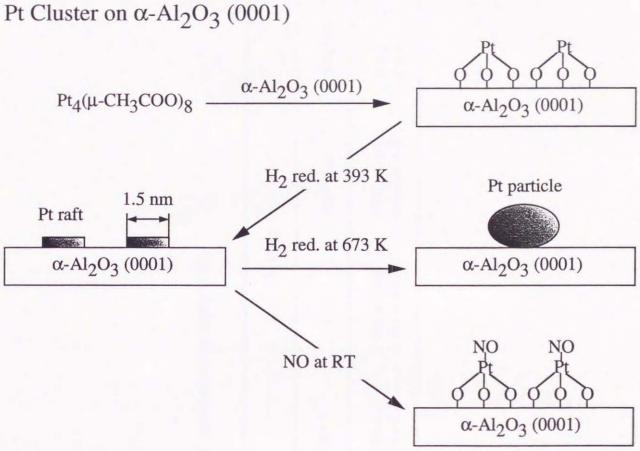

Fig. 11 Structural transformation of the Pt species on α-Al_2O_3 (0001).

Table 1 Curve-Fitting Results for Pt Species A on α-Al_2O_3(0001).

	Pt-O			
sample	N*	r / nm	$\Delta\sigma^2$ / nm	ΔE_0 / eV
p-polarization	3.3 ± 0.5	0.198 ± 0.003	0.001 ± 0.001	3 ± 2
s-polarization	3.0 ± 0.5	0.201 ± 0.003	0.001 ± 0.001	3 ± 2

Table 2 Calculated Effective Coordination Numbers(N^*) for Pt-O at Typical Three Adsorption Sites.

	coordination number			
polarization	experiment	atop	bridge	3-fold
p	3.3 ± 0.5	1.6	2.4	3.1
s	3.0 ± 0.5	0.7	1.8	3.0

Table 3 Best-Fitting Results for the EXAFS Data for Species B.

	Pt-O			
sample	N*	r / nm	$\Delta\sigma^2$ / nm	ΔE_0 / eV
p-polarization	1.5 ± 1.0	0.220 ± 0.009	0.003 ± 0.001	5 ± 2
s-polarization	not observed	not observed	not observed	not observed

	Pt-Pt			
sample	N*	r / nm	$\Delta\sigma^2$ / nm	ΔE_0 / eV
p-polarization	3.0 ± 0.8	0.274 ± 0.003	0.001 ± 0.001	3 ± 2
s-polarization	6.0 ± 1.0	0.273 ± 0.003	0.002 ± 0.001	3 ± 2

Chapter 8

Concluding Remarks

During my doctoral course, I have investigated asymmetric/anisotropic surface structure of active sites by means of the polarization-dependent total-reflection fluorescence XAFS(PTRF-XAFS) technique. I also improved the technique that can be applied to higher Z-elements over 42 since most of those elements have an important role in commercial-purposed catalysts. However, there were several obstacles for PTRF-XAFS measurements due to their considerably high x-ray absorption energy regions. One is that the adjustment of a total-reflection condition is acutely difficult since the critical angle becomes extremely small. The other one is the Bragg diffraction from the substrate which becomes serious problem in the higher x-ray absorption energy region. Thus it has long been believed that these problems made the PTRF-XAFS measurement for them quite difficult.

In Chapters 2 and 3, I revealed that it is possible to measure fluorescent XAFS for those elements under total-reflection conditions. The first problem was overcome by a high-precision angle adjustment apparatus such as the 4-circle diffractometer installed in BL14A. For the second problem, I tried to improve S/N ratio in XAFS signals by applying a compact fluorescent detector, such as a CdTe solid state detector, in order to avoid Bragg diffraction from the substrate effectively since it has a sharp directionality and one can set the detector at the position with no Bragg diffraction. The small detector has advantage to be placed as close as possible to the window of the in-situ cell. With those improvements, I have first succeeded in measuring Mo K-edge PTRF-XAFS which has been believed to be quite difficult. I investigated the surface structure of Mo oxides on $TiO_2(110)$ which is one of important catalytic systems from industrial as well as fundamental interests in Chapter 4. In that work, I challenged to carry out Mo K-edge PTRF-EXAFS measurements for Mo oxides on $TiO_2(110)$ in the 3 different directions of the substrate. $TiO_2(110)$ has an anisotropic surface structure with alternative alignment of the bridging oxygen ridge and the groove composed of rows of five-fold coordinated Ti^{4+} cations along the [001] axis. As the results of Mo K-edge PTRF-EXAFS measurements, I indicated the formation of Mo dimer structure which stepped

over the bridging oxygen row with its Mo-Mo distance at 0.335 nm along the [1 $\bar{1}$ 0] direction of TiO_2(110). It was also found that the Mo dimer species exist at 0.220 nm far from the surface. In Chapter 5, PTRF-EXAFS measurements revealed that the Mo oxides species on TiO_2(110) doped with K has a symmetric tetrahedral Mo oxide structure with Mo-O bond at 0.176 nm due to an interaction between molybdenum and potassium. Through Chapters 2-5, I demonstrated that the improved PTRF-XAFS technique will be a highly potential method for investigation of the symmetric/anisotropic surface structures.

In the Chapter 6, I have conducted in-situ PTRF-XAFS of active Pt catalysts derived from Pt_4 cluster. Beforehand I have investigated $[Pt_4(\mu\text{-}CH_3COO)_8]/SiO_2$ Powder to check the catalytic activity of Pt_4 cluster. As the results of the characterization, the surface structure of the catalyst changed from the tetramer to dimers during an induction period, then to monomers which were active for the catalysis. Subsequently in Chapter 7, in order to investigate the dynamic transformation of Pt particles during the reaction in 3 dimensional way, I applied in-situ PTRF-XAFS technique for $Pt_4(\mu\text{-}CH_3COO)_8$ on $\alpha\text{-}Al_2O_3$ (0001). The Pt_4 cluster framework is destroyed to Pt monomers which occupy the 3-fold hollow sites of the oxygen atoms of $\alpha\text{-}Al_2O_3$(0001) surface, then the isolated Pt atoms are reduced to one-atomic layer thick raft clusters with H_2 at 373 K. The Pt rafts are redispersed to Pt monomers by exposure of NO, or agglomerated to 3 dimensional particles by reduction at 673 K. In the chapter, the technique gives clearer information about anisotropic structure of dispersed active sites under in-situ conditions.

In these works I have demonstrated and come to believe that the PTRF-XAFS method can give the information about the orientation and adsorption sites of metal atoms, metal-support and metal-metal bondings, and anisotropic surface structures. Finally, further developments in photon source and detection apparatus will enable to carry out faster and better experiment for investigating dynamic processes at surfaces.

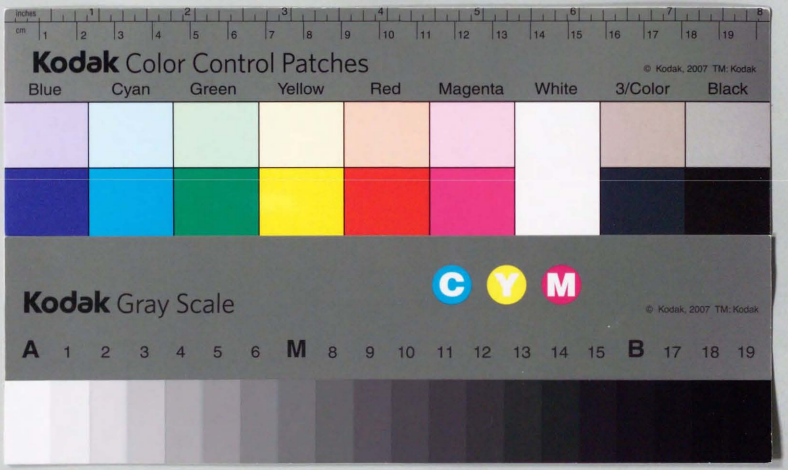
inches
cm
Kodak Color Control Patches
© Kodak, 2007 TM: Kodak
Blue
Cyan
Green
Yellow
Red
Magenta
White
3/Color
Black
Kodak Gray Scale
C
Y
M
© Kodak, 2007 TM: Kodak
A 1 2 3 4 5 6 M 8 9 10 11 12 13 14 15 B 17 18 19